CORRELATION BETWEEN MMP-2 AND -9 LEVELS AND LOCAL STRESSES IN ARTERIES USING A HETEROGENEOUS MECHANICAL MODEL

A Thesis
Presented to
The Academic Faculty

by

Yu Shin Kim

In Partial Fulfillment
of the Requirements for the Degree
Doctor of Philosophy in the
School of Mechanical Engineering

Georgia Institute of Technology
August 2007

CORRELATION BETWEEN MMP-2 AND -9 LEVELS AND LOCAL STRESSES IN ARTERIES USING A HETEROGENEOUS MECHANICAL MODEL

Approved by:

Dr. Raymond P. Vito, Advisor
School of Mechanical Engineering
Georgia Institute of Technology

Dr. W. Robert Taylor
School of Medicine
Emory University

Dr. Andrés J. García
School of Mechanical Engineering
Georgia Institute of Technology

Dr. Zorina S. Galis
Department of Surgery
Indiana University School of Medicine

Dr. Marc E. Levenston
School of Mechanical Engineering
Georgia Institute of Technology

Date Approved: June 28, 2007

To my family

ACKNOWLEDGEMENTS

I would like to express my gratitude to all people who provided me their endless support for the completion of this thesis. First, I would like to express special thanks to my advisor, Dr. Raymond Vito, for his great encouragement and support. I am also thankful to Dr. Zorina Galis for her advice and support for this project. I must thank Dr. Alexander Rachev for working with me to refine my mechanical model and his help in writing this thesis. I am also grateful to my committee members for agreeing to serve on my committee and review my work: Dr. Andrés García, Dr. Marc Levenston, Dr. Robert Taylor, and Dr. Zorina Galis.

I would like to thank Tracey Couse for her advice on histology. I also thank four undergraduate research assistants, John Tidwell, Lindsey Threlkeld, Tiffany Morrow, and Abigail Hung, for their assist in imaging and data processing. I'd like to thank Dr. Hai-Chao Han for teaching me the organ culture techniques.

I would like to thank current and former members of the Vito Lab. I appreciate Dr. Peter Carnell for his friendship and proofreading many of my writings. I also thank Dr. Brian Wayman, Lori Lowder, and Melissa Hallow for their help and support in many ways.

I would like to thank the National Science Foundation and the National Institutes of Health for financial support. This work was supported by funding from the Georgia Tech/Emory Center (GTEC) for the Engineering of Living Tissues, an Engineering Research Centers (ERC) program of the National Science Foundation under award

number EEC-9731643 and the NHLBI R01 64689 from the National Institute of Health. Porcine carotid arteries were generously donated by Holifield Farms of Conyers, GA.

I am especially thankful to all of my family members, especially my parents, JeongWoong Kim, YoungSoon Han, and parents-in-law, JongRyoung Lee, KyoungSook Kim. Their great encouragement and prayer has been with me during the years of my study at Georgia Institute of Technology, and throughout my whole life. Most importantly, I want to thank my wife, Dr. Sanghee Lee, for her perpetual support in so many ways, and my son, Han-Earl Eugene Kim, for bringing me a joy of my life.

TABLE OF CONTENTS

LIST OF TABLES

Page

LIST OF FIGURES

Page

LIST OF SYMBOLS

A_m	Cross-Sectional Area of the Media
c_{c1} and c_{c2}	Material Constants for Collagen
c'_{c1}	Area Fraction-Weighted Material Constant for Collagen
c_e	Material Constant for Elastin
c'_e	Area Fraction-Weighted Material Constant for Elastin
D	Diameter
E_c	Green Strain of Collagen Fiber
E_j, where $j = r, \theta, z$	Green Strain at Tissue Level
e	Error
$\hat{e}$	Unit Vector of the VSMC Nuclear Major Axis
F	Deformation Gradient
F_e	Area Fraction of Elastin in Arterial Tissue
F_c	Area Fraction of Collagen in Arterial Tissue
f_e	Local Area Fraction of Elastin
f_c	Local Area Fraction of Collagen
I	Identity Matrix
I_1	First Invariant of the Green Strain Tensor
I_c	Intensity of Collagen Birefringence
I_e	Intensity of Elastin Autofluorescence
I'_c	Normalized Pixel Intensity of Collagen
I'_e	Normalized Pixel Intensity of Elastin
i	Layer Number

l	Deformed Length of a Helix
l_0	Undeformed Length of a Helix
l_M	Major Axis Length of a VSMC Nucleus
l_{RP}	Length of a Helix at Recruiting Point
l_θ	Circumferential Length of a VSMC Nucleus
P	Pressure
p	Lagrange Multiplier
Q	Flow Rate
R_i	Inner Radius of the Media at the Zero Stress State
R_o	Outer Radius of the Media at the Zero Stress State
(R, Θ, Z)	Cylindrical Coordinate System for Zero Stress Configuration
(r, θ, z)	Cylindrical Coordinate System for Deformed Configuration
$\hat{r}$	Unit Vector of the r-axis
r_i	Inner Radius of Deformed Configuration
r_o	Outer Radius of Deformed Configuration
r_s	Spearman Rank Correlation Coefficient
S_i	Inner Boundary Length of the Media at the Zero Stress State
S_o	Outer Boundary Length of the Media at the Zero Stress State
s_i	Inner Boundary Length of the Media at No Load
s_o	Outer Boundary Length of the Media at No Load
t	Thicnkess
W	Strain Energy Function of Artery
W_c	Strain Energy Function for Collagen
W_e	Strain Energy Function for Elastin

(X, Y, Z)	Imaging Coordinate System
(X_c, Y_c, Z_c)	Centroid
$\hat{z}$	Unit Vector of the z-axis
α_k, where $k = e, c$	Proportionality Constant
Φ	Opening Angle
Ω	Error Function
λ	Eigenvalue
λ_c	Collagen Stretch Ratio
λ_h	Helical Stretch Ratio
λ_{RP}	Recruiting Point
λ_z	Axial Stretch Ratio
μ	Viscosity
ν	Eigenvector
$\hat{\theta}$	Unit Vector of the θ-axis
θ_h	Helical Deviation
θ_{h0}	Helical Deviation at Zero Stress Configuration
θ_r	Radial Deviation
ρ_i	Inner Radius of the Media at No Load
ρ_o	Outer Radius of the Media at No Load
σ_j, where $j = r, \theta, z$	Cauchy Stress
τ	Shear Stress

LIST OF ABBREVIATIONS

ABC	Avidin and Biotinylated Horseradish Peroxidase Complex
COV	Covariance Tensor
DAB	3,3'-diaminobenzidine
DMEM	Dulbecco's Modified Eagle's Medium
ECM	Extracellular Matrix
EEL	External Elastic Lamina
IEL	Internal Elastic Lamina
MEF	Musculo-Elastic Fascicle
MMP	Matrix Metalloproteinase
OCT	Optimum Cutting Temperature
PBS	Phosphate Buffered Saline
SEF	Strain Energy Function
TEVG	Tissue Engineered Vascular Graft
VSMC	Vascular Smooth Muscle Cell

SUMMARY

The mechanical environment influences vascular smooth muscle cell (VSMC) functions related to the vascular remodeling. However, the relationships are not appropriately addressed by most mechanical models of arteries assuming homogeneity. Accounting for the effects of heterogeneity is expected to be important to our understanding of VSMC functions. We hypothesized that local stresses computed using a heterogeneous mechanical model of arteries positively correlate to the levels of matrix metalloproteinase (MMP)-2 and -9 *in situ*. We developed a mathematical model of an arterial wall accounting for nonlinearity, residual strain, anisotropy, and structural heterogeneity. The distributions of elastin and collagen fibers, quantified using their optical properties, showed significant structural heterogeneity. Anisotropy was represented by the direction of collagen fibers, which was measured by the helical angle of VSMC nuclei. The recruiting points of collagen fibers were computed assuming a uniform strain of collagen fibers under physiological loading conditions; an assumption motivated by the morphology. This was supported by observed uniform length and orientation of VSMC nuclei under physiological loading. The distributions of circumferential stresses computed using both heterogeneous and corresponding homogeneous models were correlated to the distributions of expression and activation of MMP-2 and -9 in porcine common carotid arteries, which were incubated in an *ex vivo* perfusion organ culture system under either normotensive or hypertensive conditions for 48 hours. While strains computed using incompressibility were identical in both models, the heterogeneous model, unlike the homogeneous model, predicted higher

circumferential stresses in the outer layer. The tissue levels of MMP-2 and -9 were positively correlated to circumferential stresses computed using the heterogeneous model, which implies that areas of high stress are expected to be sites of localized remodeling and agrees with results from cell culture studies. The results support the role of mechanical stress in vascular remodeling and suggest the importance of structural heterogeneity in studying mechanobiological responses.

CHAPTER 1

INTRODUCTION

Vascular smooth muscle cells (VSMCs) respond to their mechanical environment. Understanding the relationships between functions of VSMCs and mechanical stimuli is important in studying the adaptive and maladaptive changes in the structure and function of arteries. The histology of arterial tissue provides information on how VSMCs respond to mechanical stimuli as well as the structure of arterial tissue.

Structure of Arteries

Arteries have heterogeneous structure and are composed of three distinctive layers: the intima, media, and adventitia. The intima is the innermost layer of the artery and contains a monolayer of endothelial cells. The media consists of various connective tissue components, especially elastin and collagen fibers, and VSMCs. The adventitia contains collagen fibers, ground substance, and some fibroblasts. The intima and media are divided by the internal elastic lamina (IEL), and the media and adventitia are divided by the external elastic lamina (EEL).

Among the three layers, the arterial media is the most responsible for the mechanical characteristics of arterial tissue. The components of the media form a functional and structural unit, a "lamellar unit" (Wolinsky and Glagov 1967). The microstructure of lamellar units was observed to be the repetition of VSMC layers bound by elastin lamellae with collagen fibers in between. Regardless of species, the average tension per lamellar unit of an aortic media was remarkably constant. The repeating unit of VSMCs and extracellular matrix (ECM) proteins, the organizational and functional structural unit of the arterial media, is referred as a "musculo-elastic fascicle (MEF)"

(Clark and Glagov 1985). MEFs are more prominent in aortas than in muscular arteries and aligned in the direction of presumed resultant tensile stress.

Extracellular Matrix

The ECM network formed by elastin and collagen fibers is responsible for most of the mechanical strength of arteries (Torrance and Shwatz 1961; Conklin et al. 2002). The distributions of elastin and collagen fibers, major components of the ECM network, are known to be heterogeneous through the arterial media. In many types of arteries, the concentration of collagen increases while that of elastin decreases from the intima to the adventitia. In bovine carotid arteries, it was observed that the area fraction of collagen increased from 0.183 ± 0.22 to 0.852 ± 0.12 toward the outer layer in the media while that of elastin decreased from 0.336 ± 0.05 to 0.046 ± 0.03 in the same direction (Hasan and Greenwald 1995). In the aortas of children, it was observed that medial elastin decreased while collagen increased from the intima to the adventitia (Feldman and Glagov 1971). In addition, the size of collagen fibrils progressively increases from the intima to the adventitia. Merrilees et al. (1987) reported that the mean diameters of collagen fibrils were 30-40 nm in the intima and inner media and 50-100 nm in the outer media of arteries from human, pig, and rat.

The distributions of elastin and collagen fibers in the media change with aging, indicating lifelong remodeling activities. Feldman and Glagov (1971) observed that transmural gradients of elastin and collagen in the human aortic media were reversed with aging. Avolio et al. (1998) investigated the effect of aging on the fraction of elastin in arteries. Due to the different heart rate among species, they used the number of cardiac cycles as the measure of age. The volume fraction of elastin in the aortic media was lower in the group with the high number of cardiac cycles. This suggested that such changes in medial elastin are associated with cumulative effects of repeated pulsation.

Structure of VSMCs

The mechanical coupling between the elements of cellular structure provides a pathway for mechanical signal transfer and facilitates coordinated changes in cellular and nuclear shapes. The structural framework of cells consists of a cytoskeleton and a membrane skeleton. The cytoskeleton, comprised of actin filaments and intermediate filaments, is anchored to the dense bodies of the membrane skeleton, which is coupled to the ECM (Pienta and Coffey 1992; Davis 1993; Small and Gimona 1998). Cell nuclei also contain a structural framework called the nuclear matrix, which is interconnected with intermediate filaments in the cytoskeleton. Thus, the structural continuity from the nuclear matrix to the ECM exists and enables coordinated control of cell shape (Fey et al. 1984; Pienta and Coffey 1992; Kuo and Seow 2004). The structural integrity of the cellular matrix is well represented by the hypothetical nucleated tensegrity model of a cell (Ingber 1993). The mechanical relevance of the structural integrity among ECM receptors, cytoskeleton, and the nuclear matrix was shown by observing the deformations of cell nuclei in response to mechanical stimuli applied to the cell boundary (Maniotis et al. 1997).

VSMCs are highly elongated spindle-shaped cells each with one nucleus. In addition to the structural lattice of cells, a smooth muscle cell has a contractile apparatus comprised of myosin and actin filaments that is interconnected with the cytoskeleton via cytoplasmic dense bodies and is anchored to the dense plaques of the membrane skeleton (Cooke and Fay 1972; Small and Gimona 1998). Unlike skeletal and cardiac muscles, smooth muscle does not show striations because the contractile elements are not arranged in an orderly fashion. The intracellular organization of the contractile filaments in smooth muscle cells is still poorly understood due to the lack of comprehensive microscopic data (Alberts et al. 1994). Some ultrastructural observations suggest that the contractile apparatus in smooth muscle may be arranged along the plasma membrane (Fay and Delise 1973; Work and Warshaw 1988). In a recent study, Kuo and Seow (2004)

observed that cytoplasmic contractile filaments lie parallel to the longitudinal axis of the cell bundle in the electron microscopic images of swine airway smooth muscle. They also observed the attachment of actin filaments to the nuclear envelope. The mechanical coupling between contractile filaments and nuclear matrix was shown by observing the stretch of the nuclear envelope in response to the isometric contraction of the smooth muscle cells (Kuo and Seow 2004). Although VSMCs account for a small portion of the passive mechanical strength of arteries, they play an active role in the arterial remodeling process in response to changes in mechanical environment. VSMCs are connected to neighboring VSMCs and the ECM network (Kuo and Seow 2004). The mechanical and structural coupling between receptors such as integrins and ECM components provides a pathway for mechanotransduction (Wilson et al. 1995; Williams 1998; Li and Xu 2000).

The morphological characteristics of VSMCs have been quantified to study structural and mechanical properties of cells and arterial tissue. Various visualization methods have been used to capture two- or three-dimensional morphology of VSMCs. Light microscopy with haematoxylin and eosin staining (Walmsley and Canham 1979; Peters et al. 1983; Holzapfel et al. 2002) and fluorescent microscopy with Hoechst staining (Liu 1998) were used to capture two-dimensional orientation of VSMCs in the medial layer. Electron microscopy (Canham et al. 1982; Todd et al. 1983) and confocal microscopy (Arribas et al. 1997; Dickhout and Lee 2000) were used to quantify three-dimensional characteristics such as the orientation and size of VSMCs. Confocal microscopy is a reliable method to study three-dimensional morphology of VSMCs *in situ* without the need for fine sectioning and the alignment of image stacks. The most widely measured characteristics of VSMCs are their orientation (Walmsley and Canham 1979; Canham et al. 1982; Liu 1998; Holzapfel et al. 2002) and length along the long axis of a cell (Todd et al. 1983; Dickhout and Lee 2000).

It has been shown that the orientation of VSMC nuclei is in good agreement with VSMC alignment (Canham et al. 1982) and aligned with collagen fibers in the arterial

media (Canham et al. 1986; Finlay et al. 1991). VSMC nuclei are also coaligned with contractile filaments (Canham et al. 1986; Kuo and Seow 2004). The orientation of collagen fibers, measured by the orientation of VSMC nuclei in arteries at zero stress state, was included in some mechanical models of arteries (Holzapfel et al. 2002; Zulliger et al. 2004; Zulliger et al. 2004). The changes in cell length may be correlated to local strains in intact arteries. Fung (1984) measured the changes in VSMC length using the dense bodies of VSMCs as structural markers. The spacing between dense bodies increased as luminal pressure increased. The distribution of the spacing between dense bodies was statistically uniform throughout the vessel wall at pressures above 20 mmHg. Takamizawa and Hayashi (1987) proposed the 'uniform strain hypothesis' which assumes a constant circumferential strain over the cross-section in the physiological loading state. However, they did not provide histological evidence for such a state.

Functions of VSMCs

Vascular Remodeling

VSMCs change the geometry of arteries in response to changes in mechanical stimuli such as wall shear stress (Kamiya and Togawa 1980; Brownlee and Langille 1991; Fischer et al. 2002), luminal pressure (Liu and Fung 1989; Matsumoto and Hayashi 1996; Fridez et al. 2003), and axial stretch (Jackson et al. 2002; Davis et al. 2005). It is generally accepted that the geometric changes of blood vessels in response to changes in mechanical stimuli tend to restore both circumferential wall stress and intimal shear stress to normal levels. Matsumoto and Hayashi (1994) reported that rat aortic wall thickness increased rapidly in response to hypertension and wall stress developed by *in situ* blood pressure was kept at a normal level. The elastic modulus of the aorta of hypertensive rats at *in situ* blood pressure returned to the normal value in 16 weeks after hypertension was induced. In response to altered blood pressure, geometric changes appear to precede

changes in material properties. Fridez et al. (2003) observed that vascular smooth muscle tone in rat carotid arteries increased rapidly in the acute phase of remodeling (0-8 days) induced by hypertension and returned to near normal levels at long term (56 days). These observations suggest that initial changes in the geometry of arteries are due to the contraction of VSMCs and long-term changes in mechanical properties are attributable to structural remodeling.

Structural remodeling is associated with the production and reorganization of the ECM components by VSMCs. However, mechanical stimuli differentially affect the production of elastin and collagen, two major ECM proteins in arteries. While collagen content in the media of rat carotid arteries increases rapidly in the acute hypertension phase (0-8 days), increases in elastin content are slight (Fridez et al. 2003). This may be due to the differences between the turnover rates of elastin and collagen fibers.

Mature elastin is extremely stable and its turnover is very slow (Debelle and Tamburro 1999). Lefevre and Rucker (1980) estimated the turnover and degradation of mature elastin from the aortas of Japanese quail by measuring the variation in radioactivity of L-[^{14}C] lysine-labeled desmosines in elastin. They concluded that the best estimates of mature elastin turnover are only quantifiable in years. Using light and electron microscopic radioautography, Davis (1993) observed that no new growth or turnover of elastin occurred in the mouse aorta between 28 days and 8 months of age while synthesis of new elastin was observed between 4 to 21 days of age. The author emphasized that initial deposition of elastin and proper assembly of elastic laminas is a critical event in vessel development. The low turnover rate of elastin may be responsible for the decrease of medial elastin over time.

The turnover of collagen fibers in various soft tissues is many times faster than that of elastin and is quantifiable in days (Nissen et al. 1978; McAnulty and Laurent 1987; Sodek and Ferrier 1988). Also, the turnover of collagen fibers in arteries increases many fold in response to an increase in blood pressure. Nissen et al. (1978) reported that

the half-life of collagen fibers in mesenteric arteries and aortas from normotensive rats is 70 days while for hypertensive rats this is reduced to 17 days.

Vascular remodeling activities induced by mechanical stimuli are not uniform through the arterial media. In response to induced hypertension, non-uniform thickening of lamella units through the arterial media was observed in different types of arteries. Matsumoto and Hayashi (1994) observed that the layers near the inner wall thickened more than those near the outer wall in rat aortas in induced Goldblatt hypertension at 8 weeks. However, Fridez et al. (2003) reported a different observation using rat carotid arteries. In response to induced hypertension, the inner layers of rat carotid arteries thickened more in the acute phase (0-8 days), whereas outer layers were thicker at the end of the adaptation phase (56 days post-surgery).

Role of MMP-2 and MMP-9

Matrix metalloproteinases (MMPs) are involved in vascular remodeling activities, either adaptive or maladaptive. MMPs, when activated, degrade ECM proteins in both normal physiological and pathological states (Matrisian 1992; Dollery et al. 1995). MMP-2 and MMP-9, also known as gelatinase A and B, are thought to have similar functions due to their ability to degrade similar substrates, including elastin and gelatin. Johnson and Galis (2004) showed that both MMP-2 and MMP-9 are involved in VSMC migration and the formation of intimal hyperplasia *in vivo* and *in vitro*. They also showed that MMP-9, but not MMP-2, genetic deficiency impaired the ability of VSMCs to attach to gelatin, suggesting that VSMCs bind MMP-9 and use it for assembly of fibrillar collagen. Later, Defawe et al. (2005) showed that MMP-9 has a biphasic effect on VSMC-mediated collagen gel contraction. While endogenous levels of MMP-9 promoted collagen gel contraction, either depletion or overexpression of MMP-9 inhibited gel contraction.

Mechanosensitive Regulation of MMP-2 and MMP-9

Using cell culture experiments, mechanical stimuli have been shown to positively correlate to the expression and activation of MMP-2 and MMP-9. Cyclically stretching cultured human VSMCs from 10% to 16% of their original lengths increased MMP-2 activity (O'Callaghan and Williams 2000). Stationary mechanical strain of 5% also increased the production of MMP-2 and MMP-9 by human VSMCs, although cyclic mechanical strain from 0 to 10% at 1 Hz in the same study did not (Asanuma et al. 2003). The controversial results from these studies may be due to the differences in the magnitude of cyclic stretching. The threshold of stationary strain of VSMCs to produce MMP-2 and MMP-9 was lower than that of cyclic strain in these studies.

The influence of mechanical stimuli on the expression and activation of MMP-2 and MMP-9 has been also studied at the tissue level. Lehoux et al. (2004) observed that MMP-2 activity increased in mouse carotid arteries cultured at both low (10 mmHg) and high pressures (150 mmHg) compared with arteries kept at 80 mmHg, while MMP-9 activity increased only in arteries maintained at high pressure. A change in the pressure-diameter curve was observed in arteries at high pressure, while no change was seen in vessels at both normal and low pressures. The shift in the pressure-diameter curve toward greater distensibility at high pressure was dependent on MMP-9, but not MMP-2, activity. This suggests that changes in the mechanical properties of arteries at high pressure may be related to the nonproteolytic function of MMP-9, modulating VSMC-mediated collagen gel compaction.

The expression and activation of MMP-2 and MMP-9 are distributed heterogeneously through the vessel wall. Arteries and veins investigated in an *ex vivo* organ culture system showed differential distributions of MMP-2 and MMP-9 through the vessel wall in response to altered hemodynamics. It was observed that the expression and activation of MMP-2 is highest in the region of the outer media of porcine carotid arteries perfused *ex vivo* with steady flow at 200 mmHg (Chesler et al. 1999). In human

saphenous veins arterially perfused *ex vivo*, the levels of immunostaining for MMP-2 and MMP-9 and gelatinolytic activity were also more intense in the outer media and the adventitia where the number of proliferating cells was the highest (Mavromatis et al. 2000). Similar patterns of MMP-2 and MMP-9 distributions in porcine coronary arteries were also observed *in vivo* (Wilson et al. 2002). These results suggest that the outer media may be more sensitive to mechanical stimuli than the inner media. Thus, VSMCs in the outer media are expected to sense higher mechanical strain and/or stress resulting in increased production of MMP-2 and MMP-9 by VSMCs. However, it is impossible to measure mechanical stress and strain *in situ* at the microstructural level. Therefore, mechanical models are necessary to predict the mechanical environment of cells and interpret their biological responses.

Mechanics of Arteries

Arterial tissue shows complex mechanical behavior and has nonlinear, viscoelastic, and anisotropic material properties. Arterial tissue is also normally accepted as an incompressible material (Carew et al. 1968). The existence of vascular smooth muscle tone and dynamic properties of arteries make their mechanical properties more complex (Armentano et al. 1995). Various functional forms for the constitutive relation have been proposed to describe the passive mechanical behavior of arteries with a variety of assumptions to describe nonlinearity, anisotropy, zero-stress state, and material homogeneity.

Phenomenological Models

Fung (1965) originally proposed a pseudoelastic model, in which arterial tissue is assumed to be a hyperelastic material. Hyperelastic materials are nonlinear elastic materials under large deformations with very little change in volume. Due to the viscoelastic property of arteries, pseudoelasticity is applicable only to preconditioned

tissues and different strain energy functions (SEFs) are generally needed for loading and unloading processes. Although many mathematical expressions have been proposed for SEFs, they can be categorized into three types: polynomial type (Vaishnav et al. 1972), exponential type (Doyle and Dobrin 1971; Demiray 1972; Fung 1973), and logarithmic type (Takamizawa and Hayashi 1987).

Most pseudoelastic models of arteries assume a homogeneous structure through the arterial wall and are phenomenological in that they are based on fitting experimental data (Chuong and Fung 1983; von Maltzahn et al. 1984; Takamizawa and Hayashi 1987; Vito and Dixon 2003). Thus, the vascular wall microstructure including structural differences between wall layers is not explicitly taken into account. Pseudoelastic constitutive models of arteries assuming homogeneous mechanical properties of the arterial wall and excluding the effects of residual stress show a non-uniform distribution of wall stress with the largest circumferential stress at the intimal surface (Vito and Hickey 1980; Chuong and Fung 1983; Humphrey 1995; Vorp et al. 1995). Including the effects of residual strain significantly reduces the circumferential stress gradient (Chuong and Fung 1986; Matsumoto and Hayashi 1996; Rachev et al. 1996; Chaudhry et al. 1997). However, the distribution of circumferential stress is still not uniform with larger circumferential stress generally located at the luminal surface.

Structural Models

Multi-layered models were introduced to account for differences in the mechanical properties of distinct layers in the arterial wall. von Maltzhan et al. (1981) proposed a nonlinear two-layer cylindrical model for an arterial wall accounting for the structural difference between the medial and adventitial layers, and a different polynomial SEFs were used for each layer. Based on the result of the range of validity analysis, an exponential form for the SEF of the media was proposed (von Maltzahn 1983). The elastic properties of the adventitial and medial layers of bovine carotid

arteries were experimentally measured and analyzed using exponential type SEFs for both of layers (von Maltzahn et al. 1984). Residual strain was not included in this analysis and circumferential and axial stresses were very high at the intimal surface. Rachev (1997) considered an artery to be a thick-walled two-layer tube made of nonlinear elastic incompressible material in studying the remodeling of arterial geometry under hypertensive conditions. Residual strains were included in this model using the opening angle for each layer. Although multi-layered models include the structural differences between the media and adventitia, they do not explicitly account for differences in the mechanical properties of vascular constituents.

Composite models of arteries have been proposed to account for the distinctive mechanical properties of structural components. These models assume that the mechanical property of an arterial wall can be expressed as the combination of mechanical properties of vascular constituents. Holzapfel and Weizsäcker (1998) proposed a two-term SEF: the first term represents the isotropic contribution from elastin; and the second term represents the anisotropic contribution from collagen fibers. Holzapfel et al. (2002) included the structural differences between the media and adventitia as well as the distinctive mechanical property of each structural component. They used the same form of SEF but different sets of material parameters for the media and adventitia. They also introduced the anisotropy of each wall represented by the orientation of collagen fibers, which was measured using VSMC nuclei in the media and the intra-spatial voids between collagen fiber bundles in the adventitia.

In addition to the features of the composite models, constrained mixture models include not only the wavy nature of collagen fibers but also the fraction of both elastin and collagen fibers contained in the media. Zulliger et al. (2004) proposed a SEF composed of the SEFs of elastin and collagen fibers weighted by the area fraction of each component. They also included the gradual recruitment of initially wavy collagen fibers using the log-logistic distribution function. Using a single function for the recruitment of

collagen fibers implies that collagen fibers through the arterial wall are straightened up in the same fashion in terms of tissue level strain. Zulliger et al. (2004) proposed a pseudo-SEF which includes vascular smooth muscle tone. This model can describe the mechanical behavior of arteries not only under passive conditions, but also under conditions with varying levels of vascular smooth muscle tone. Wuyts et al. (1995) also proposed a model which accounts for the mechanically important constituents, collagen fibers, elastin, and VSMCs, and includes the gradual stretching of collagen fibers. However, they assumed all components obey Hooke's law, which is not applicable when strain is large. They also expressed the gradual recruitment of collagen fibers by a function of strain. Although variables in the recruitment function of collagen fibers are often said to have physical meaning, the functions are usually phenomenological and evaluated by the degree of overall fit to pressure-diameter relations.

Zero Stress State

The unloaded state of arteries was often considered to be the zero-stress state. However, arteries do have residual stress and strain. When arterial ring segments are cut and allowed to freely expand radially, they open up indicating the existence of residual stress in the unloaded state. The so called "opening angle" is often used as an indicator of residual strain (Chuong and Fung 1986; Rachev and Greenwald 2003). Currently, most mechanical models of arteries use the "opened-up" segment of arterial tissue as zero-stress reference state. The stress concentration at the inner surface resulting from pressure loading decreases as the opening angle increases. Peterson and Okamoto (2000) investigated the sensitivity of circumferential stress to variations in the opening angle. They used a SEF and pressure-diameter data of rabbit carotid arteries published by Chuong and Fung (1983) and showed that the distribution of circumferential stress becomes mostly uniform at the opening angle of 130°. However, a mean opening angle

of rabbit carotid arteries reported by Li and Hayashi (1996) is 95°, which still makes the circumferential stress highest at the innermost surface.

The opening angle of arteries changes due to the growth and remodeling of arterial tissue. It has been shown that opening angle changes with age. The opening angle of human aorta from subjects aged between 3 months and 87 years increased with age (Saini et al. 1995). The opening angle of rat aorta was also observed to increase from the age of 6 weeks to 56 weeks (Badreck-Amoudi et al. 1996). Opening angle was also observed to increase in response to hypertension. The opening angle of rat's aorta increased rapidly in response to induced hypertension, then decreased gradually (Liu and Fung 1989).

Many studies showed that additional residual strains and stresses exist in the opened-up configuration (Greenwald et al. 1997; Stergiopulos et al. 2001; Matsumoto et al. 2002). Greenwald et al. (1997) reported that removing material from the outer surface caused the opening angle of the remaining inner layers to increase, while removing material from the inner surface caused the opening angle to decrease. This implies that additional residual strains and stresses at the microstructural level exist in the opened-up state. Stergiopulos et al. (2001) showed that the inner half of a porcine aorta has significantly larger opening angle than the outer half.

The zero stress states of each component in arteries are expected to differ from each other. Greenwald et al. (1997) showed that removing elastin caused the opening angle to decrease while removing collagen or VSMC had no effect. Thus, each microstructural component of the arterial wall supports a different level of residual stress. This suggests the reference configuration of collagen fibers and VSMCs are not readily available. Thus, the tissue-level strain at the recruitment of collagen fibers may not be uniform as proposed in many models of arteries. Matsumoto et al. (2002) also showed that residual stress depends on the components of tissue at the microscopic level using scanning micro indentation test on porcine thoracic aortas.

Homogeneous or Heterogeneous Media

Although arteries show distinctive structural heterogeneity in the media, most studies of arterial mechanics assume homogeneous mechanical properties across the media. Although some mechanical models of arteries include layered features and microstructural information, such as fiber orientations, these models typically assume homogeneous material properties in the medial layer.

The justification for assuming homogeneity is quite controversial. Based on measurements of the deformations of elastic lamellae in normal and inverted arterial segments of canine carotid arteries, Dobrin (1999) suggested that the media acts mechanically like a homogeneous material. However, the strain distribution in arteries is mostly constrained by their tubular structure and incompressibility. Thus, the distribution of material properties across the arterial wall cannot be accounted for by the strain measures alone. Stergiopulos et al. (2001) also supported a single-layered model of the media with homogeneous mechanical properties by comparing the elastic properties and the compositions of the inner and outer halves of the porcine aortic media. However, they also observed significantly more collagen in the outer half of porcine aortic media and said that the uniformity of elastic properties may not be applicable to other types of arteries.

There are also studies suggesting that the arterial wall is mechanically heterogeneous. Vito et al. (1991) measured the distribution of strains in cross sections of the canine thoracic aorta and showed an increased stiffness near the outer wall. Also, residual stresses depend on tissue components at the microscopic level (Matsumoto et al. 2002). The distribution of mechanical stress through the arterial wall is affected by both opening angle and the composition of arterial layers (Peterson and Okamoto 2000). Thus, the mechanical heterogeneity of the arterial media is presumably due to the microstructural heterogeneity. Some theoretical studies also suggested heterogeneous mechanical properties in the media. Using a simple phenomenological model for vascular

growth, Taber and Humphrey (2001) suggested two things: (1) the material properties of bovine carotid arteries are heterogeneous across the wall with stiffer outer layers; (2) growth in arteries correlates better with stress than with strain.

In conclusion, a mechanical model of an artery representing the heterogeneous nature of the medial structure is needed to better understand the physiology and pathophysiology of arterial tissue. To our knowledge, currently available mechanical models of arteries do not account for the structural heterogeneity across the arterial media. The lack of explicit description of the arterial microstructure (i.e. zero stress configurations of collagen fibers) necessitates further exploration of various assumptions and histological techniques for quantification. Filling this gap of knowledge is important to improve the ability of mechanical models to predict responses of vascular cells.

CHAPTER 2

RESEARCH OBJECTIVES

Knowledge on the distributions of mechanical stress and strain through the arterial wall is essential in understanding the physiology and pathophysiology of arterial tissue. The mechanosensitive functions of vascular cells are in part responsible for activities related to vascular remodeling (Langille 1996). The relationships between mechanical factors and vascular cell functions have been studied experimentally utilizing cultured cells or tissue segments (Williams 1998). Although cell culture experiments offer better control of the mechanical stimuli applied to the cells than do experimental approaches utilizing tissue samples, they do not provide a natural environment for cells. Tissue level experimental approaches, either *in vivo* or *ex vivo*, provide the distribution of biological responses of cells in their natural environment. However, the mechanical environment of cells *in situ* is not well understood. Since mechanical stress cannot be measured *in situ*, mathematical models are necessary to interpret results from tissue level studies using relationships established in cell culture studies.

A mechanical model is a useful tool not only for bridging results from cell culture and tissue level studies but also for utilizing these results for engineering a functional tissue engineered vascular graft (TEVG). The potential of mechanical models of native or engineered biological tissues lies in their ability to predict the directions of cellular activities in response to their mechanical environment. However, the link between the local mechanical environment of VSMCs and their functions *in situ* is, for many reasons, still not addressed properly by existing mechanical models of arteries. Among the characteristics of arterial tissue, the structural heterogeneity of the arterial media has long been ignored in mechanical modeling. Currently, most mechanical models of blood vessels assume homogeneous material properties in the arterial media, yet accounting for

the effects of heterogeneity may be important to the understanding of VSMC functions. Moreover, understanding these effects may reveal important clues regarding the pathogenesis of vascular disease and the design of a functional TEVG.

Higher levels of MMP-2 and MMP-9 expression and activation were observed in the outer media of arteries in both *in vivo* and *ex vivo* studies. Results from experiments using cultured VSMCs show that mechanical stretching positively correlates to the production of MMP-2 and MMP-9 by VSMCs. Interpreting these results in terms of the stress and strain distributions across the arterial wall is problematic when using a mechanical model assuming homogeneous properties in the medial layer, which generally predicts lower stress and strain in the outer media. Strain distribution in the arterial wall is readily determined from the tubular structure of arteries and incompressibility. Thus, stress distribution may correlate to the distribution of the expression and activation of MMP-2 and MMP-9. Since arteries exhibit known structural heterogeneity and varying stiffness across the arterial wall, it is worth examining the effect of heterogeneity on the distribution of local stress and cell functions. Therefore, a mechanical model of an arterial wall, including microstructural heterogeneity, was developed and used to determine the correlation between circumferential stresses and the expression and activation of MMP-2 and MMP-9 by VSMCs.

This study serves as the foundation for our long-term goal, which is to promote the understanding of the mechanobiology of vascular cells and the physiology and pathophysiology of arterial tissue. Further, we expect the established knowledge on the relationship between mechanical stress/strain and the mechanosensitive response of vascular cells will contribute to the design of methods for the prevention and treatment of various diseases.

Hypothesis

Local stresses computed using a heterogeneous mechanical model of arteries positively correlate to the levels of MMP-2 and MMP-9 expression and activation by VSMCs *in situ*.

Specific Aims

Specific Aim 1: Quantify the distributions of ECM components and VSMC nuclear geometry in porcine common carotid artery subjected to physiologic mechanical loading conditions.

Information on the structure of arteries is essential for the development of the structure-based mechanical of arteries. Using the optical properties of elastin and collagen fibers, the distributions of elastin and collagen fibers through the media can be quantified. The deformation of collagen fibers can be indirectly quantified from the geometry of VSMC nuclei. Thus, a methodology for quantifying the three-dimensional geometry of VSMC nuclei in intact arteries was developed and used to quantify the distributions of length and orientation of VSMC nuclei in the arterial wall fixed at *in vivo* length and either 0 mmHg or 100 mmHg

Specific Aim 2: Develop the heterogeneous mechanical model of an artery to account for nonlinear elasticity, anisotropy, residual stress, and structural heterogeneity.

The distributions of stresses are influenced by both material composition and residual strain. The residual strains of porcine common carotid arteries can be quantified by measuring opening angle. Considering the arterial tissue as a constrained mixture, a heterogeneous mechanical model of an artery can be developed assuming the area

fractions of elastin and collagen fibers vary through the wall thickness. With structural information obtained in Specific Aim 1 and opening angle, the distributions of circumferential stress through the arterial wall can be computed.

Specific Aim 3: Determine the correlation between the distribution of circumferential stress and the distributions of the expression and activation of MMP-2 and MMP-9.

The distributions of the expression and activation of MMP-2 and MMP-9 under normotensive and hypertensive conditions quantified using an *ex vivo* organ culture experiment and histology can be correlated to the distribution of circumferential stress computed in Specific Aim 2. By comparing this to the result using a homogeneous model, the effects of structural heterogeneity on the distribution of local stress and cell functions are examined.

CHAPTER 3

METHODS

Experimental Study

Organ Culture Experiment

Fresh porcine common carotid arteries were harvested from six to seven-month-old pigs at a local abattoir. Immediately after the arteries were excised, they were washed with ice-cold PBS (Dulbecco's phosphate buffered saline, Sigma, St. Louis, MO) supplemented with 1% antibiotic-antimycotic solution (Sigma) in the lumen and were transported to the laboratory in PBS at 4°C. After testing the intact arteries for leaks, segments of 50 to 70 mm were prepared from locations between 10 mm and 100 mm upstream of the carotid bifurcation.

The arteries were cultured 48 hours in the *ex vivo* perfusion organ culture system, shown in Figure 4.1, described previously (Han and Ku 2001) and modified to include bi-axial control of the mechanical environment (Davis et al. 2005). Briefly, the arteries were mounted in physiological orientation between two cannulae in the organ culture chamber for perfusion in their *in vivo* flow direction. Then, the flow loop was filled with preheated (37°C) prefusion medium. The chamber was filled with bath medium and sealed to maintain sterility. Both the perfusion and bath medium were composed of Dulbecco's modified Eagle's medium (DMEM, Sigma) supplemented with sodium bicarbonate (3.7 g/L, Sigma), L-glutamine (2 mmol/L, Sigma), antibiotic-antimycotic solution (10 ml/L, Sigma), and calf serum (10% by volume, HyClone, Logan, UT). Dextran (6.3% by weight, average molecular weight 170,000; Sigma) was added to the perfusion media to acquire a fluid viscosity of blood (4×10^{-3} Pa·s). The viscosity was measured with a

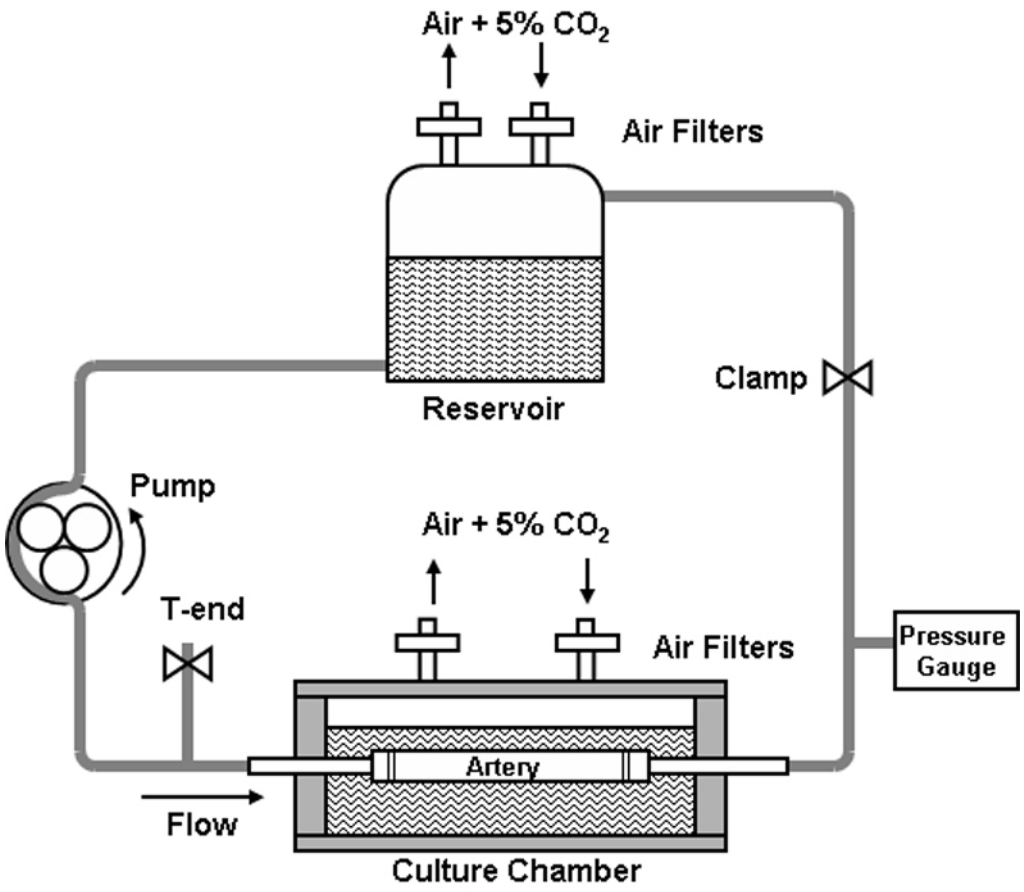

Figure 4.1: Schematic of the *ex vivo* artery organ culture system. The arterial segment is mounted on stainless steel cannulae in the chamber and perfused with the culture medium. The perfusion flow, pressure, and pulsatility are controlled by adjusting pump speed, clamp resistance, and the T-end tubing length, respectively.

Canon-Fenske viscometer (Cannon Instrument Co., State College, PA). The system was placed in an incubator in a 5% CO_2 + 95% air mixture maintained at 37°C.

Experiments were conducted in pairs using right and left carotid arteries from same animal. In each pair of arteries, one was cultured under a normotensive condition and the other under a hypertensive condition. Upon any sign of contamination during the organ culture, the specimen was discarded and excluded form the analysis. To mimic the physiological loading condition, the arteries were stretched to *in vivo* length (axial stretch ratio, $\lambda_z = 1.5$) and perfused with a pulsatile flow at a transmural pressure of 100 ± 20 mmHg. Initially, the arteries were unstretched and subjected to a minimal flow to prevent possible damage to the tissue by abrupt changes in the mechanical environment. The stretch ratio of the arteries, the flow rate of the perfusion medium and mean luminal pressure were gradually increased to *in vivo* levels over three hours. The flow rate was controlled to maintain a mean shear stress (τ) of 1.5 Pa according to the Poiseuille relationship,

$$\tau = \frac{32\mu Q}{\pi D^3}, \tag{4.1}$$

where D is the lumen diameter of the vessel, μ is the viscosity of the medium, and Q is the flow rate (Ku 1997). For the normotensive group (n = 5), the conditions equivalent to the *in vivo* mechanical environment, once reached, were maintained for 48 hours. For the hypertensive group (n = 4), a transmural pressure was further increased to 200 ± 20 mmHg and maintained for 48 hours.

At the end of the organ culture, the contractile response of VSMCs was disabled by adding 10^{-4} mol/L of sodium nitroprusside (Sigma) into the flow loop 30 minutes before the flow was stopped. This served to prevent a reflex response during tissue processing. After removal, each artery was divided into three segments. Two short

segments (~5 mm) were embedded in Tissue-Tek® optimum cutting temperature (OCT) compound (Sakura Finetek, Torrance, CA) and frozen in liquid nitrogen for immunohistochemistry and *in situ* zymography. The remaining segments (one from each artery) were reattached to cannulae and fixed in 10% formalin at pressure and *in vivo* length to preserve the microstructure at the mean incubating pressure, 100 mmHg for the normotensive group and 200 mmHg for the hypertensive group.

Quantification of Expression and Activation of MMP-2 and MMP-9

Immunohistochemistry

Immunostaining for MMP-2 and MMP-9 was performed on 7 μm frozen sections and used to investigate the localization of the expression of MMP-2 and MMP-9. Sections were thawed for 10-30 minutes immediately before use at room temperature. The sections were first fixed in acetone for 5 minutes. After preincubation with 0.3% hydrogen peroxide in methanol to block endogenous peroxidase activity, tissue sections were blocked with 10% normal horse serum (Vector Laboratories, Burlingame, CA) in PBS (Sigma) for 20 minutes at room temperature. Specimens were then incubated for 60 minutes at room temperature in a humid chamber with primary antibodies for MMP-2 or MMP-9 (EMD Biosciences, San Diego, CA) diluted to 5 mg/L in PBS. After being washed in PBS, sections were incubated for 30 minutes in a humid chamber with biotinylated secondary antibodies in PBS plus 2% horse serum, followed by incubation for 1 hour with VECTASTAIN® Elite ABC reagent (avidin and biotinylated horseradish peroxidase complex, Vector Laboratories). Gray-black stain was developed using DAB (3,3'-diaminobenzidine) substrate kit (Vector Laboratories). Because the slides were used for the quantification of the expression of MMP-2 or MMP-9, nuclei were not counterstained.

A series of monochrome images were taken using a conventional brightfield microscope. From the images, the intramural distribution of the area fraction of MMP-2 or MMP-9 expression was quantified semi-automatically using MATLAB® code. First, the intima and the outer boundary of the external elastic lamina (EEL) were traced manually by picking control points of a cubic spline curve in each image. The cross-section of an artery is generally close to but not a circular ring. Thus, the arterial wall, bound by two curves, was mapped to a circular ring. Then, the circular ring was divided into 51 layers, which is the number of layers used for the quantification of elastin and collagen fibers in the arterial wall. The thickness of each layer in the circular ring was set to be uniform at the mean incubating pressure and *in vivo* length. Since the arterial segments used for immunohistochemistry were fixed at zero pressure without axial stretch, the thickness of each layer in the immunostained sections was determined using incompressibility to match the corresponding layer in pressure-fixed sections. To quantify the area fraction of MMP-2 or MMP-9 expression, a threshold mask was defined by sampling pixel intensities in the visually identified positive stains (Lee et al. 1996). The threshold was applied to each image and the area fraction of MMP-2 or MMP-9 positive pixels in each layer was calculated and recorded.

In Situ Zymography

The localization of the activities of MMP-2 and MMP-9, gelatinolytic activity, in arterial cross-sections was detected using *in situ* zymography as described by Galis et al. (1995). Briefly, fluorescent substrate, gelatin from pig skin conjugated to Oregon Green® 488 dye, was purchased from Molecular Probes (Eugene, OR). Low gelling temperature agarose (1% by weight, Sigma-Aldrich, St. Louis, MO) was melted in a reaction buffer (50 mmol/L Tris-HCl, pH 7.4, containing 10 mmol/L $CaCl_2$, and 0.05% Brij 35), then mixed (1:1) with fluorescent substrate (1 g/L in PBS) at 50°C. The substrate solution (10 μl) was spread on prewarmed (~50°C) glass slides, and then allowed to gel at room

temperature. Seven-micron frozen sections of specimens were mounted on top of the substrate film and incubated in a humid and dark chamber at 37°C up to 4 days.

A series of images were taken from each slide using a fluorescent microscope with an FITC filter cube (Chroma Technology, Rockingham, VT). The distribution of substrate lysis, shown as dark areas, represents the localized activities of MMP-2 and MMP-9. A threshold for each image was determined independently to detect localized gelatinolytic activities. Each image was converted to a binary image using the threshold. The intima and the outer boundary of the EEL were traced, and the area between boundaries was divided into the same number of layers as in the quantification of MMP-2 and MMP-9 expressions. The area fraction of dark area in each layer was calculated automatically and recorded.

Statistical Analysis

The transmural distributions of the expression and activation of MMP-2 and MMP-9 in normotensive arteries and hypertensive arteries were analyzed visually and by computing the Spearman rank correlation coefficients (r_s) between the area fractions of MMP-2 positive staining, MMP-9 positive staining, or substrate lysis and the normalized thickness. Groups of correlation coefficients were tested for zero mean using the single-sample Student's t-test. Because the correlation coefficients are not normally distributed, they were transformed with the Fisher transformation and considered as samples from a normal distribution with unknown mean and variance. A p-value of 0.05 was considered as statistically significant in all cases.

Quantification of Arterial Structure

Visualization and Quantification of ECM Components

Elastin

Elastin was visualized using its autofluorescence (Blomfield and Farrar 1967). Elastin exhibits more intense autofluorescence than other ECM proteins when visualized at fluorophore excitation/emission maxima of 480/535 nm (Fitzmaurice et al. 1989). Images of elastin autofluorescence were taken directly from 7 μm paraffin sections using an FITC filter cube and ×10 objective lens on a Nikon fluorescent microscope. The spatial resolution of the image was 0.46 μm/pixel. Exposure time and offset value were manually controlled to enhance contrast and reduce weak fluorescent signal from other matrix proteins. Twenty to thirty images were taken along the circumference of each arterial histologic cross-section covering the entire area of the arterial wall.

The area fraction of elastin in each layer was assumed, using the rationale provided by Baraga et al. (1990), to be linearly proportional to the mean intensity of elastin autofluorescence in that layer. From the elastin images, the intramural distribution of autofluorescence intensity, measured by 8-bit gray level, was quantified automatically. The intima and the outer boundary of the EEL were traced, and the area between traced boundaries was divided into 51 layers using the method used for the quantification of MMP-2 and MMP-9 expression. Since the arterial segments used for the quantification of elastin were fixed at the mean incubating pressure and *in vivo* length, the thickness of each layer in the circular ring was set to be uniform. The average intensity of pixels in the i^{th} layer (I_{ei}, i = 1, 2,…, 51), where the 1st layer is the inner-most layer and 51st layer is the outer-most layer, was calculated and recorded automatically.

Collagen

Collagen fibers are birefringent and were visualized using polarized microscopy and staining to enhance the birefringence. Picrosirius red staining is known to be specific to collagen (Junqueira et al. 1979) and increases birefringence in a concentration and staining time-dependent manner (Canham et al. 1999). Collagen fibers were imaged from the same sections used for the elastin imaging. After the elastin images were taken, the sections were deparaffinized and stained for 75 minutes with 0.1% Sirius red F3B (Direct Red 80, Sigma-Aldrich) in saturated picric acid (Sigma) solution. Then the sections were washed in 0.5% acetic acid in dH_2O for 5 minutes. After washing in dH_2O for 5 minutes, the sections were dehydrated in ascending grade alcohols followed by xylene. A drop of Permount® (Fisher Scientific, Pittsburgh, PA) was applied on top of the tissue section and the cover glass was placed. As in elastin imaging, twenty to thirty images of collagen fibers were taken with a ×10 objective lens and two linear polarizers along the circumference of each arterial histologic cross-section covering the entire area of the arterial wall. An image taken with the slide located between two crossed polarizers (i.e. the polarization directions of two polarizers are crossed) provides a partial image of collagen fibers. Thus, two images were taken at each location. The second image was taken with the crossed polarizers rotated 45° from the setup used for the first image. Superimposing two sets of collagen images generated the final images of collagen fibers aligned to the imaging plane.

The area fraction of mechanically significant collagen fibers in superimposed images was assumed to be linearly proportional to the mean intensity of pixels. The level of collagen birefringence depends on various factors including the thickness (Junqueira et al. 1979; Junqueira et al. 1982; Canham et al. 1999), the orientation (Ehlers 1987; Whittaker et al. 1994), the maturity (Szendroi et al. 1984; Whittaker et al. 1994), and the type of collagen fibers (Wolman and Kasten 1986). These factors affect the collagen

birefringence but the net result is that more intense birefringence represents higher mechanical strength. However, it is a difficult task to formulate an explicit mathematical relationship between collagen birefringence and the area fraction of straightened collagen fibers due to the lack of a comprehensive understanding of its relationship to some of these factors. Hence, as a first approximation, the average intensity of pixels in the i^{th} layer (I_{ci}, i = 1, 2,…, 51) was quantified using the same method used for the quantification of elastin.

Statistical Analysis

The transmural distributions of elastin and collagen fibers in normotensive arteries and hypertensive arteries were analyzed visually and by computing the Spearman rank correlation coefficients (r_s) between the area fractions of elastin or collagen fibers and the normalized thickness. Groups of correlation coefficients were tested for zero mean using the single-sample Student's t-test. Because the correlation coefficients are not normally distributed, they were transformed with the Fisher transformation and considered as samples from a normal distribution with unknown mean and variance. A p-value of 0.05 was considered as statistically significant in all cases.

Quantification of Three-Dimensional Geometry of VSMC Nuclei

Specimen Preparation

Fresh common carotid arteries from six to seven-month-old pigs were harvested at a local abattoir. Arteries were washed and kept in ice-cold PBS supplemented with 1% antibiotic-antimycotic solution during transportation. After testing for leaks, arterial segments were washed and kept in PBS preheated to 37°C for an hour. To preserve the geometry of the passive VSMC nuclei, the contractile response of VSMCs was disabled by the addition of sodium nitroprusside to a final concentration of 10^{-4} mol/L. After 30 minutes, arteries were mounted between two cannulae and stretched to *in vivo* length

(axial stretch ratio, $\lambda_z = 1.5$). The arterial lumens were filled with 10% formalin either at no pressure or at 100 mmHg (Table 4.1). Then, the chamber was filled with 10% formalin. After overnight fixation, arteries were cut into segments, processed, and embedded in paraffin for sectioning.

Table 4.1: Specimens used for the quantification of VSMC nuclear geometry. Each pair was composed of left and right common carotid arteries from the same pig. All arteries were fixed at *in vivo* length.

Fixed pressure	Specimen Pair #	# of VSMC nuclei counted
0 mmHg	1	291
	2	372
100 mmHg	1	525
	2	485

Paraffin-embedded arterial segments were cut into 25 μm sections. Paraffin sections were deparaffinized, and rehydrated in descending grades of alcohol. After washing in dH_2O for 5 minutes, sections were stained for 20 minutes under dark conditions with Hoechst 33258 (Molecular Probes, Eugene, OR) diluted to 1 μg/ml in PBS. Sections were washed twice in PBS for 5 minutes each, then cover slipped using fluorescent mount medium (Fluoromount-G, Southern Biotechnology Associates, Birmingham, AL). Stained sections were stored in a dark box at 4°C.

Three-Dimensional Visualization of VSMC Nuclei

The morphology of VSMC nuclei were visualized using LSM 510 UV confocal microscope (Carl Zeiss, Thornwood, NY) equipped with a water-cooled argon laser with excitation lines in the range of 351-364 nm. The pinhole size was set to 76 μm (1.5 Airy units) with a ×40 objective lens to make the thickness of an optical section 1 μm. The

cross-section of arterial segments was aligned to the imaging plane, which is the *XY*-plane with respect to the imaging coordinate system (*X*, *Y*, *Z*), shown in Figure 4.2. Optical sections, consisting of two-dimensional images on the *XY*-plane, were acquired and stacked to form a Z-stack. The scanning interval, the distance between neighboring optical sections in the *Z* direction, of each Z-stack was controlled to be about 1 μm. Although a ×40 objective lens provides enough resolving power to reconstruct VSMC nuclei, the size of the imaging window (230.4 μm *(X)* × 230.4 μm *(Y)* with a spatial resolution of 0.45 μm/pixel) was not large enough to cover the thickness of an arterial wall. Thus, three or four Z-stacks were acquired with a small overlap between neighboring Z-stacks along each transmural path from the intima to the EEL. VSMC nuclei in the overlapped region were used to align Z-stacks.

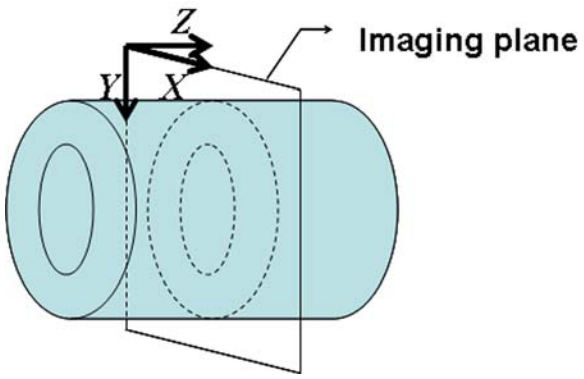

Figure 4.2: The imaging plane of each optical section is the *XY*-plane with respect to the imaging coordinate system (*X*, *Y*, *Z*).

Two-dimensional images of each Z-stack were smoothed to reduce noise by using a 3×3 kernel in the *XY*, *YZ*, and *XZ* planes, respectively. Optical sections from a smoothed Z-stack were converted to binary (black or white) images using a preset threshold value, and then reassembled into a binary (0 or 1) three-dimensional matrix, in which each entry

represents a voxel. A three-dimensional object consists of interconnected voxels with assigned value of 1. From each matrix, three-dimensional objects were identified and labeled using a 26-connected neighborhood scheme, in which voxels are connected if their faces, edges, or corners touch. The objects identified include VSMC nuclei as well as unwanted noise factors such as endothelial cell nuclei and fragments of elastin autofluorescence. The set of objects that consist of less than 500 voxels was first filtered to remove unwanted small fragments. Then, VSMC nuclei were identified manually using two- and three-dimensional visual representations of each object. Two-dimensional visual representation showed the projection of a selected object onto the *XY*-plane in white, while other objects and voids were gray and black, respectively (Figure 4.3). The three-dimensional visual representation provides an isosurface view of a selected object with respect to a coordinate system, where each voxel represents a cube. However, a voxel is not a cube in physical dimensions. Thus, the aspect ratio of each axis was adjusted according to the physical dimensions of a voxel (0.45 μm *(X)* × 0.45 μm *(Y)* × scanning interval *(Z)*) to show each object in the imaging coordinate system (Figure 4.4).

Quantification of VSMC Nuclear Geometry

The orientation and lengths of each VSMC nucleus was automatically calculated using MATLAB® code. First, the centroid (X_c, Y_c, Z_c) of a VSMC nucleus composed of n voxels, which are located at (X_i, Y_i, Z_i) for $i = 1 \ldots n$, was computed using

$$X_c = \frac{1}{n}\sum_{i=1}^{n} X_i \,,\; Y_c = \frac{1}{n}\sum_{i=1}^{n} Y_i \,,\; Z_c = \frac{1}{n}\sum_{i=1}^{n} Z_i \,. \tag{4.2}$$

Z-stacks along each transmural path were joined by aligning the centroids of VSMC nuclear objects in the overlapped region. The intramural location of the centroid of each

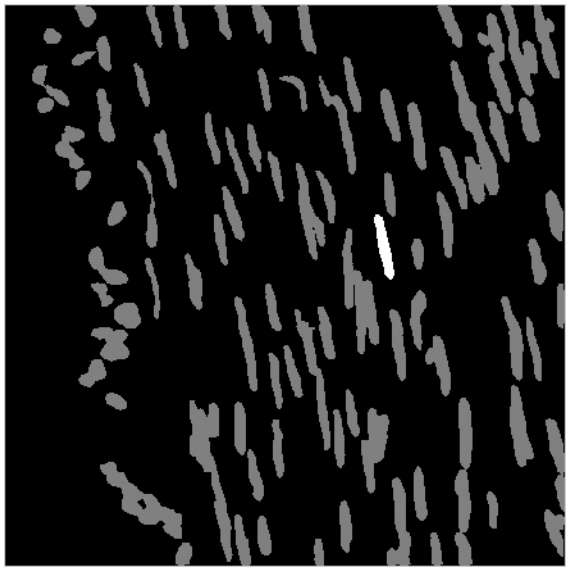

Figure 4.3: Two-dimensional visual representation of a Z-stack showing the projection of three-dimensional objects onto the imaging plane. A selected object is highlighted in white.

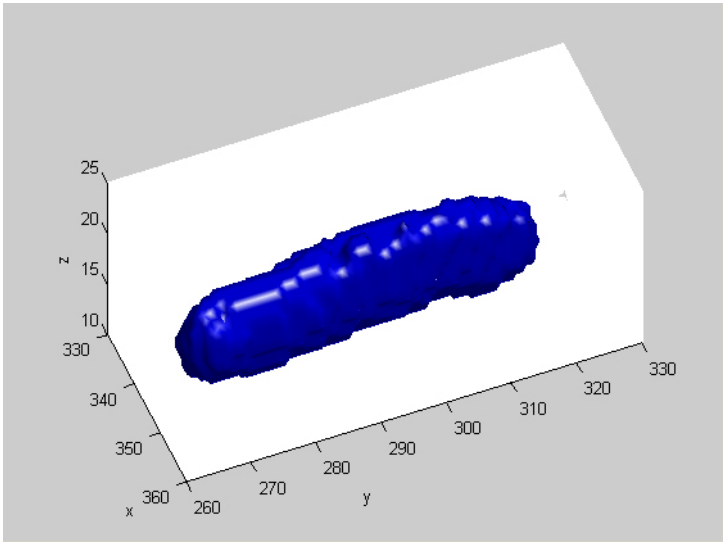

Figure 4.4: Three-dimensional visual representation of a selected object. The isosurface view of a selected object was plotted in voxel space with physical aspect ratio.

VSMC nucleus was computed in terms of normalized thickness, which is 0 at the intima and 1 at the outer boundary of the media.

Given the centroid of each VSMC nuclear object, the second-order moment of the voxels around the centroid forms a covariance tensor,

$$COV = \frac{1}{n}\sum_{i=1}^{n}\begin{bmatrix} (X_i - X_c)^2 & (X_i - X_c)(Y_i - Y_c) & (X_i - X_c)(Z_i - Z_c) \\ (X_i - X_c)(Y_i - Y_c) & (Y_i - Y_c)^2 & (Y_i - Y_c)(Z_i - Z_c) \\ (X_i - X_c)(Z_i - Z_c) & (Y_i - Y_c)(Z_i - Z_c) & (Z_i - Z_c)^2 \end{bmatrix}. \quad (4.3)$$

The eigenvalue problem for the covariance tensor was solved to get eigenvectors which define the principal axes of the VSMC nucleus:

$$(COV - \lambda I)v = 0, \quad (4.4)$$

where λ is the eigenvalue, and v is the eigenvector of the covariance matrix, and I is the identity matrix. The major axis of a VSMC nucleus was collinear with the eigenvector associated with the largest eigenvalue. The major axis length of a VSMC nucleus was measured as the length of a VSMC nucleus along the major axis.

The orientation of a VSMC nucleus was measured using a local coordinate system, where the θ-axis and r-axis on the transverse plane are aligned to the circumferential and radial directions of an arterial cross-section, respectively (Figure 4.5). Because each transmural path covers a small portion of an arterial cross-section, the intima appears to be linear. A vector tangential to the intima, and pointing counterclockwise, was computed by fitting a line to the centroids of endothelial cell nuclei. This approximates the circumferential direction and was normalized to define the

unit vector of the θ-axis ($\hat{\theta}$). The major axis of each VSMC nucleus was transformed to local coordinates (r, θ, z) using an affine transformation matrix as

$$\begin{bmatrix} e_r \\ e_\theta \\ e_z \end{bmatrix} = \begin{bmatrix} r_X & r_Y & 0 \\ \theta_X & \theta_Y & 0 \\ 0 & 0 & -1 \end{bmatrix} \begin{bmatrix} e_X \\ e_Y \\ e_Z \end{bmatrix}, \tag{4.5}$$

where (r_X, r_Y, 0), (θ_X, θ_Y, 0), and (0, 0, -1) are the unit vectors of the r-, θ-, and z-axis with respect to the imaging coordinate system (X, Y, Z), respectively, and (e_r, e_θ, e_z) and (e_X, e_Y, e_Z) are the unit vectors of the major axis of a VSMC nucleus in terms of the local coordinate system and the imaging coordinate system, respectively. The unit vector of the major axis of a VSMC nucleus was conditioned to point in the circumferential direction as

$$\hat{e} = \begin{cases} (e_r, e_\theta, e_z) & if\ e_\theta \geq 0 \\ (-e_r, -e_\theta, -e_z) & if\ e_\theta < 0 \end{cases}. \tag{4.6}$$

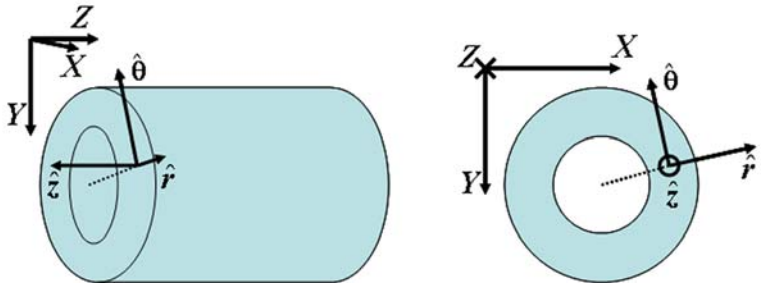

Figure 4.5: The imaging coordinate system (X, Y, Z) and the local coordinate system (r, θ, z) for VSMC nuclear objects. The local coordinate system is shown by unit vectors in the radial, circumferential, and axial directions.

Helical deviation, the angle between the unit vector of the θ-axis and the projection of the unit vector of the major axis onto θ*z*-plane, was computed using

$$\theta_h = \cos^{-1}\left(\frac{\hat{\theta}\cdot\left(\hat{r}\times\hat{e}\times\hat{r}\right)}{\left|\hat{\theta}\right|\left|\hat{r}\times\hat{e}\times\hat{r}\right|}\right), \tag{4.7}$$

where θ_h is the helical deviation ($0° \le \theta_h \le 90°$), and $\hat{r}$ is the unit vector of the *r*-axis. Radial deviation, the angle between the unit vector along the *r*-axis and the projection of the unit vector of the major axis onto *r*θ-plane, was computed using

$$\theta_r = \cos^{-1}\left(\frac{\hat{\theta}\cdot\left(\hat{z}\times\hat{e}\times\hat{z}\right)}{\left|\hat{\theta}\right|\left|\hat{z}\times\hat{e}\times\hat{z}\right|}\right), \tag{4.8}$$

where θ_r is the radial deviation ($0° \le \theta_h \le 90°$), and $\hat{z}$ is the unit vector of the *z*-axis. Helical and radial deviations do not provide information about the orientation of helices. The helical angle of a VSMC nucleus was defined as $+\theta_h$ for a right-handed helix and $-\theta_h$ for a left-handed helix. Also, the radial angle of a nucleus was defined as $+\theta_r$ for an outward spiral and $-\theta_r$ for an inward spiral (Figure 4.6).

The circumferential length (l_θ), defined as the projection of the major axis length of a VSMC nucleus onto the θ-axis, is given as

$$l_\theta = l_M\left(\hat{\theta}\cdot\hat{e}\right), \tag{4.9}$$

where l_M is the major axis length of a VSMC nucleus.

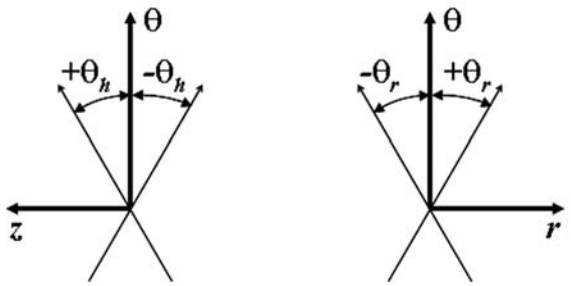

Figure 4.6: The sign convention for helical angle ($+\theta_h$ or $-\theta_h$) and radial angle ($+\theta_r$ or $-\theta_r$).

The stretch ratios of VSMC nuclei and arterial tissue in the circumferential direction were compared. Based on the observation by Fung (1984), the circumferential length of VSMC nuclei was assumed to be uniform through the wall thickness. The normalized circumferential stretch ratio of VSMC nuclei at 0 mmHg was determined by dividing the circumferential length at 100 mmHg by the circumferential length at 0 mmHg. For comparison purposes, the tissue level normalized circumferential stretch ratio at 0 mmHg with respect to the configuration at 100 mmHg was computed from previously conducted pressure-diameter experiments by Davis (2002).

Statistical Analysis

The transmural distributions of the major axis lengths, circumferential lengths, helical and radial deviations, and helical and radial angles for the 0 mmHg and 100 mmHg groups were analyzed visually and by computing the Spearman rank correlation coefficients, r_s. The means of each variable for the 0 mmHg and 100 mmHg groups were tested for the same means using the Wilcoxon rank sum test or the two-sample *t* test. The Wilcoxon rank sum test applied if sampled data for variables were not governed by a normal probability distribution. If both data sets being compared followed a normal distribution, the two-sample *t* test was used to compare the means. The probability distribution of each variable was tested for normality by performing the Lilliefors test and

visually checked using a histogram prior to the analysis. A *p*-value of 0.05 was considered as statistically significant in all cases.

Mechanical Model

A heterogeneous mechanical model of an arterial wall was developed based on the optical measurements of the two major ECM components, elastin and collagen. The heterogeneous model was used to compute local stresses in normal common carotid arteries from young pigs. An artery was considered as a thick-walled circular tube composed of two elastic incompressible materials, elastin and collagen, with residual strain at the no load state. Elastin and collagen were assumed to be responsible for the strength of the artery based on the previous observations (Torrance and Shwatz 1961; Conklin et al. 2002). The distributions of elastin and collagen, measured optically, were non-uniform across the arterial wall. Thus, the local mechanical property of an arterial wall was assumed to vary in proportion to the area fractions of elastin and collagen fibers.

Finite Deformation of Arteries

Opening Angle

The reference geometry for strains is the cross-section of a radially cut and opened arterial ring often referred to as the zero stress state (Chuong and Fung 1986). Due to the destructive nature of the method used to determine this state, residual strains could not be measured using the same arteries used in the organ culture. Hence, residual stretch ratios were measured from the same type of arteries (n = 13) as those used in the organ culture. The average opening angle computed using residual stretch ratios at the inner and outer boundaries of the arterial media was used to calculate strains through the arterial wall.

Digital images of porcine carotid arterial rings were taken before and after they were radially cut to relieve the residual stresses. The lengths of the inner and outer

boundaries of the media were digitally measured from the images. Assuming the geometries of unloaded and zero stress configurations to be a circular ring and a partial circular ring defined by an opening angle, respectively (Figure 4.7), the following relations are established.

$$\rho_i = \frac{s_i}{2\pi} \quad \text{and} \quad \rho_o = \frac{s_o}{2\pi}, \tag{4.10}$$

$$R_i = \frac{S_i}{2(\pi - \Phi)} \text{ and } \quad R_o = \frac{S_o}{2(\pi - \Phi)}, \tag{4.11}$$

where ρ_i and ρ_o are the inner and outer radii of the media at the unloaded state, s_i and s_o are the lengths of the inner and outer boundaries of the media at the unloaded state, R_i and R_o are the inner and outer radii of the media at the zero stress state, S_i and S_o are the lengths of the inner and outer boundaries of the media at the zero stress state, and Φ is the opening angle (Figure 4.7).

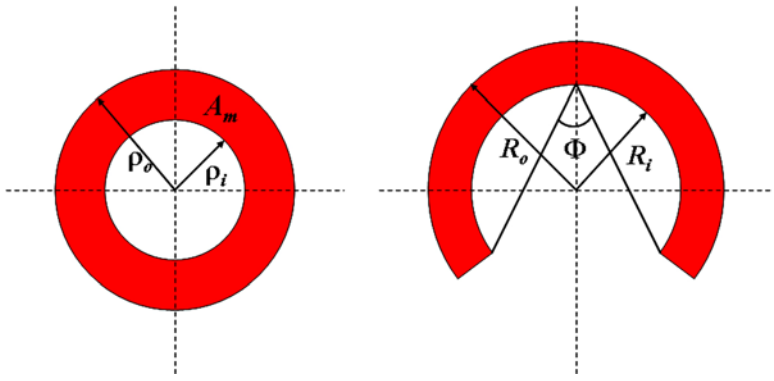

Figure 4.7: The cross-sectional configurations of unloaded state (left) and zero stress state (right).

Assuming incompressibility and no axial stretch, the cross-sectional areas at both states are the same as

$$A_m = \pi\left(\rho_o^2 - \rho_i^2\right) = \left(\pi - \Phi\right)\left(R_o^2 - R_i^2\right), \tag{4.12}$$

where A_m is the cross-sectional area of the media. Substituting equations 4.10 and 4.11 into equation 4.12 gives the opening angle,

$$\Phi = \pi\left(1 - \frac{S_o^2 - S_i^2}{s_o^2 - s_i^2}\right). \tag{4.13}$$

Strains of Elastin and Collagen

A point (R, Θ, Z) in the zero stress configuration is mapped to a point (r, θ, z) in the pressurized and axially stretched configuration (Figure 4.8) according to

$$r = r(R), \qquad \theta = \frac{\pi}{\pi - \Phi}\Theta, \qquad z = \lambda_z Z. \tag{4.14}$$

The deformation gradient, say F, that maps a point (R, Θ, Z) into a point (r, θ, z) in cylindrical coordinates is

$$\mathrm{F} = \begin{bmatrix} \frac{\partial r}{\partial R} & \frac{1}{R}\frac{\partial r}{\partial \Theta} & \frac{\partial r}{\partial Z} \\ r\frac{\partial \theta}{\partial R} & \frac{r}{R}\frac{\partial \theta}{\partial \Theta} & r\frac{\partial \theta}{\partial Z} \\ \frac{\partial z}{\partial R} & \frac{1}{R}\frac{\partial z}{\partial \Theta} & \frac{\partial z}{\partial Z} \end{bmatrix} = \begin{bmatrix} \frac{\partial r}{\partial R} & 0 & 0 \\ 0 & \frac{r}{R}\frac{\pi}{\pi - \Phi} & 0 \\ 0 & 0 & \lambda_z \end{bmatrix}. \tag{4.15}$$

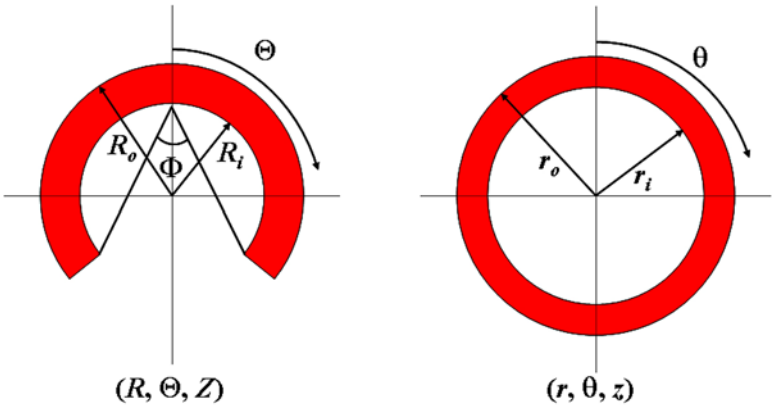

Figure 4.8: The cross-sections of arteries at zero stress configuration (left) and loaded configuration (right).

Hence, stretch ratios in the radial, circumferential, and axial directions are, respectively,

$$\lambda_r = \frac{\partial r}{\partial R}, \qquad \lambda_\theta = \frac{r}{R}\frac{\pi}{\pi - \Phi}, \qquad \text{and } \lambda_z. \tag{4.16}$$

The material is assumed to be incompressible (det F = 1), hence

$$\frac{\partial r}{\partial R}\frac{r}{R}\frac{\pi}{\pi - \Phi}\lambda_z = 1. \tag{4.17}$$

Integrating equation 4.17 yields

$$r^2 - r_i^2 = \frac{\pi - \Phi}{\pi \lambda_z}\left(R^2 - R_i^2\right), \tag{4.18}$$

where r_i is the inner radius of the deformed configuration.

Elastin provides structural support at all strains. Thus, the strain of elastin is equal to the strain of arterial tissue, which is defined by the principal components of the Green strain,

$$E_j = \frac{1}{2}\left(\lambda_j^2 - 1\right), \qquad \text{where j} = r, \theta, z. \tag{4.19}$$

Based on the histological observations, the structure of collagen fibers was modeled as left- and right-handed helices aligned at an angle of helical deviation (θ_h) with respect to the circumferential direction (Figure 4.9). Initially undulated collagen fibers become straightened once a strain along the helix reaches a 'recruiting point', which was assumed to vary through the arterial wall. Once straightened, collagen fibers become load-bearing and a stretch ratio along the helix (λ_h) is given as

$$\lambda_h = \frac{l}{l_0} = \frac{l}{l_{RP}}\frac{l_{RP}}{l_0} = \lambda_c \lambda_{RP}\,, \tag{4.20}$$

where l_0 is an undeformed length of a helix, l is a deformed length of a helix, l_{RP} is the length of a helix at a recruiting point, λ_{RP} is the stretch ratio along the helix at a recruiting point, and λ_c is the stretch ratio of collagen fibers. Since collagen fibers do not affect the opening angle (Greenwald et al. 1997), they are not straightened at the zero stress configuration. Thus, λ_{RP} is larger than one at any location in arterial tissue. With the assumption of variable recruiting points in the radial direction, λ_{RP} is a function of r and should be determined using additional assumptions. Hence, the stretch ratio and the strain of the stretched collagen fiber in the loaded state are

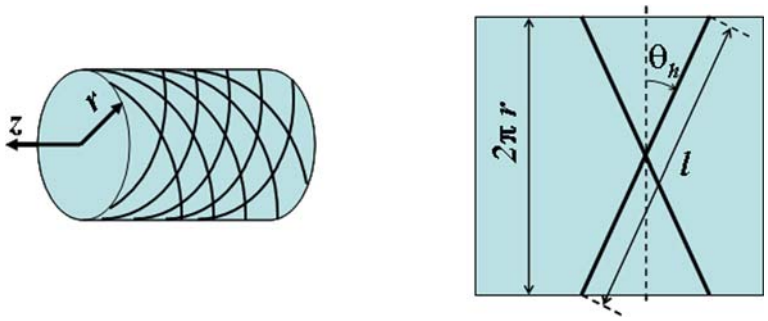

(A)

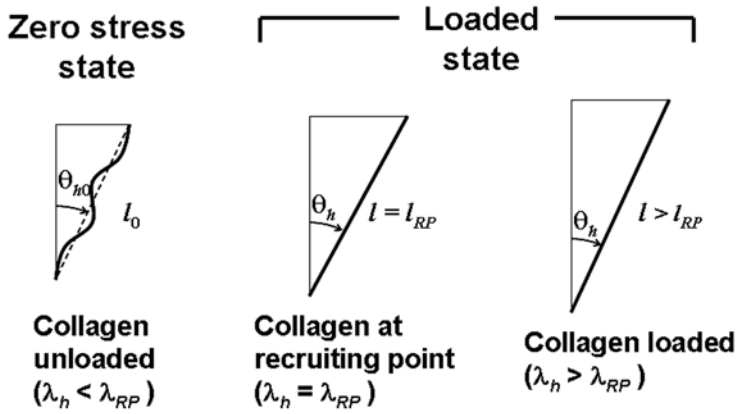

(B)

Figure 4.9: Balanced left- and right-helices of collagen fibers at *r* (A) and the configuration of a collagen fiber at zero stress state, recruiting point, and loaded state (B).

$$\lambda_c = \frac{\lambda_h}{\lambda_{RP}}, \qquad \text{for } \lambda_h > \lambda_{RP}, \text{ and} \tag{4.21}$$

$$E_c = \frac{1}{2}\left(\lambda_c^2 - 1\right), \tag{4.22}$$

where E_c is the strain of collagen fibers in the fiber direction. The square of a stretch ratio along the helix is

$$\lambda_h^2 = \lambda_\theta^2 \cos^2 \theta_{h0} + \lambda_z^2 \sin^2 \theta_{h0}, \tag{4.23}$$

where θ_{h0} is a helical deviation at the zero stress configuration (Figure 4.9). Substituting equation 4.23 into equation 4.21 yields

$$\lambda_c^2 = \frac{1}{\lambda_{RP}^2}\left(\lambda_\theta^2 \cos^2 \theta_{h0} + \lambda_z^2 \sin^2 \theta_{h0}\right). \tag{4.24}$$

Substituting equations 4.19 and 4.24 into equation 4.22 yields the Green strain of collagen fibers in terms of the tissue-level strains as

$$E_c = \frac{1}{2}\left(\frac{\cos^2 \theta_{h0}}{\lambda_{RP}^2}\left(2E_\theta + 1\right) + \frac{\sin^2 \theta_{h0}}{\lambda_{RP}^2}\left(2E_z + 1\right) - 1\right). \tag{4.25}$$

To determine the recruiting points across the wall thickness, unlike previous studies, collagen fibers were assumed to experience identical strain at physiological pressure and axial stretch. It is expected that strain in VSMCs are closely associated with strains in collagen fibers. Therefore, the introduced assumption implies that VSMCs are at uniform strain under physiological loading conditions, which is in agreement with the

experimental observations (Fung 1984). Also, the helical deviation of collagen fibers was assumed to be uniform through the arterial wall at physiological pressure and axial stretch. The assumption was validated by observing the orientation of VSMC nuclei fixed at physiological loading condition. Thus, helical deviation at zero stress configuration generally varies through the arterial wall. The cosine and sine of the helical deviation of loaded collagen fibers are

$$\cos\theta_h = \frac{\lambda_\theta \cos\theta_{h0}}{\lambda_c \lambda_{RP}}, \text{ and} \tag{4.26}$$

$$\sin\theta_h = \frac{\lambda_z \sin\theta_{h0}}{\lambda_c \lambda_{RP}}. \tag{4.27}$$

Strain Energy Functions

Elastin was assumed to be a neo-Hookean material (Holzapfel et al. 2002), for which the SEF is

$$W_e = \frac{c_e}{2}(I_1 - 3), \text{ where } I_1 = \lambda_r^2 + \lambda_\theta^2 + \lambda_z^2, \tag{4.28}$$

c_e is the material constant and I_1 is the first invariant of the Green strain tensor. Rewriting equation 4.28 in terms of the Green strain yields

$$W_e = c_e(E_r + E_\theta + E_z). \tag{4.29}$$

Undulated collagen fibers are not load-bearing and hence are assumed to store no strain energy. Once straightened, collagen fibers gradually stiffen the arterial wall and were modeled by an exponential SEF:

$$W_c = \begin{cases} 0 & \text{for } \lambda_h \le \lambda_{RP} \\ \dfrac{c_{c1}}{c_{c2}}\left[\exp\left(c_{c2}E_c^2\right)-1\right] & \text{for } \lambda_h > \lambda_{RP}, \end{cases} \tag{4.30}$$

where c_{c1} and c_{c2} are material constants for collagen fibers. Note that if c_{c2} is much smaller than 1,

$$\exp\left(c_{c2}E_c^2\right)-1 \approx c_{c2}E_c^2 \tag{4.31}$$

and W_c is a quadratic function of Green strain with coefficient c_{c1}.

Considering the arterial tissue as a constrained mixture, the SEF of an arterial wall is the sum of the SEFs of elastin and collagen fibers weighted by area fractions of each component:

$$W = f_e W_e + f_c W_c, \tag{4.32}$$

where f_e and f_c are the area fractions of elastin and collagen fibers, respectively. The distributions of elastin and collagen fibers were observed to be heterogeneous through the arterial wall. With the axisymmetric assumption, the area fractions of elastin and collagen fibers vary solely along the radial direction.

Stress Response

The Cauchy stresses in the matrix of elastin and collagen fibers are calculated by

$$\sigma_j = -p + \lambda_j^2 \frac{\partial W}{\partial E_j}, \quad \text{where j} = r, \theta, z, \tag{4.33}$$

and p is a Lagrange multiplier enforcing the incompressibility constraint. Substituting equation 4.32 into equation 4.33 yields

$$\sigma_j = -p + f_e \lambda_j^2 \frac{\partial W_e}{\partial E_j} + f_c \lambda_j^2 \frac{\partial W_c}{\partial E_c} \frac{\partial E_c}{\partial E_j}, \qquad \text{where j = } r, \theta, z. \tag{4.34}$$

Substituting equations 4.25, 4.29, and 4.30 into equation 4.34 yields the normal stresses in the arterial tissue:

$$\sigma_r = -p + f_e c_e \lambda_r^2, \tag{4.35}$$

$$\sigma_\theta = -p + f_e c_e \lambda_\theta^2 + 2 f_c c_{c1} \exp\left(c_{c2} E_c^2\right) E_c \lambda_\theta^2 \frac{\cos^2 \theta_{h0}}{\lambda_{RP}^2}, \tag{4.36}$$

$$\sigma_z = -p + f_e c_e \lambda_z^2 + 2 f_c c_{c1} \exp\left(c_{c2} E_c^2\right) E_c \lambda_z^2 \frac{\sin^2 \theta_{h0}}{\lambda_{RP}^2}. \tag{4.37}$$

Equations 4.35 – 4.37 can be rewritten with stretch ratios and the sine and cosine of the helical deviation at the deformed configuration. Substituting equations 4.22, 4.26, and 4.27 into equations 4.35 – 4.37 yields

$$\sigma_r = -p + f_e c_e \lambda_r^2, \tag{4.38}$$

$$\sigma_\theta = -p + f_e c_e \lambda_\theta^2 + f_c c_{c1} \exp\left(\frac{c_{c2}}{4}\left(\lambda_c^2 - 1\right)^2\right)\left(\lambda_c^2 - 1\right)\lambda_c^2 \cos^2 \theta_h, \tag{4.39}$$

$$\sigma_z = -p + f_e c_e \lambda_z^2 + f_c c_{c1} \exp\left(\frac{c_{c2}}{4}\left(\lambda_c^2 - 1\right)^2\right)\left(\lambda_c^2 - 1\right)\lambda_c^2 \sin^2 \theta_h. \tag{4.40}$$

Noting that stretch ratios and the fractions of elastin and collagen fibers vary only with r, the equations of equilibrium read as

$$\frac{\partial \sigma_r}{\partial r} + \frac{\sigma_r - \sigma_\theta}{r} = 0\,, \quad \frac{\partial p}{\partial \theta} = 0\,, \qquad \frac{\partial p}{\partial z} = 0\,. \tag{4.41}$$

Thus, the Lagrange multiplier, p, is a function of r. Integrating equation 4.41 yields

$$\sigma_r(r) - \sigma_r(r_i) = \int_{r_i}^{r} (\sigma_\theta - \sigma_r)\frac{dr}{r}, \tag{4.42}$$

where $\sigma_r(r_i) = -P$, the luminal pressure measured as a gauge pressure. Rearranging equation 4.42 gives the transmural variation of the Lagrange multiplier, p, as a function of r:

$$\begin{aligned} p(r) = P + & f_e c_e \lambda_r^2 \\ & - \int_{r_i}^{r} \left(f_e c_e \left(\lambda_\theta^2 - \lambda_r^2\right) + f_c c_{c1} \exp\left(\frac{c_{c2}}{4}\left(\lambda_c^2 - 1\right)^2 \right) \left(\lambda_c^2 - 1\right) \lambda_c^2 \cos^2 \theta_h \right) \frac{dr}{r}. \end{aligned} \tag{4.43}$$

The outer pressure measured as a gauge pressure is typically taken to be zero. Thus, $\sigma_r(r_o) = 0$ yields

$$P = \int_{r_i}^{r_o} \left(f_e c_e \left(\lambda_\theta^2 - \lambda_r^2\right) + f_c c_{c1} \exp\left(\frac{c_{c2}}{4}\left(\lambda_c^2 - 1\right)^2 \right) \left(\lambda_c^2 - 1\right) \lambda_c^2 \cos^2 \theta_h \right) \frac{dr}{r}, \tag{4.44}$$

where r_o is the outer radius of the deformed configuration. Equation 4.44 includes four unknown variables, c_e, c_{c1}, c_{c2}, and λ_c at P_i = 100 mmHg and λ_z = 1.5.

Implementation of Heterogeneous Model

The transverse cross-section of arterial tissue, including the internal elastic lamina (IEL), the media, and the EEL, was modeled as a multi-layered tube composed of 51 concentric layers. The thickness of each layer was about 11 μm representing approximately half of the width of a VSMC (Todd et al. 1983). The average pixel intensities of elastin and collagen fibers in each layer were assumed to be proportional to the area fraction of each component:

$$f_{ki} = \alpha_k I_{ki}, \tag{4.45}$$

where k is e for elastin or c for collagen fibers, f_{ki} is the area fraction of elastin or collagen fibers in the i^{th} layer, and α_k is the constant of proportionality for elastin or collagen fibers.

The area-weighted average of the area fraction of elastin (or collagen fibers) in each layer yields the area fraction of elastin (or collagen fibers) in the arterial wall:

$$F_k = \frac{\sum_{i=1}^{51} f_{ki} A_i}{\sum_{i=1}^{51} A_i}, \tag{4.46}$$

where A_i is the area of the i^{th} layer, and F_k is the area fraction of elastin or collagen fibers in the arterial wall. Likewise, the area-weighted average of the pixel intensity of elastin (or collagen fibers) in each layer yields the average pixel intensity of elastin (or collagen fibers) at the tissue level:

$$\bar{I}_k = \frac{\sum_{i=1}^{51} I_{ki} A_i}{\sum_{i=1}^{51} A_i}, \tag{4.47}$$

where $\bar{I}_k$ is the average pixel intensity of elastin or collagen fibers in the arterial wall. Substituting equations 4.45 and 4.47 into equation 4.46 gives

$$F_k = \alpha_k \bar{I}_k . \tag{4.48}$$

Then, substituting equation 4.48 into equation 4.45 yields

$$f_{ki} = F_k \frac{I_{ki}}{\bar{I}_k} . \tag{4.49}$$

The pixel intensities of elastin and collagen fibers were normalized using

$$I'_{ki} = \frac{I_{ki}}{\bar{I}_k}, \tag{4.50}$$

where I'_{ki} is the normalized pixel intensity of elastin (or collagen fibers) in the i^{th} layer, and the area-weighted average of I'_{ki} yields one. Thus, the area fraction of each component in the i^{th} layer is decoupled into tissue-level area fraction and normalized distribution of each component.

The proportionality constant, α_k, varies from section to section depending on the conditions for staining and imaging. For elastin imaging, this is attributable to the opacity of the embedding medium and photo bleaching of the sections. For the images of

collagen fibers, this is due to the variability of sectioning and staining conditions. The setting of a microscope such as exposure time also affects pixel intensity. Thus the area fractions of elastin and collagen fibers cannot be measured precisely using methods used in this study. The area fractions are coupled with material constants in the constitutive equation. Thus, they can not be optimized unless material constants are given. Hence, area fractions and material constants were optimized together as area fraction-weighted material constants:

$$c_e' = F_e c_e , \tag{4.51}$$

$$c_{c1}' = F_c c_{c1} . \tag{4.52}$$

where c_e' and c_{c1}' are the area fraction-weighted material constants for elastin and collagen fibers, respectively.

Rewriting equation 4.44 in a discrete form gives

$$\begin{aligned} P = {} & c_e' \sum_{i=1}^{51} I_{ei}' \left(\lambda_{\theta i}^2 - \lambda_{ri}^2 \right) \frac{t_i}{\bar{r}_i} \\ & + c_{c1}' \sum_{i=1}^{51} I_{ci}' \exp\left(\frac{c_{c2}}{4} \left(\lambda_{ci}^2 - 1 \right)^2 \right) \left(\lambda_{ci}^2 - 1 \right) \lambda_{ci}^2 \cos^2 \theta_{hi} \frac{t_i}{\bar{r}_i} \end{aligned} , \tag{4.53}$$

where $\lambda_{\theta i}$ and λ_{ri} are circumferential and radial stretch ratios in the i^{th} layer, λ_{ci} is the stretch ratio of collagen fibers in the i^{th} layer, θ_{hi} is the helical deviation in the i^{th} layer, t_i is the thickness of the i^{th} layer, and $\bar{r}_i$ is the mean radius of the i^{th} layer.

The average of previously reported pressure-diameter relations (n = 9) of healthy porcine carotid arteries prior to the organ culture (Davis 2002) was used to determine stretch ratios at various pressures assuming incompressibility. The pressure-diameter

relationship was measured using arteries stretched to *in vivo* length (λ_z = 1.5) at ten pressure points between 0 mmHg and 120 mmHg. The error at each data point associated with regression analysis was defined as the difference between experimentally measured pressure and computed pressure at measured diameter using the model:

$$e = P_{\exp} - P_{theory}\,, \tag{4.54}$$

where P_{exp} is the luminal pressure measured experimentally at each data point, and P_{theory} is the luminal pressure computed using the model at each data point. Thus, force equilibrium at each of ten pressure-diameter data points gives

$$\begin{aligned} P_{\exp} = {} & c_e' \sum_{i=1}^{51} I_{ei}' \left(\lambda_{\theta i}^2 - \lambda_{ri}^2\right) \frac{t_i}{\bar{r}_i} \\ & + c_{c1}' \sum_{i=1}^{51} I_{ci}' \exp\left(\frac{c_{c2}}{4}\left(\lambda_{ci}^2 - 1\right)^2\right)\left(\lambda_{ci}^2 - 1\right)\lambda_{ci}^2 \cos^2\theta_{hi} \frac{t_i}{\bar{r}_i} + e \end{aligned}\,. \tag{4.55}$$

Equation 4.55 forms a mathematical model for multivariate nonlinear regression with ten pairs of pressure-diameter data points. Using both numerical and analytical methods, four unknown parameters, a material constant for elastin (c_e'), material constants for collagen fibers (c_{c1}' and c_{c2}), and uniform stretch ratio of collagen fibers (λ_c) at P_i = 100 mmHg and λ_z = 1.5 were optimized by minimizing the error function (Ω) defined as

$$\Omega = \sum e^2 = \sum (P_{\exp} - P_{theory})^2\,. \tag{4.56}$$

With optimized parameters for each artery, the transmural distributions of stresses were calculated for static luminal pressure equal to the mean pressure of each artery during organ culture. First, the Lagrange multiplier of the i^{th} layer was computed:

$$p_i = P + c_e' I_{ei}' \lambda_{ri}^2 - \sum_{l=1}^{i} \left(c_e' I_{el}' \left(\lambda_{\theta l}^2 - \lambda_{rl}^2 \right) + c_{c1}' I_{cl}' \exp\left(\frac{c_{c2}}{4} \left(\lambda_{cl}^2 - 1 \right)^2 \right) \left(\lambda_{cl}^2 - 1 \right) \lambda_{cl}^2 \cos^2 \theta_{hl} \right) \frac{t_l}{\bar{r}_l}, \quad (4.57)$$

where p_i is the Lagrange multiplier of the i^{th} layer. Then, the normal stresses in the i^{th} layer are

$$\sigma_{ri} = -p_i + c_e' I_{ei}' \lambda_{ri}^2, \quad (4.58)$$

$$\sigma_{\theta i} = -p_i + c_e' I_{ei}' \lambda_{\theta i}^2 + c_{c1}' I_{ci}' \exp\left(\frac{c_{c2}}{4} \left(\lambda_{ci}^2 - 1 \right)^2 \right) \left(\lambda_{ci}^2 - 1 \right) \lambda_{ci}^2 \cos^2 \theta_{hi}, \quad (4.59)$$

$$\sigma_{zi} = -p_i + c_e' I_{ei}' \lambda_{zi}^2 + c_{c1}' I_{ci}' \exp\left(\frac{c_{c2}}{4} \left(\lambda_{ci}^2 - 1 \right)^2 \right) \left(\lambda_{ci}^2 - 1 \right) \lambda_{ci}^2 \sin^2 \theta_{hi}, \quad (4.60)$$

where σ_{ri}, $\sigma_{\theta i}$, and σ_{zi} are normal stresses of the i^{th} layer in the radial, circumferential, and axial directions, respectively.

Homogeneous Model

A comparable model assuming homogeneous structure across the arterial wall was also formulated and analyzed. The distributions of elastin and collagen fibers were assumed to be uniform across the arterial wall for the homogeneous model:

$$I_e' = 1, \quad (4.61)$$

$$I_c' = 1. \quad (4.62)$$

In contrast to the heterogeneous model, previously developed structure-based models utilized a single collagen recruiting function to model the recruitment of collagen fibers. In other words, they assumed that a 'recruiting point' does not vary through the thickness (Wuyts et al. 1995; Zulliger et al. 2004). Thus, unknown parameters for the homogeneous model are a material constant for elastin (c'_e), material constants for collagen fibers (c'_{c1} and c_{c2}), and the constant recruiting point of collagen fibers (λ_{RP}). These parameters were optimized by minimizing the error function, equation 4.55. The distributions of stresses were calculated for static luminal pressure equal to the mean pressure of each artery during organ culture using equations 4.57 – 4.60.

Statistical Analysis

The hypothesis that local stress distribution correlates to the distributions of the expression and activation of MMP-2 and MMP-9 was tested by calculating the Spearman rank correlation coefficients (r_s) between the computed circumferential stress using the heterogeneous or the homogeneous model and MMP-2 positive stained area fraction, MMP-9 positive stained area fraction, or substrate (gelatin) lysis area fraction for each specimen. Groups of correlation coefficients were tested for zero mean using the single-sample Student's t-test. Because the correlation coefficients are not normally distributed, they were transformed with the Fisher transformation and considered as samples from normal distribution with unknown mean and variance. A *p*-value of 0.05 was considered as statistically significant in all cases.

CHAPTER 4

RESULTS

Distributions of Expression and Activation of MMP-2 and MMP-9

The expressions of MMP-2 and MMP-9 were mostly localized near the IEL, the outer media, and the EEL (Figure 5.1A and B, respectively). The activities of MMP-2 and MMP-9 were mostly localized in the outer media and the EEL (Figure 5.1C). In the IEL and the inner media, the gelatinolytic activities were weak. The area fractions of pixels positively stained for MMP-2 or MMP-9 and substrate lysis in each layer were plotted against the normalized thickness for the normotensive group (Figure 5.2 – 5.6) and the hypertensive group (Figure 5.7 – 5.10). The expression of MMP-2 increased toward the outer layer in both normotensive arteries (r_s = 0.79; p < 0.01; n = 5) and hypertensive arteries (r_s = 0.84; p < 0.01; n = 4). The expression of MMP-9 also increased toward the outer layer in both normotensive arteries (r_s = 0.56; p = 0.01; n = 5) and hypertensive arteries (r_s = 0.69; p < 0.01; n = 4). The gelatinolytic activities increased toward the outer layer in all arteries incubated at either 100 mmHg (r_s = 0.86; p < 0.01; n = 5) or 200 mmHg (r_s = 0.83; p < 0.01; n = 4). Spearman rank correlation coefficients for each artery are listed in Table 5.1.

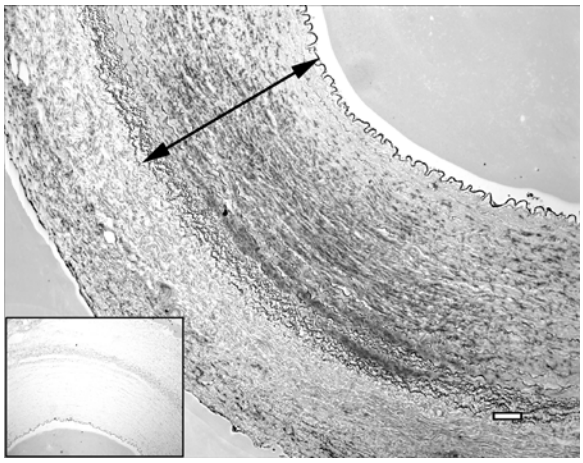

(A)

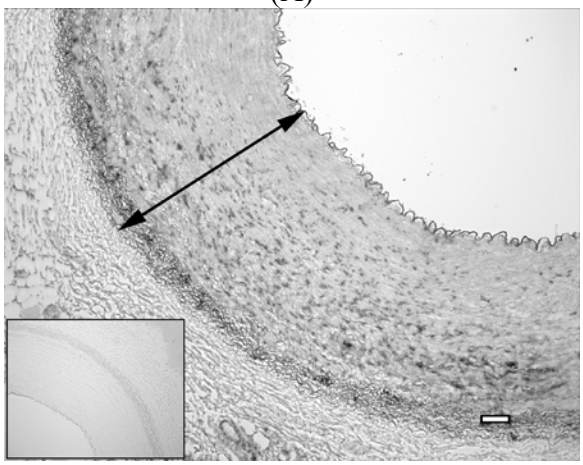

(B)

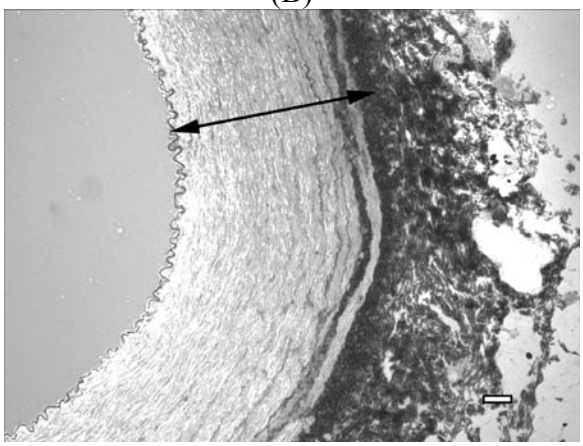

(C)

Figure 5.1: Representative images of the immunostaining for MMP-2 (A) and MMP-9 (B), where areas positively stained for MMP-2 and MMP-9 appear to be dark gray-black. A representative image of *in situ* zymography (C) showing localized gelatinolytic activities that are dark regions in the image. Arrows indicate one normalized thickness, which is from the IEL to the EEL. Bars = 100μm.

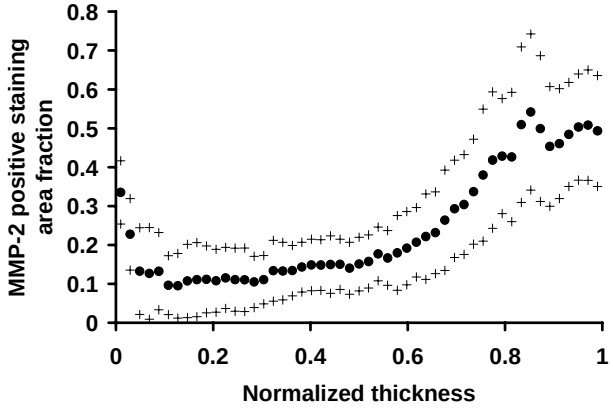

(A)

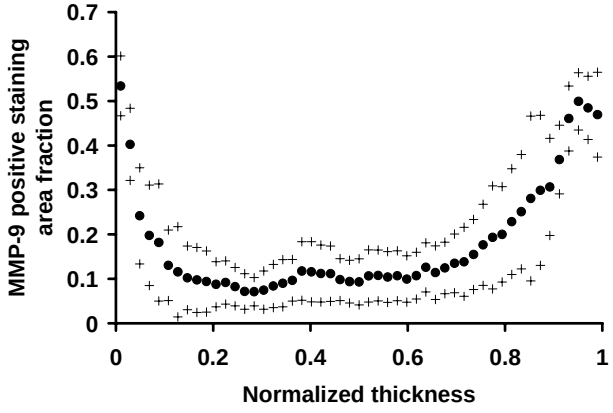

(B)

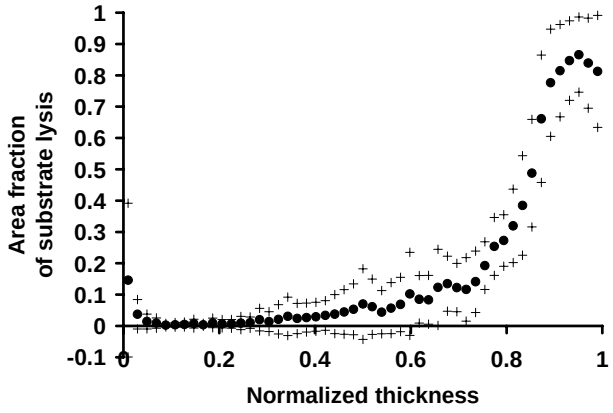

(C)

Figure 5.2: The average area fractions of pixels positively immunostained for MMP-2 (n = 14) (A) and MMP-9 (n = 8) (B) and substrate lysis due to gelatinolytic activities (n = 8) (C) in each layer were plotted against the normalized thickness as mean (●) ± S.D. (+) for sample #1001 (normotensive).

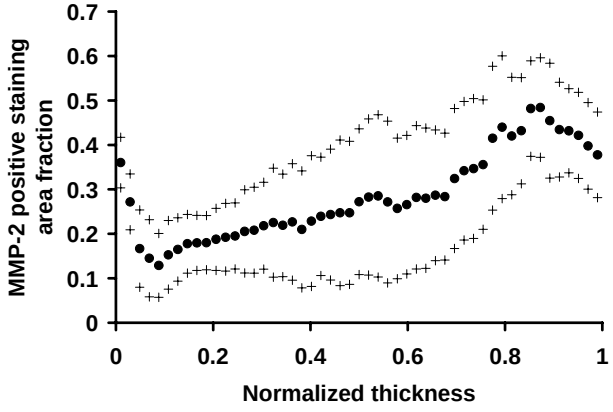

(A)

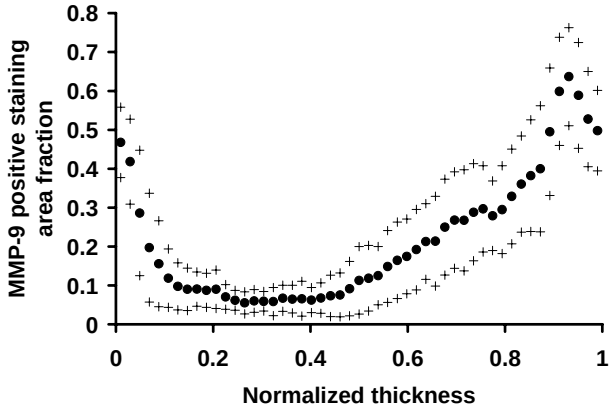

(B)

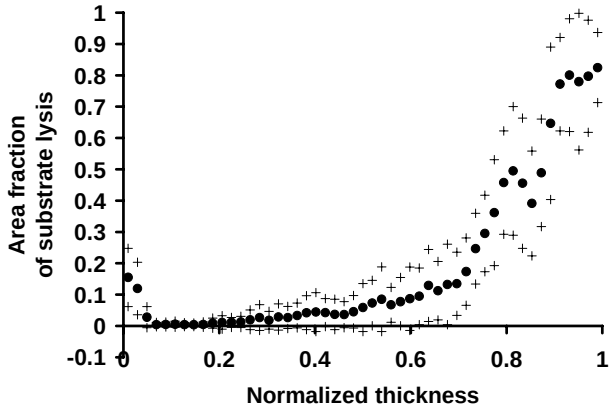

(C)

Figure 5.3: The average area fractions of pixels positively immunostained for MMP-2 (n = 15) (A) and MMP-9 (n = 18) (B) and substrate lysis due to gelatinolytic activities (n = 12) (C) in each layer were plotted against the normalized thickness as mean (●) ± S.D. (+) for sample #1002 (normotensive).

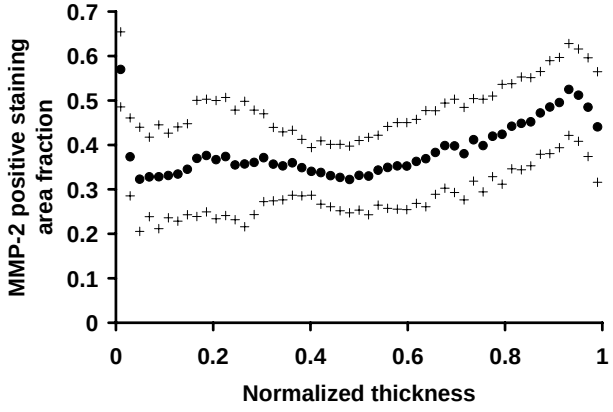

(A)

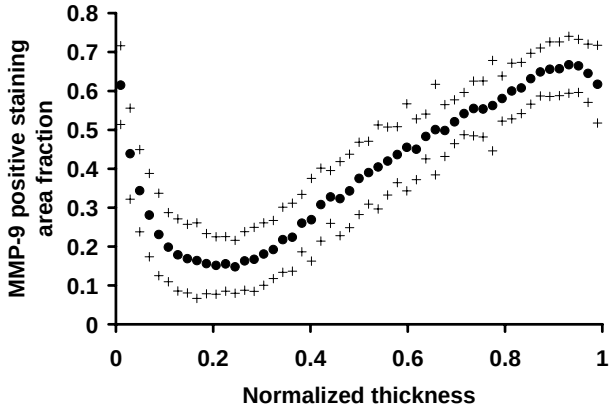

(B)

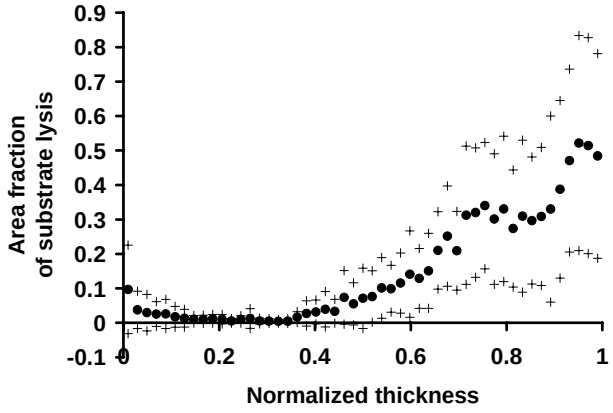

(C)

Figure 5.4: The average area fractions of pixels positively immunostained for MMP-2 (n = 17) (A) and MMP-9 (n = 22) (B) and substrate lysis due to gelatinolytic activities (n = 11) (C) in each layer were plotted against the normalized thickness as mean (●) ± S.D. (+) for sample #1003 (normotensive).

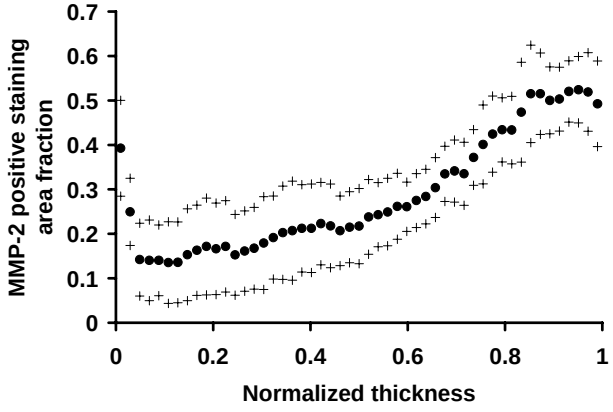

(A)

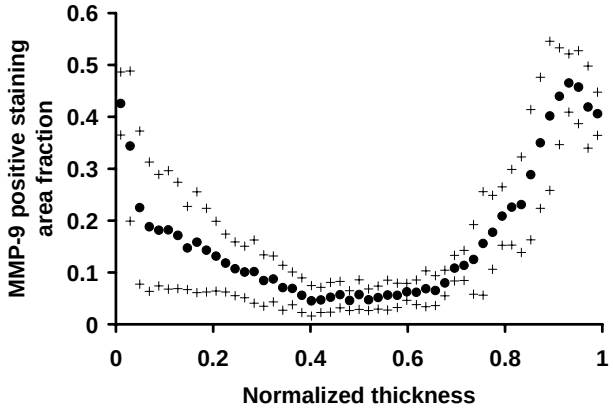

(B)

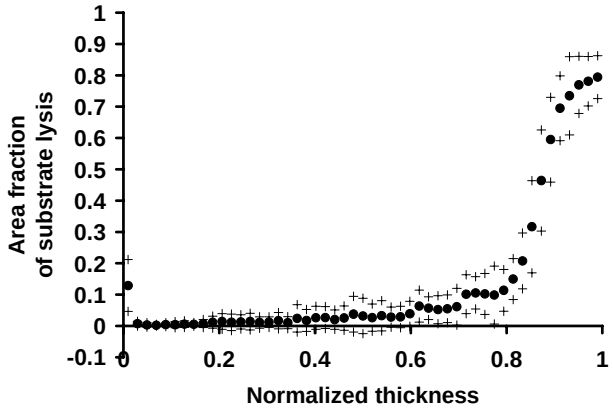

(C)

Figure 5.5: The average area fractions of pixels positively immunostained for MMP-2 (n = 14) (A) and MMP-9 (n = 8) (B) and substrate lysis due to gelatinolytic activities (n = 11) (C) in each layer were plotted against the normalized thickness as mean (●) ± S.D. (+) for sample #1004 (normotensive).

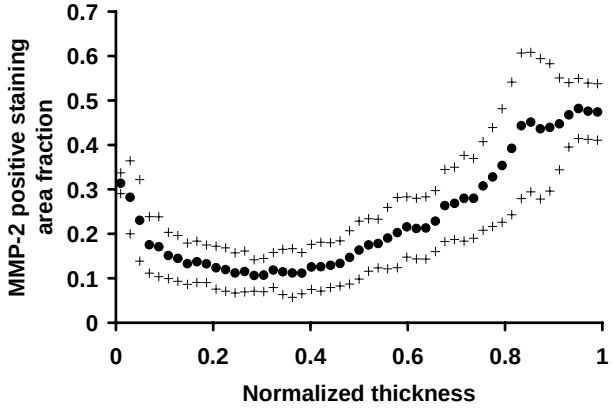

(A)

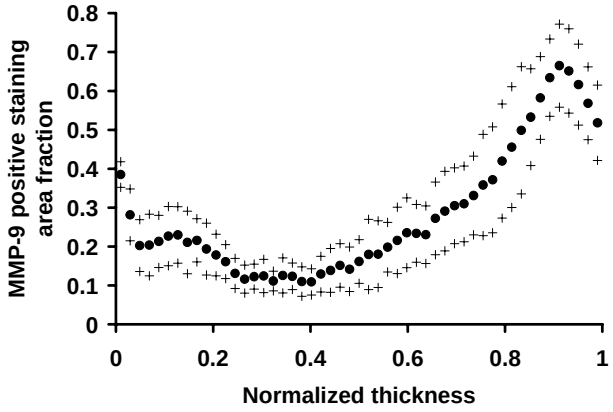

(B)

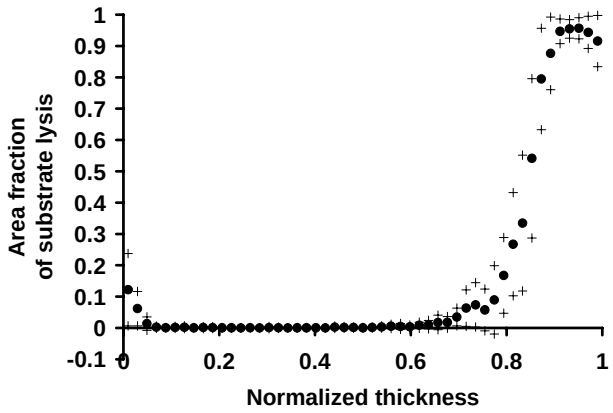

(C)

Figure 5.6: The average area fractions of pixels positively immunostained for MMP-2 (n = 15) (A) and MMP-9 (n = 10) (B) and substrate lysis due to gelatinolytic activities (n = 12) (C) in each layer were plotted against the normalized thickness as mean (●) ± S.D. (+) for sample #1005 (normotensive).

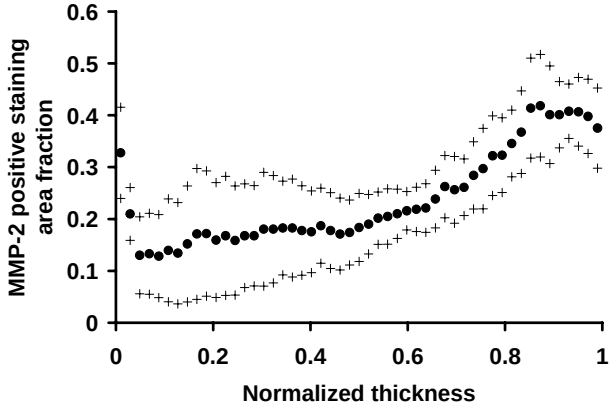

(A)

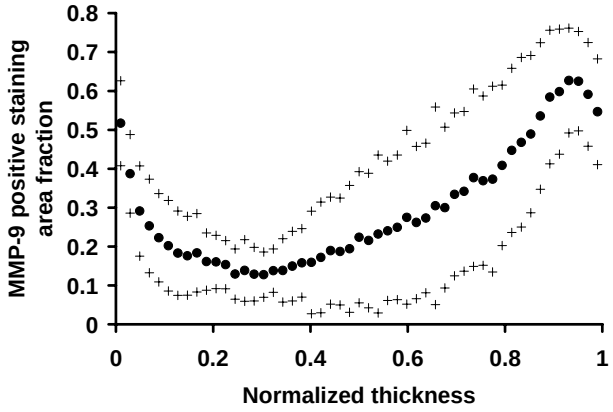

(B)

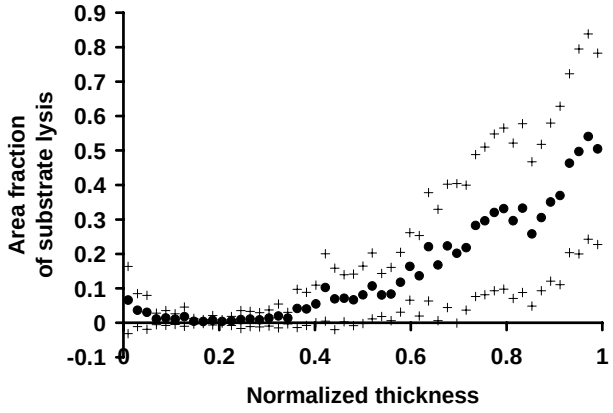

(C)

Figure 5.7: The average area fractions of pixels positively immunostained for MMP-2 (n = 13) (A) and MMP-9 (n = 12) (B) and substrate lysis due to gelatinolytic activities (n = 10) (C) in each layer were plotted against the normalized thickness as mean (●) ± S.D. (+) for sample #2001 (hypertensive).

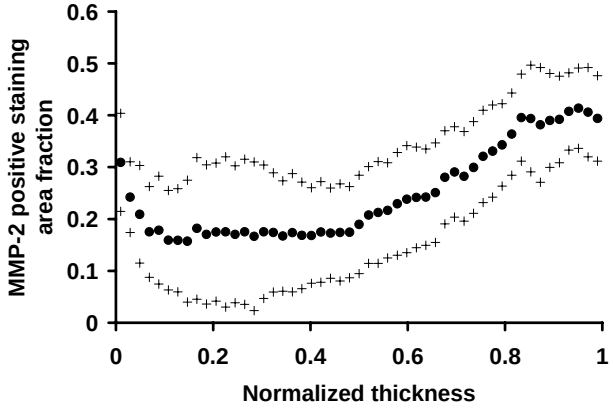

(A)

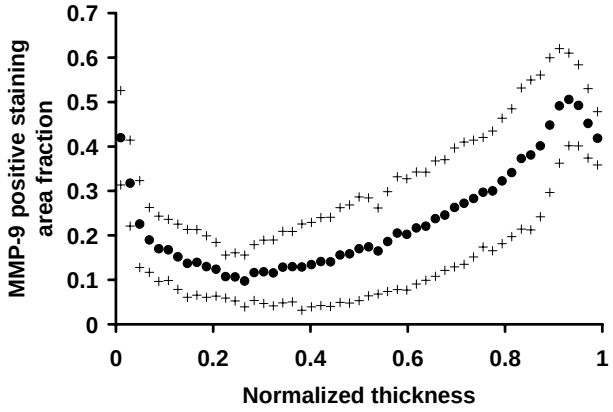

(B)

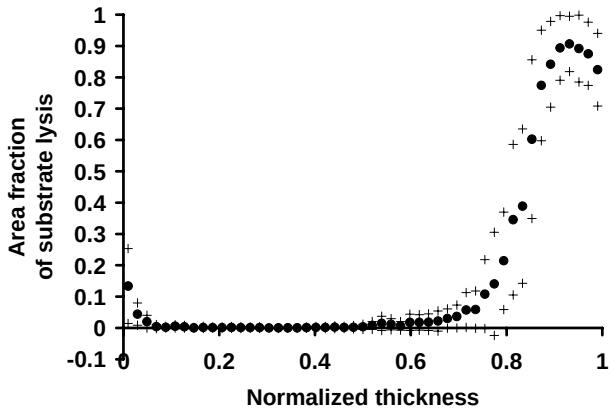

(C)

Figure 5.8: The average area fractions of pixels positively immunostained for MMP-2 (n = 13) (A) and MMP-9 (n = 12) (B) and substrate lysis due to gelatinolytic activities (n = 11) (C) in each layer were plotted against the normalized thickness as mean (●) ± S.D. (+) for sample #2002 (hypertensive).

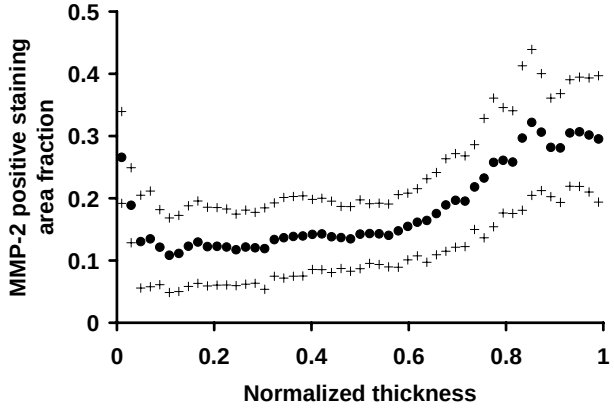

(A)

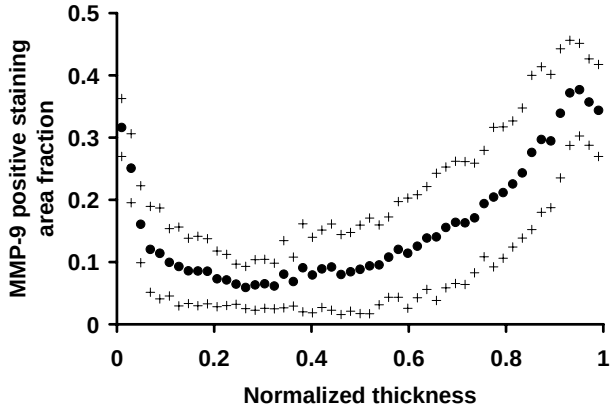

(B)

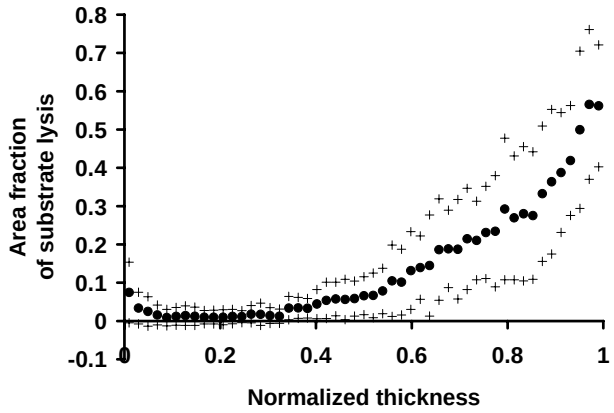

(C)

Figure 5.9: The average area fractions of pixels positively immunostained for MMP-2 (n = 13) (A) and MMP-9 (n = 12) (B) and substrate lysis due to gelatinolytic activities (n = 11) (C) in each layer were plotted against the normalized thickness as mean (●) ± S.D. (+) for sample #2003 (hypertensive).

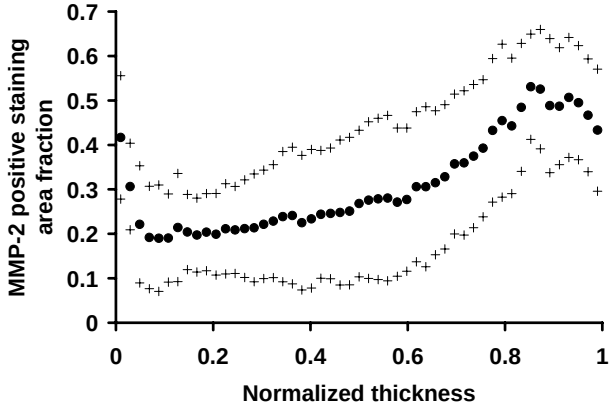

(A)

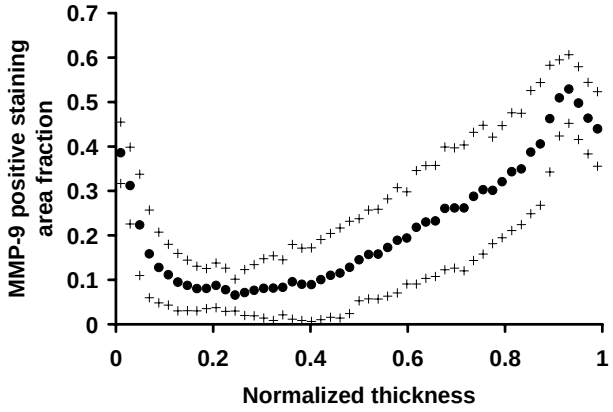

(B)

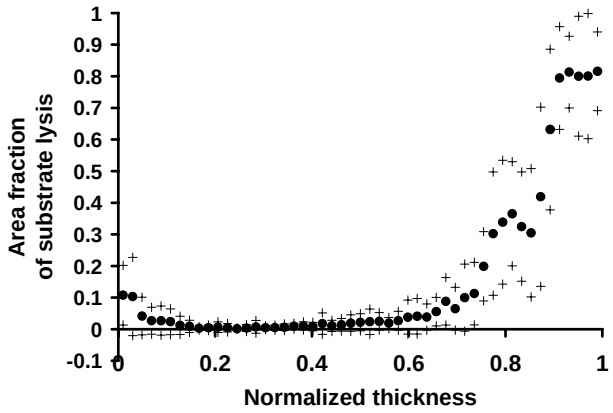

(C)

Figure 5.10: The average area fractions of pixels positively immunostained for MMP-2 (n = 13) (A) and MMP-9 (n = 12) (B) and substrate lysis due to gelatinolytic activities (n = 11) (C) in each layer were plotted against the normalized thickness as mean (●) ± S.D. (+) for sample #2004 (hypertensive).

Table 5.1: Spearman rank correlation coefficients (r_s) between normalized thickness and the expression and activation of MMP-2 and MMP-9 in normotensive arteries (#1001 – #1005) and hypertensive arteries (#2001 – #2004). All correlations were statistically significant except *one case.

Specimen	MMP-2 expression vs. normalized thickness (r_s)	MMP-9 expression vs. normalized thickness (r_s)	Gelatinolytic activity vs. normalized thickness (r_s)
#1001	0.8586 ($p < 0.01$)	0.4767 ($p < 0.01$)	0.9001 ($p < 0.01$)
#1002	0.8757 ($p < 0.01$)	0.6173 ($p < 0.01$)	0.8828 ($p < 0.01$)
#1003	0.6219 ($p < 0.01$)	0.8170 ($p < 0.01$)	0.8734 ($p < 0.01$)
#1004	0.8907 ($p < 0.01$)	0.2179 ($p = 0.06$)*	0.9119 ($p < 0.01$)
#1005	0.7079 ($p < 0.01$)	0.6545 ($p < 0.01$)	0.7070 ($p < 0.01$)
#2001	0.8658 ($p < 0.01$)	0.6896 ($p < 0.01$)	0.9285 ($p < 0.01$)
#2002	0.7805 ($p < 0.01$)	0.6895 ($p < 0.01$)	0.7255 ($p < 0.01$)
#2003	0.8293 ($p < 0.01$)	0.6420 ($p < 0.01$)	0.9309 ($p < 0.01$)
#2004	0.8646 ($p < 0.01$)	0.7319 ($p < 0.01$)	0.7304 ($p < 0.01$)

Distributions of Elastin and Collagen Fibers

The transmural distributions of elastin and collagen fibers in the arteries fixed at *in vivo* length ($\lambda_z = 1.5$) and mean incubating pressure, 100 mmHg for the normotensive group and 200 mmHg for the hypertensive group, were acquired from the images of each component.

A representative image of elastin shows the IEL with strong autofluorescence along with thin elastin lamellae between VSMC layers (Figure 5.11A). The EEL was thick and composed of rather discontinuous elastin fragments. Elastin was not observed in the adventitia. Although elastin lamellae were discretely distributed through the media, they were continuously branching and merging through the circumference of the artery. The average pixel intensity, which is proportional to the area fraction, of elastin in each layer was mostly uniform in the media with a small increase near the outer boundary of the media and high in the IEL and the EEL in normotensive arteries (Figure 5.12A –

5.16A) and hypertensive arteries (Figure 5.17A – 5.20A). Although the pixel intensity of elastin in each layer peaked at the IEL, it generally increased toward the outer layer in arteries fixed at either 100 mmHg (r_s = 0.48; p = 0.03; n = 5) or 200 mmHg (r_s = 0.38; p = 0.01; n = 4). The distributions of elastin were similar between specimens fixed at 100 mmHg and those fixed at 200 mmHg. Though the pattern of the distribution was consistent among the specimens, the overall luminance of elastin autofluorescence varied among sections due to the varying opacity of the embedding medium.

A representative image of collagen fibers shows that the strongest birefringence is detected in the adventitia mainly due to its high content of structural collagen type I fibers, which were mostly observed as thick and long fiber bundles (Figure 5.11B). Although the birefringence of collagen fibers was high in the EEL, they were discontinuous and fragmented unlike in the adventitia. In the media, most of collagen fibers were located near elastin lamellae, but they were, unlike the elastin lamellae, mostly discontinuous. The average pixel intensity, which is proportional to the area fraction, of collagen fibers in each layer was greatest near the EEL with a small peak in the IEL in normotensive arteries (Figure 5.12B – 5.16B) and hypertensive arteries (Figure 5.16B – 5.20B). The distribution of collagen fibers was relatively uniform in the inner media and gradually increased toward the outer layer. The pixel intensity of collagen fibers in each layer increased toward the outer layer in arteries fixed at either 100 mmHg (r_s = 0.69; p = 0.02; n = 5) or 200 mmHg (r_s = 0.87; p < 0.01; n = 4). Spearman rank correlation coefficients for each artery are listed in Table 5.2.

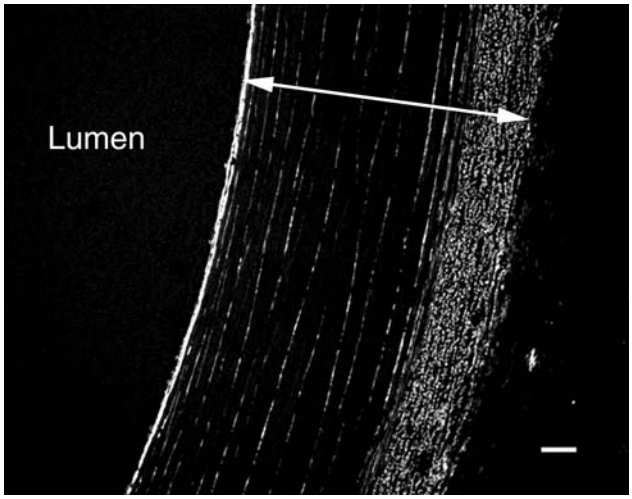

(A)

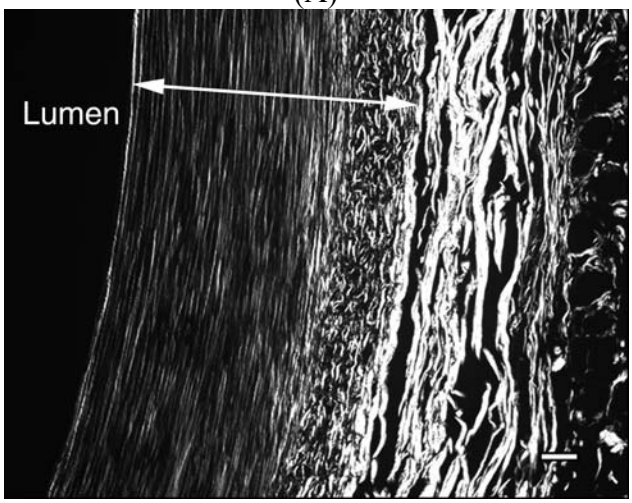

(B)

Figure 5.11: Representative images of elastin (A) and collagen fibers (B) taken from the arteries stretched to *in vivo* length (λ_z = 1.5) and fixed at 100 mmHg (normotensive). Arrows indicate one normalized thickness, which is from the IEL to the EEL. Bars = 50 μm.

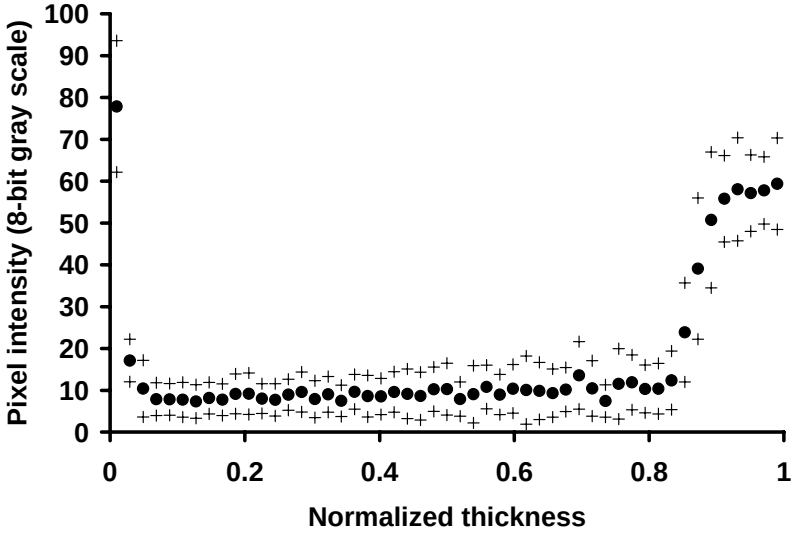

(A)

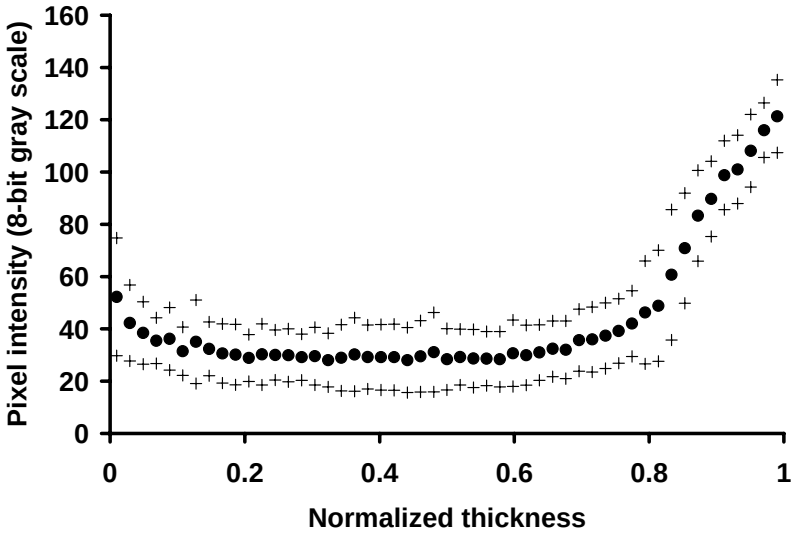

(B)

Figure 5.12: The average pixel intensities of elastin (n = 20) (A) and collagen fibers (n = 20) (B) in each layer were plotted against the normalized thickness as mean (•) ± S.D. (+) for sample #1001 (normotensive).

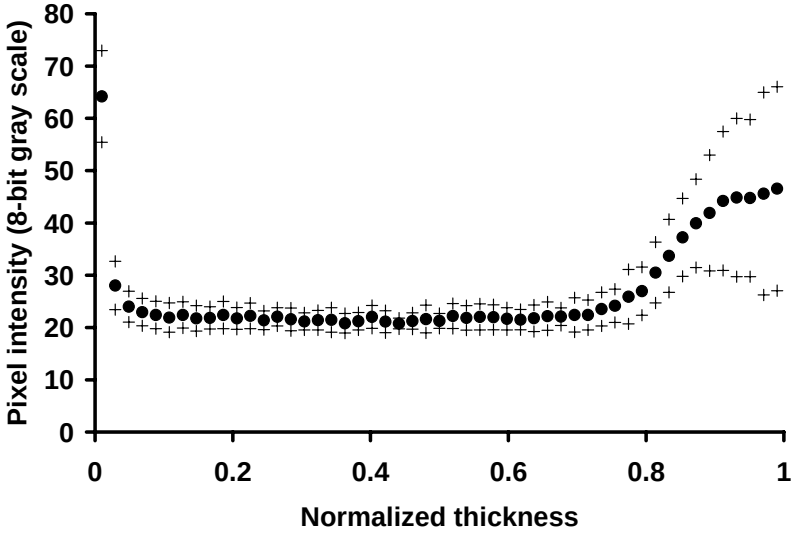

(A)

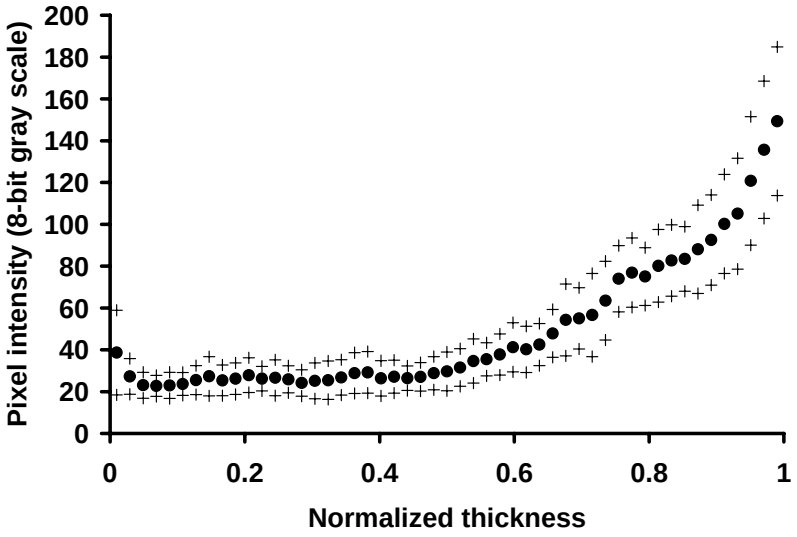

(B)

Figure 5.13: The average pixel intensities of elastin (n = 19) (A) and collagen fibers (n = 16) (B) in each layer were plotted against the normalized thickness as mean (•) ± S.D. (+) for sample #1002 (normotensive).

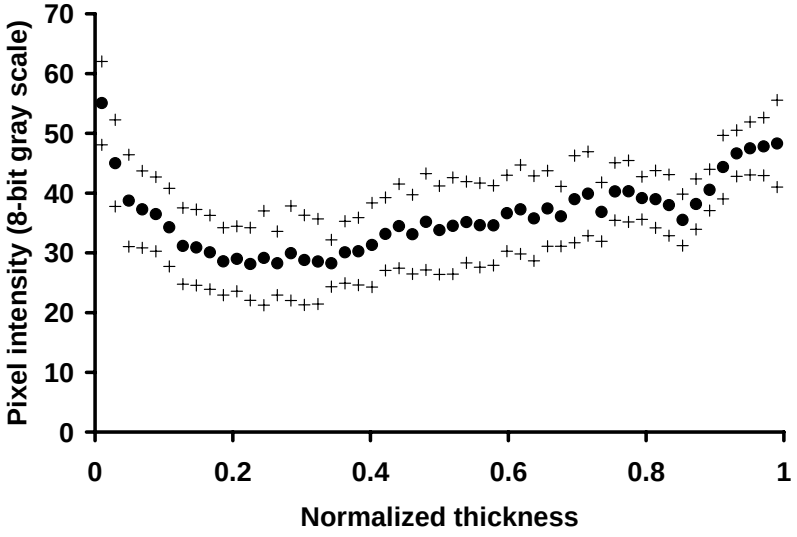

(A)

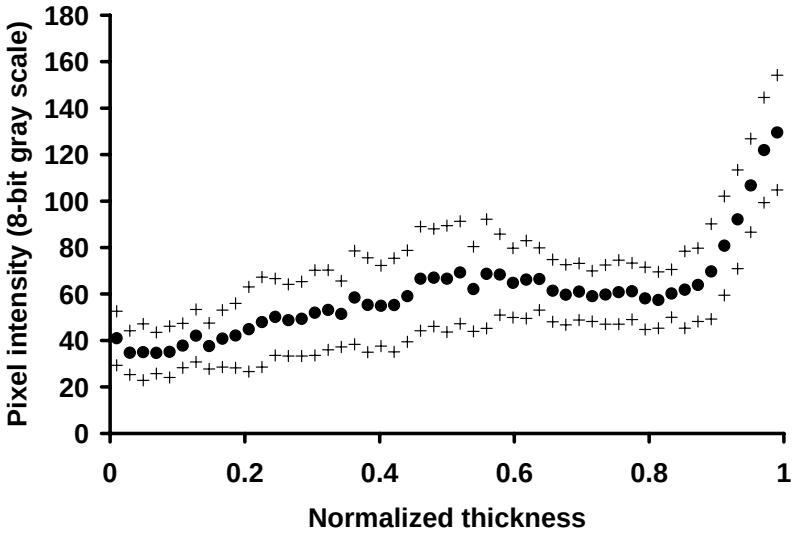

(B)

Figure 5.14: The average pixel intensities of elastin (n = 21) (A) and collagen fibers (n = 15) (B) in each layer were plotted against the normalized thickness as mean (•) ± S.D. (+) for sample #1003 (normotensive).

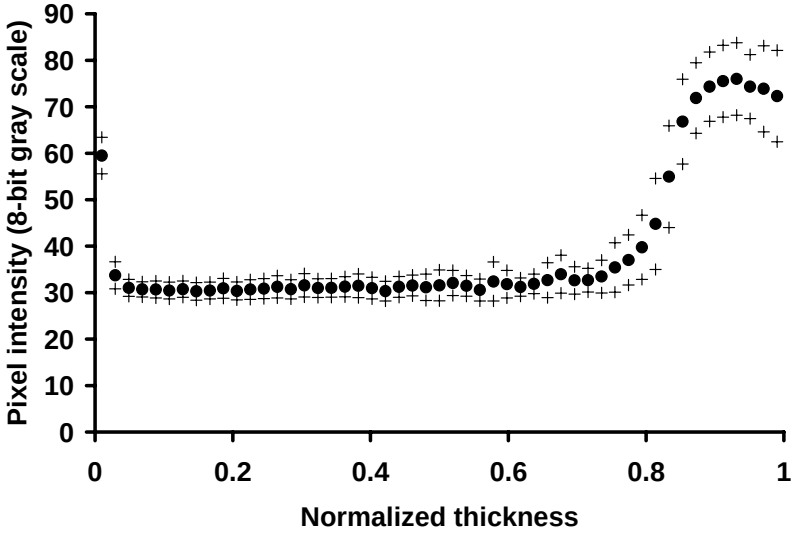

(A)

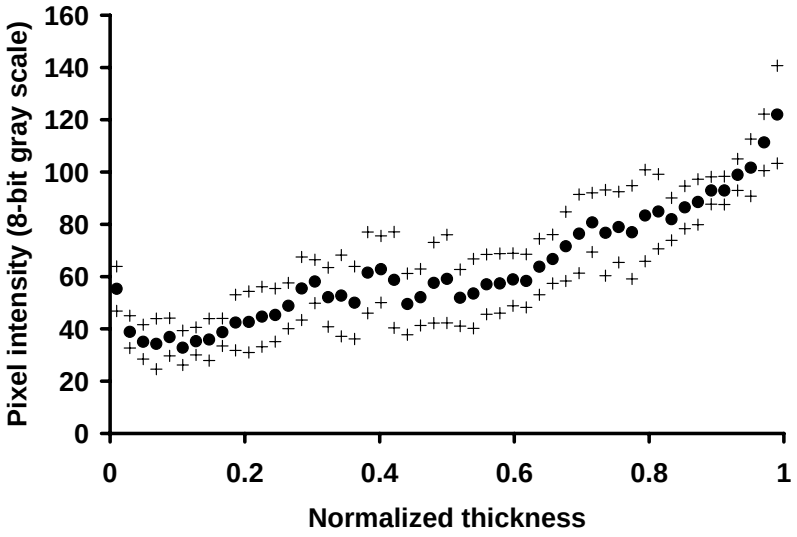

(B)

Figure 5.15: The average pixel intensities of elastin (n = 27) (A) and collagen fibers (n = 15) (B) in each layer were plotted against the normalized thickness as mean (•) ± S.D. (+) for sample #1004 (normotensive).

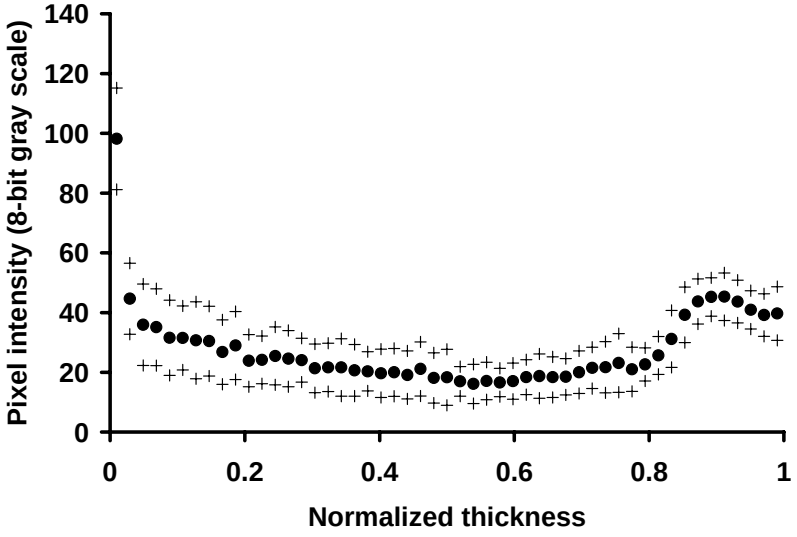

(A)

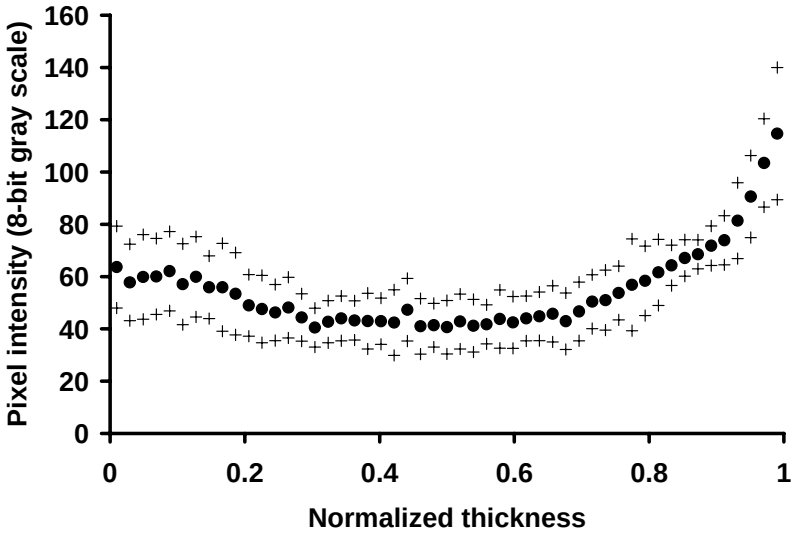

(B)

Figure 5.16: The average pixel intensities of elastin (n = 23) (A) and collagen fibers (n = 23) (B) in each layer were plotted against the normalized thickness as mean (•) ± S.D. (+) for sample #1005 (normotensive).

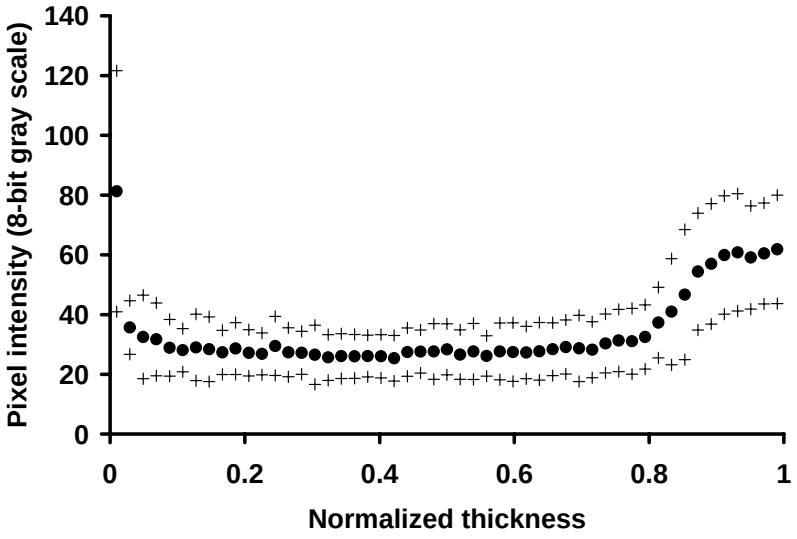

(A)

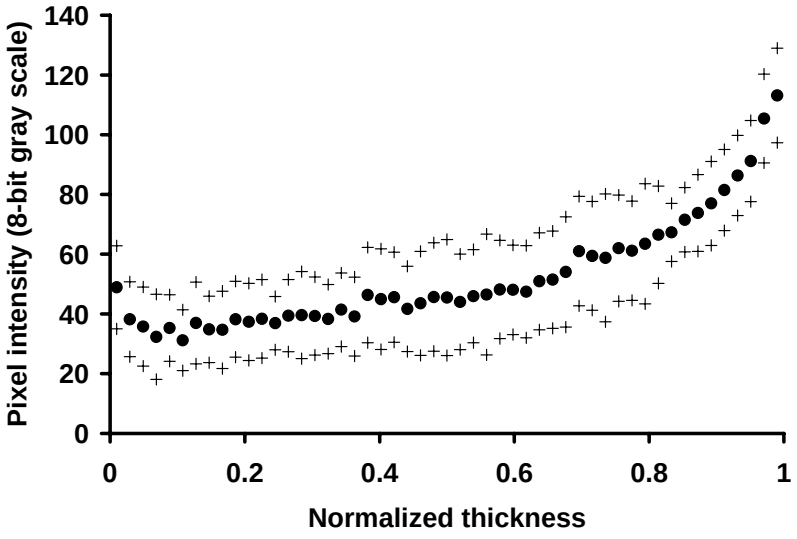

(B)

Figure 5.17: The average pixel intensities of elastin (n = 18) (A) and collagen fibers (n = 18) (B) in each layer were plotted against the normalized thickness as mean (•) ± S.D. (+) for sample #2001 (hypertensive).

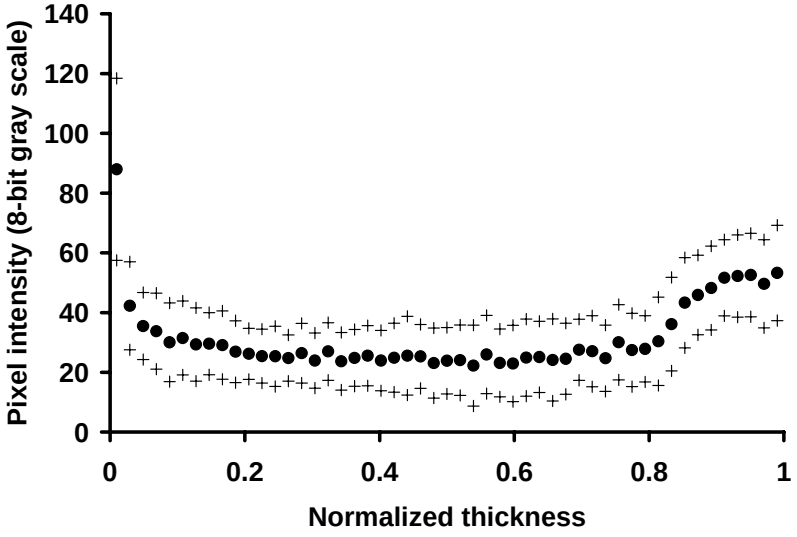

(A)

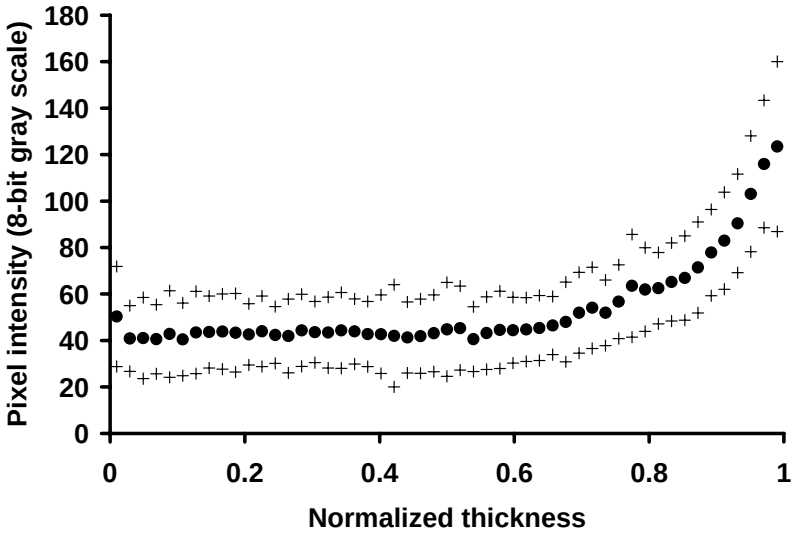

(B)

Figure 5.18: The average pixel intensities of elastin (n = 18) (A) and collagen fibers (n = 18) (B) in each layer were plotted against the normalized thickness as mean (•) ± S.D. (+) for sample #2002 (hypertensive).

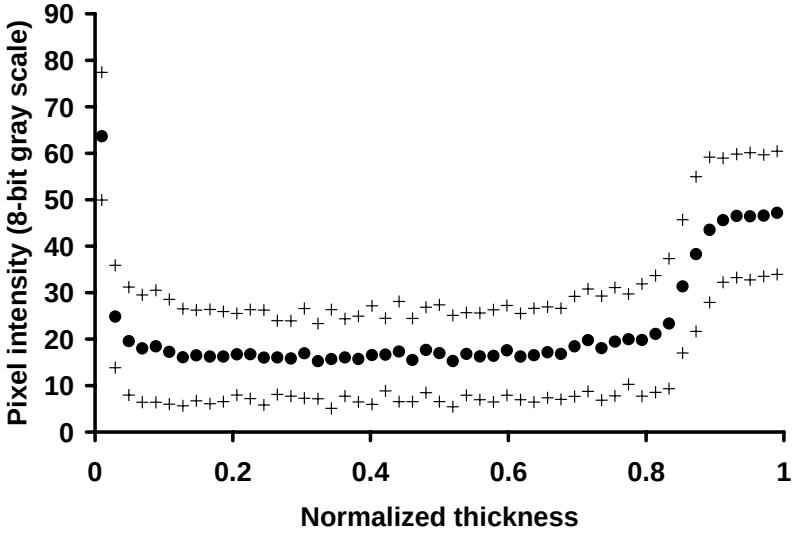

(A)

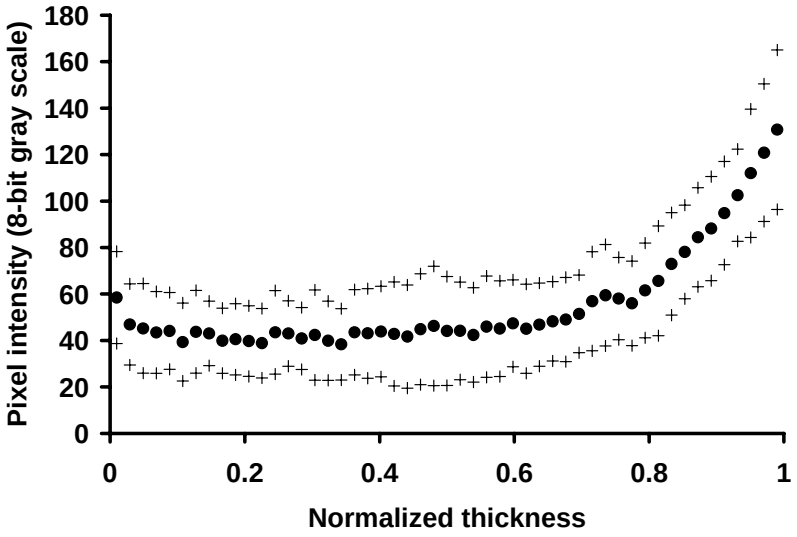

(B)

Figure 5.19: The average pixel intensities of elastin (n = 18) (A) and collagen fibers (n = 18) (B) in each layer were plotted against the normalized thickness as mean (•) ± S.D. (+) for sample #2003 (hypertensive).

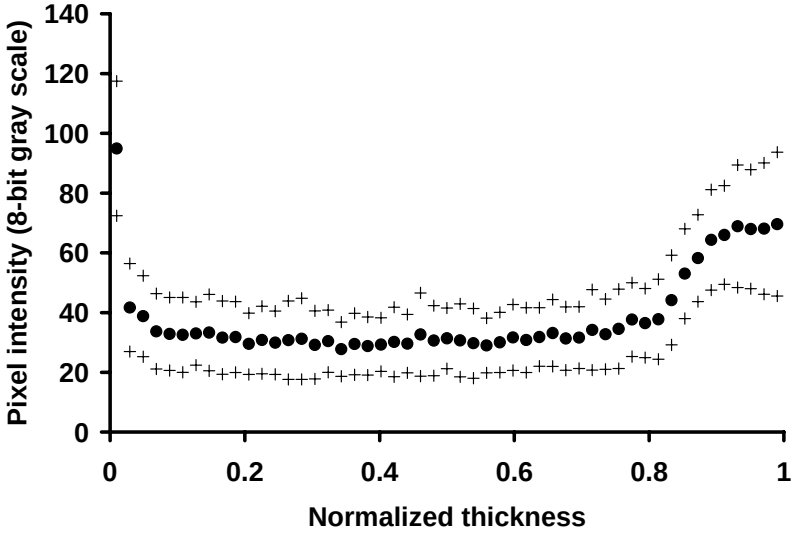

(A)

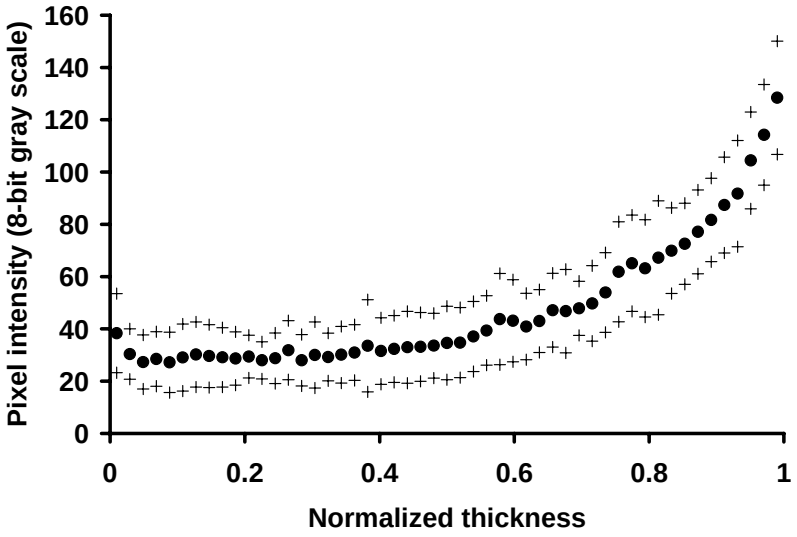

(B)

Figure 5.20: The average pixel intensities of elastin (n = 18) (A) and collagen fibers (n = 18) (B) in each layer were plotted against the normalized thickness as mean (•) ± S.D. (+) for sample #2004 (hypertensive).

Table 5.2: Spearman rank correlation coefficients (r_s) between normalized thickness and the concentrations of elastin and collagen fibers in normotensive arteries (#1001 – #1005) and hypertensive arteries (#2001 – #2004). All correlations were statistically significant except *two cases.

Specimen	Elastin concentration vs. normalized thickness (r_s)	Collagen fiber concentration vs. normalized thickness (r_s)
#1001	0.6149 ($p < 0.01$)	0.4720 ($p < 0.01$)
#1002	0.4414 ($p < 0.01$)	0.9109 ($p < 0.01$)
#1003	0.5828 ($p < 0.01$)	0.8480 ($p < 0.01$)
#1004	0.7778 ($p < 0.01$)	0.9371 ($p < 0.01$)
#1005	-0.0153 ($p = 0.46$)*	0.2687 ($p < 0.05$)
#2001	0.4240 ($p < 0.01$)	0.9378 ($p < 0.01$)
#2002	0.1859 ($p = 0.09$)*	0.8170 ($p < 0.01$)
#2003	0.5027 ($p < 0.01$)	0.7766 ($p < 0.01$)
#2004	0.4064 ($p < 0.01$)	0.9348 ($p < 0.01$)

Distributions of VSMC Nuclear Geometry

The length and orientation of VSMC nuclei were quantified using two pairs of common carotid arteries from young pigs. Each pair was composed of left and right common carotid arteries from same pig. In each pair, both arteries were stretched to *in vivo* length ($\lambda_z = 1.5$), and then one was fixed at 0 mmHg and the other at 100 mmHg.

VSMC Nuclear Length

The major axis lengths of VSMC nuclei at 0 mmHg were 18.02 ± 3.63 μm (n = 291) for pair 1 and 18.46 ± 3.96 μm (n = 372) for pair 2. The major axis lengths of VSMC nuclei at 100 mmHg were 23.09 ± 4.75 (n = 525) for pair 1 and 23.95 ± 5.03 (n = 485) for pair 2. The probability distribution of each data set of major axis lengths was not governed by a normal probability distribution (Table 5.3) and visualized using a histogram (Figure 5.21). In both pairs of data, the major axis length of VSMC nuclei was significantly shorter at 0 mmHg than at 100 mmHg ($p < 0.01$ for both pairs). The transmural distribution of major axis lengths showed a positive trend at 0 mmHg and no

significant trend at 100 mmHg (Table 5.4). However, major axis lengths at 0 mmHg peaked between 0.6 and 0.7 normalized thickness and decreased toward the outer boundary (Figure 5.22). The distributions of major axis lengths at 0 mmHg showed significant positive trends ($r_s = 0.30$, $p < 0.01$ for pair 1; $r_s = 0.24$, $p < 0.01$ for pair 2) in the inner 70% of the wall thickness and either no significant ($r_s = -0.14$, $p = 0.08$ for pair 1) or significant negative trend ($r_s = -0.21$, $p < 0.01$ for pair 2) in the outer 40% of the wall thickness. The major axis lengths of VSMC nuclei were uniformly distributed through the wall at 100 mmHg (Figure 5.22).

The circumferential lengths of VSMC nuclei at 0 mmHg were 16.72 ± 4.09 μm (n = 291) for pair 1 and 17.20 ± 4.26 μm (n = 372) for pair 2. The circumferential lengths of VSMC nuclei at 100 mmHg were 22.54 ± 4.97 (n = 525) for pair 1 and 23.41 ± 5.31 (n = 485) for pair 2. The probability distribution of each data set of circumferential lengths was not governed by a normal probability distribution (Table 5.3) and visualized using a histogram (Figure 5.23). In both pairs of data, the circumferential length of VSMC nuclei was significantly shorter at 0 mmHg than at 100 mmHg ($p < 0.01$ for both pairs). The transmural distribution of circumferential lengths showed a positive trend at 0 mmHg and no significant trend at 100 mmHg (Table 5.4). However, circumferential lengths at 0 mmHg peaked between 0.6 and 0.7 normalized thickness and decreased toward the outer boundary (Figure 5.24). The distributions of circumferential lengths at 0 mmHg showed significant positive trends ($r_s = 0.35$, $p < 0.01$ for pair 1; $r_s = 0.34$, $p < 0.01$ for pair 2) in the inner 70% of the wall thickness and either no significant ($r_s = -0.16$, $p = 0.05$ for pair 1) or significant negative trend ($r_s = -0.28$, $p < 0.01$ for pair 2) in the outer 40% of the wall thickness. The circumferential lengths of VSMC nuclei were uniformly distributed through the wall at 100 mmHg (Figure 5.24).

Based on the observation, the distribution of the circumferential lengths of VSMC nuclei at 100 mmHg was assumed to be uniform. The circumferential stretch ratios of VSMC nuclei at 0 mmHg with respect to the circumferential lengths of VSMC nuclei at

100 mmHg were higher than the stretch ratios of arterial tissue in the circumferential direction with respect to the configuration at 100 mmHg (Figure 5.25). Upon depressurization, the VSMC nuclei deformed about half of the deformation of arterial tissue at the same intramural location in the circumferential direction.

Table 5.3: The hypothesis that each data set for the measurements of VSMC nuclear geometry has a normal distribution was evaluated using the Lilliefors test. The hypothesis is rejected if the test is significant at the 5% level (i.e. a *p*-value is below 0.05). *Four data sets followed a normal distribution.

VSMC nuclear geometry	Specimen Pair 1		Specimen Pair 2	
	0 mmHg	100 mmHg	0 mmHg	100 mmHg
Major axis length	$p < 0.01$	$p = 0.0145$	$p < 0.01$	$p < 0.01$
Circumferential length	$p < 0.01$	$p = 0.0251$	$p < 0.01$	$p < 0.01$
Helical deviation	$p < 0.01$	$p < 0.01$	$p < 0.01$	$p < 0.01$
Helical angle	$p = 0.1819$*	$p < 0.01$	$p = 0.0151$	$p < 0.01$
Radial deviation	$p < 0.01$	$p < 0.01$	$p < 0.01$	$p < 0.01$
Radial angle	$p = 0.0953$*	$p = 0.1908$*	$p < 0.01$	$p = 0.1491$*

Table 5.4: Spearman rank correlation coefficients (r_s) between normalized thickness and the major axis lengths, circumferential lengths, helical and radial deviation, and helical and radial angles.

	Specimen Pair 1		Specimen Pair 2	
	0 mmHg	100 mmHg	0 mmHg	100 mmHg
Major axis length vs. normalized thickness (r_s)	0.2195 ($p < 0.01$)	-0.0262 ($p = 0.27$)	0.1382 ($p < 0.01$)	-0.0722 ($p = 0.06$)
Circumferential length vs. normalized thickness (r_s)	0.2102 ($p < 0.01$)	-0.0270 ($p = 0.27$)	0.1674 ($p < 0.01$)	-0.0667 ($p = 0.07$)
Helical deviation vs. normalized thickness (r_s)	-0.0182 ($p = 0.38$)	0.0050 ($p = 0.45$)	-0.0216 ($p = 0.34$)	-0.0091 ($p = 0.42$)
Helical angle vs. normalized thickness (r_s)	0.0020 ($p = 0.49$)	-0.0867 ($p = 0.02$)	0.0725 ($p = 0.08$)	-0.0136 ($p = 0.38$)
Radial deviation vs. normalized thickness (r_s)	0.0205 ($p = 0.36$)	-0.0120 ($p = 0.39$)	-0.1113 ($p = 0.02$)	0.0153 ($p = 0.37$)
Radial angle vs. normalized thickness (r_s)	-0.0386 ($p = 0.26$)	-0.0094 ($p = 0.41$)	-0.0542 ($p = 0.15$)	-0.0588 ($p = 0.10$)

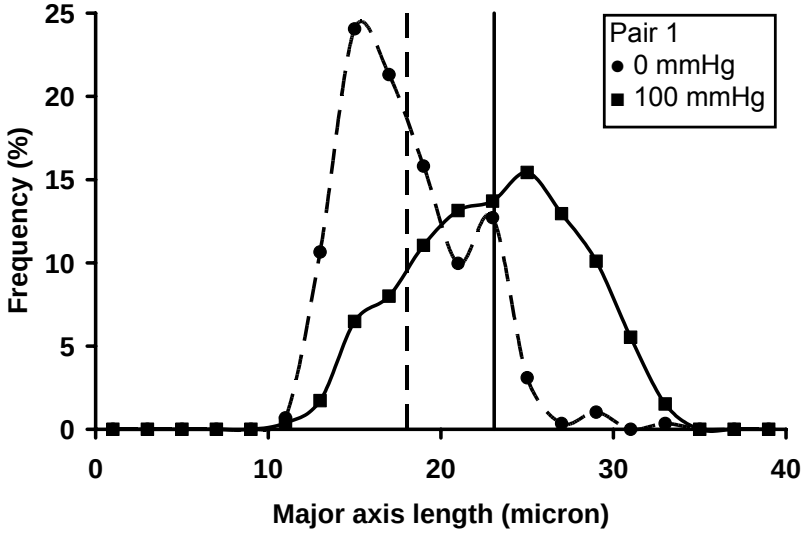

(A)

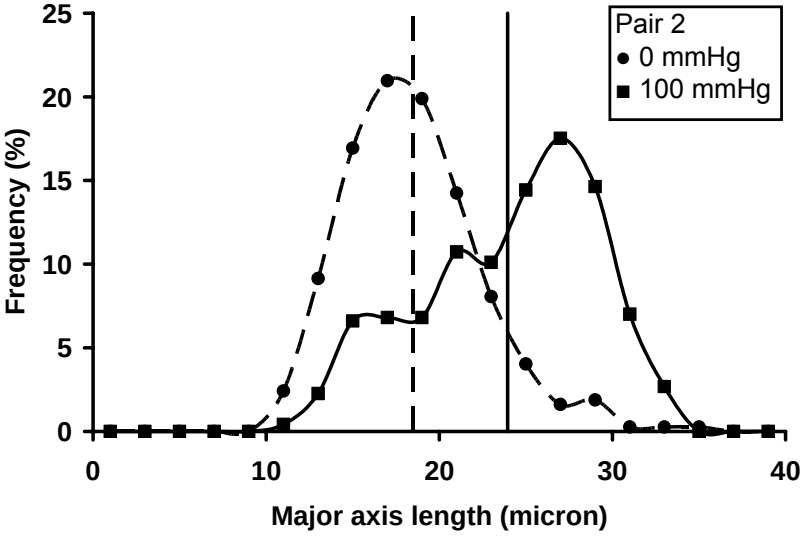

(B)

Figure 5.21: Histograms of VSMC nuclear major axis lengths at 0 mmHg (●) and 100 mmHg (■) in pair 1 (A) and pair 2 (B) were shown. The numbers of VSMC nuclei were counted in 20 evenly distributed bins between 0 μm and 40 μm. The means of the major axis lengths of VSMC nuclei at 0 mmHg (dashed line) and 100 mmHg (solid line) were also plotted.

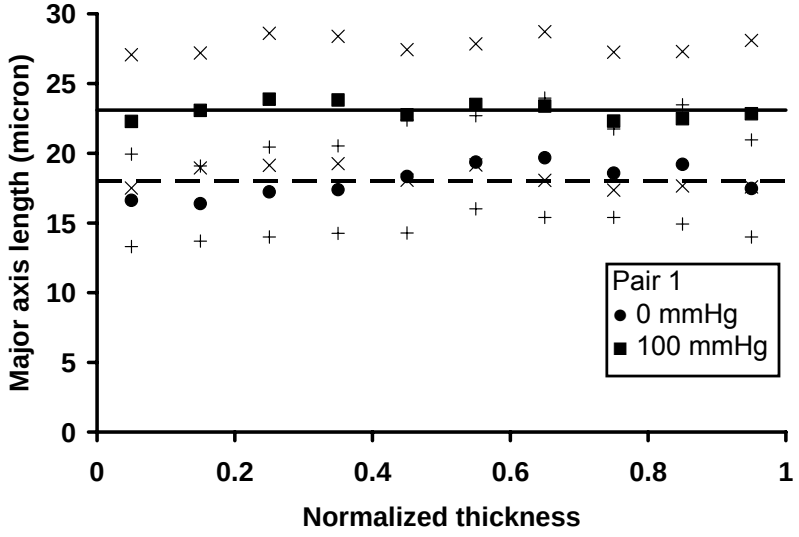

(A)

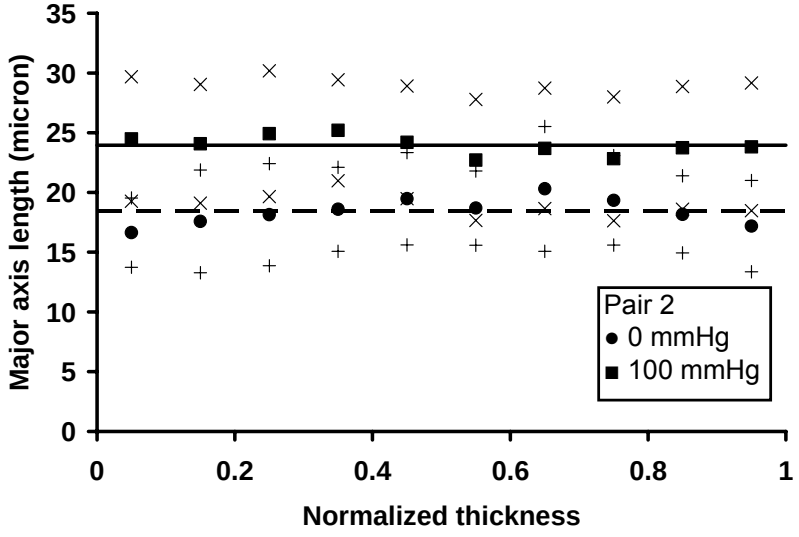

(B)

Figure 5.22: The transmural distributions of major axis lengths in pair 1 (A) and pair 2 (B) were shown as the mean (● for 0 mmHg; ■ for 100 mmHg) ± S.D. (+ for 0 mmHg; × for 100 mmHg) of local measurements in 10 bins between 0 and 1 normalized thickness. The means of the major axis lengths of VSMC nuclei at 0 mmHg (dashed line) and 100 mmHg (solid line) were also plotted.

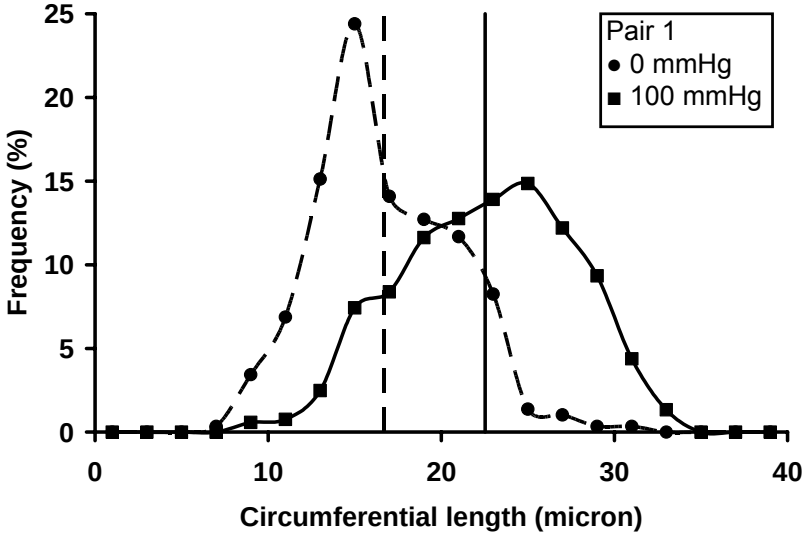

(A)

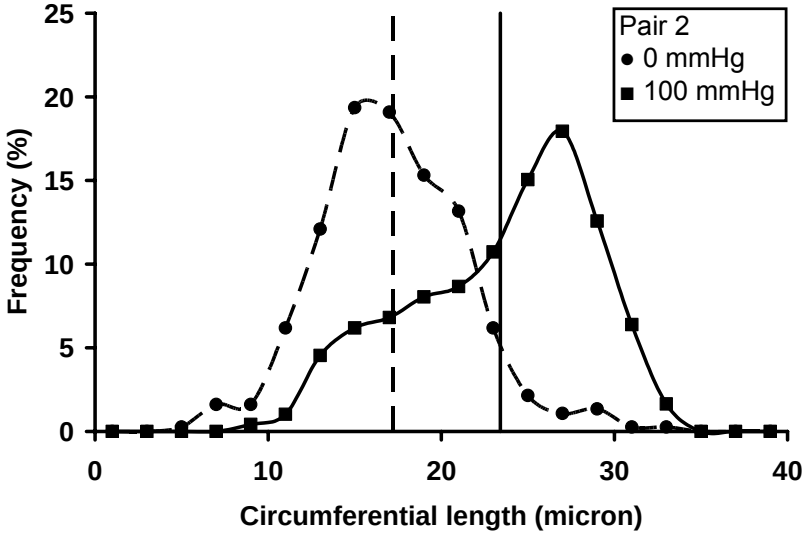

(B)

Figure 5.23: Histograms of the circumferential lengths of VSMC nuclei at 0 mmHg (●) and 100 mmHg (■) in pair 1 (A) and pair 2 (B) were shown. The numbers of VSMC nuclei were counted in 20 evenly distributed bins between 0 μm and 40 μm. The means of the circumferential lengths of VSMC nuclei at 0 mmHg (dashed line) and 100 mmHg (solid line) were also plotted.

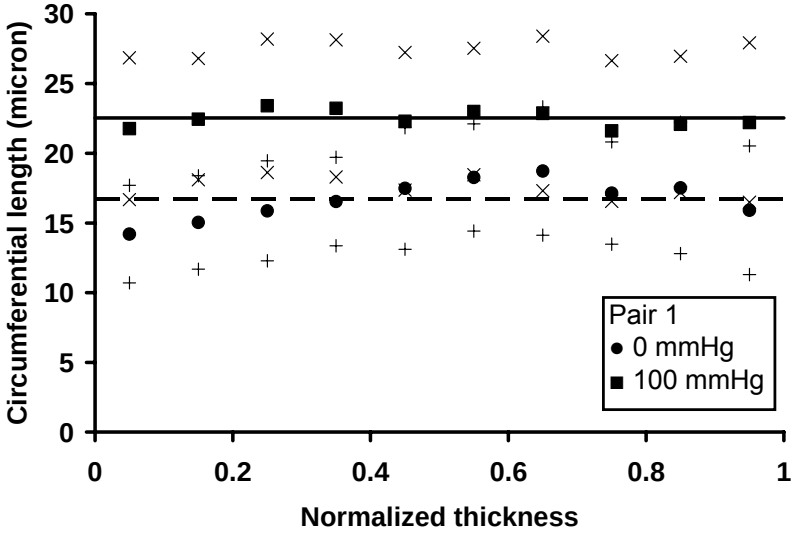

(A)

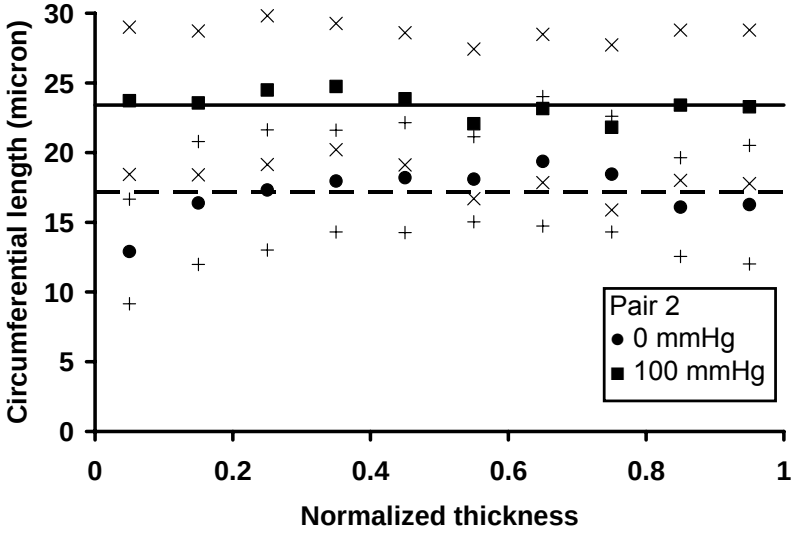

(B)

Figure 5.24: The transmural distributions of circumferential lengths in pair 1 (A) and pair 2 (B) were shown as the mean (● for 0 mmHg; ■ for 100 mmHg) ± S.D. (+ for 0 mmHg; × for 100 mmHg) of local measurements in 10 bins between 0 and 1 normalized thickness. The means of the circumferential lengths of VSMC nuclei at 0 mmHg (dashed line) and 100 mmHg (solid line) were also plotted.

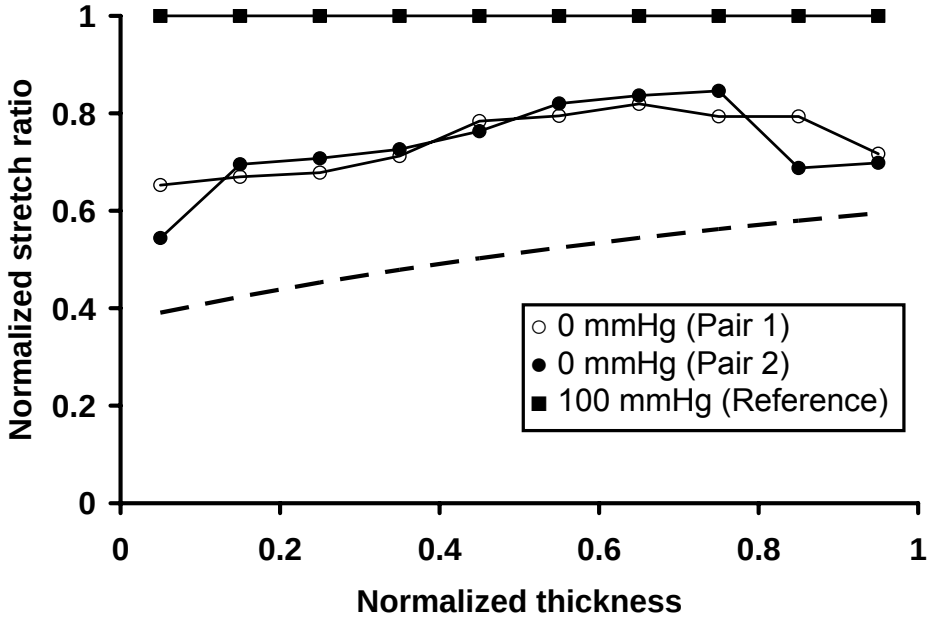

Figure 5.25: The distributions of the normalized circumferential stretch ratios of VSMC nuclei at 100 mmHg (■) and 0 mmHg (○ for pair 1; ● for pair 2) with respect to the circumferential length of VSMC nuclei at 100 mmHg. For comparison, the normalized circumferential stretch ratio of arterial tissue at 0 mmHg computed from available pressure-diameter experiments (Davis, 2002; n = 9) with respect to the configuration of arterial tissue at 100 mmHg was plotted (dashed line).

VSMC Nuclear Orientation

The helical angles of VSMC nuclei at 0 mmHg were 5.14 ± 19.41° (n = 291) for pair 1 and -0.71 ± 20.24° (n = 372) for pair 2. The helical angles of VSMC nuclei at 100 mmHg were 2.61 ± 11.57° (n = 525) for pair 1 and -2.50 ± 11.21° (n = 485) for pair 2. The probability distribution of each data set of helical angles was not governed by a normal probability distribution except the helical angles of pair 1 at 0 mmHg (Table 5.3) and visualized using a histogram (Figure 5.26). In pair 1, the helical angle of VSMC nuclei was significantly larger at 0 mmHg than at 100 mmHg (p = 0.04). The difference between the average helical angles in pair 1 was small (2.53°) and may caused by error

due to the alignment. In pair 2, there was no significant difference between the average helical angles of VSMC nuclei at 0 mmHg and at 100 mmHg ($p = 0.32$). The transmural distribution of helical angles showed no trend (Table 5.4) and was uniform either at 0 mmHg or at 100 mmHg (Figure 5.27). Although both of average helical angles at 0 mmHg and 100 mmHg were close to zero, the standard deviation of helical angles was larger at 0 mmHg than at 100 mmHg.

The helical deviations of VSMC nuclei at 0 mmHg were 15.27 ± 13.01° (n = 291) for pair 1 and 14.89 ± 13.41° (n = 372) for pair 2. The helical deviations of VSMC nuclei at 100 mmHg were 8.79 ± 7.95° (n = 525) for pair 1 and 8.04 ± 8.20° (n = 485) for pair 2. The probability distribution of each data set of helical deviations was not governed by a normal probability distribution (Table 5.3) and visualized using a histogram (Figure 5.28). In both pairs of data, the helical deviation of VSMC nuclei was significantly larger at 0 mmHg than at 100 mmHg ($p < 0.01$ for both pairs). The transmural distribution of helical deviations showed no significant trend either at 0 mmHg or at 100 mmHg (Table 5.4). However, helical deviations at 0 mmHg were small in the middle of an arterial wall and increased toward the inner and the outer boundaries (Figure 5.29). The distributions of helical deviations at 0 mmHg showed significant negative trends ($r_s = -0.22$, $p < 0.01$ for pair 1; $r_s = -0.18$, $p < 0.01$ for pair 2) in the inner half of the wall thickness and significant positive trends ($r_s = 0.17$, $p = 0.03$ for pair 1; $r_s = 0.16$, $p = 0.02$ for pair 2) in the outer half of the wall thickness. The helical deviations of VSMC nuclei were uniformly distributed through the arterial wall at 100 mmHg (Figure 5.29).

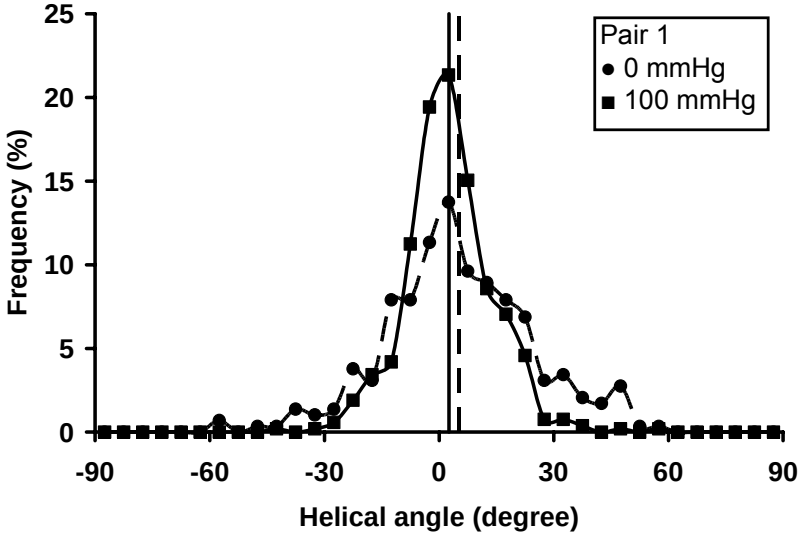

(A)

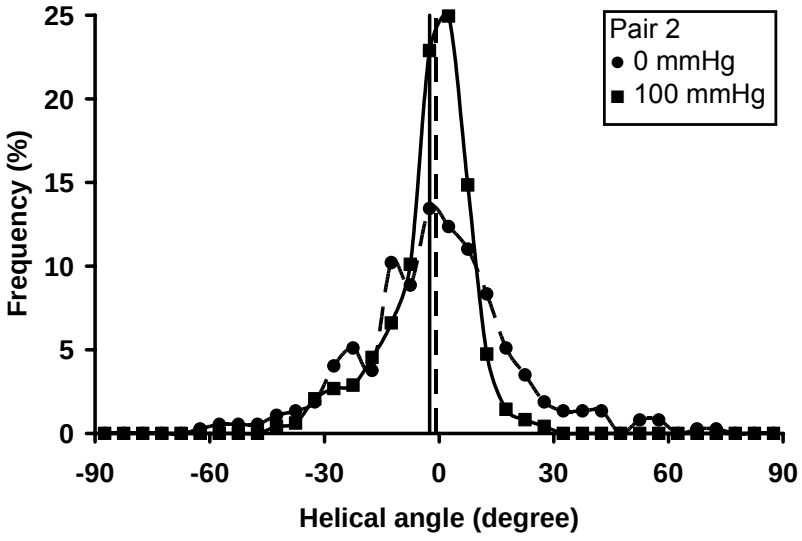

(B)

Figure 5.26: Histograms of the helical angles of VSMC nuclei at 0 mmHg (●) and 100 mmHg (■) in pair 1 (A) and pair 2 (B) were shown. The numbers of VSMC nuclei were counted in 36 evenly distributed bins between -90° and 90°. The means of the helical angles of VSMC nuclei at 0 mmHg (dashed line) and 100 mmHg (solid line) were also plotted.

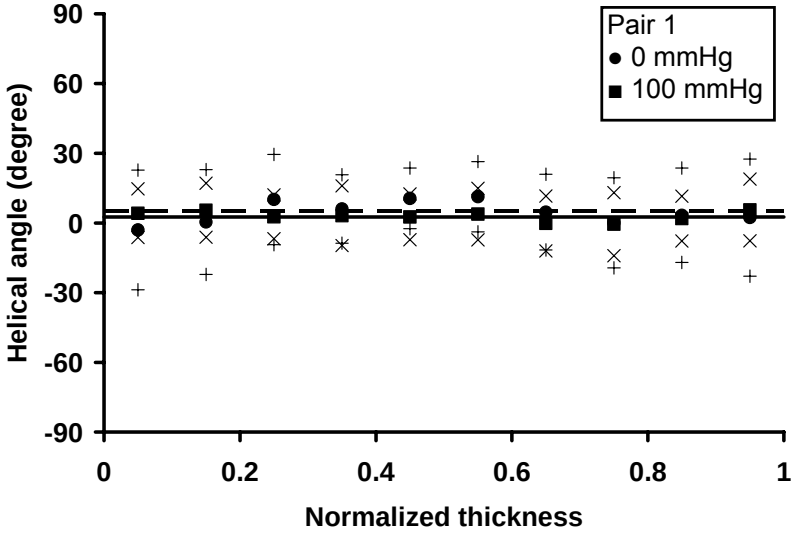

(A)

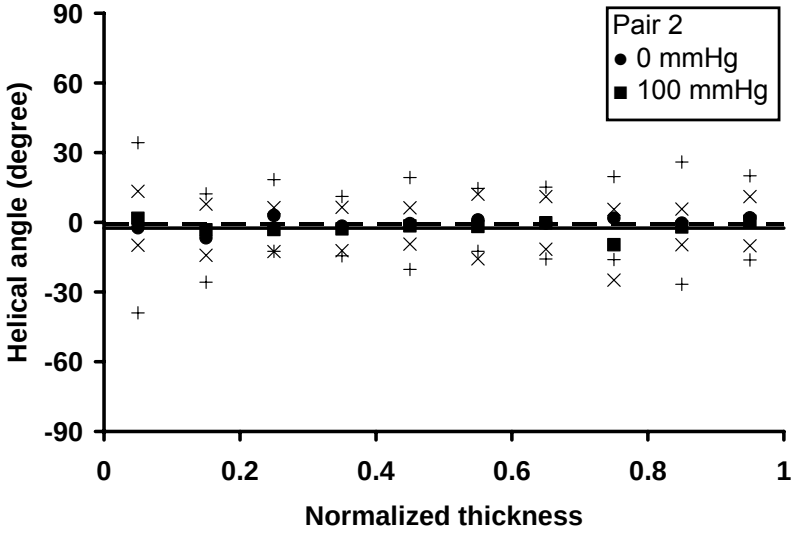

(B)

Figure 5.27: The transmural distributions of helical angles in pair 1 (A) and pair 2 (B) were shown as the mean (● for 0 mmHg; ■ for 100 mmHg) ± S.D. (+ for 0 mmHg; × for 100 mmHg) of local measurements in 10 bins between 0 and 1 normalized thickness. The means of the helical angles of VSMC nuclei at 0 mmHg (dashed line) and 100 mmHg (solid line) were also plotted.

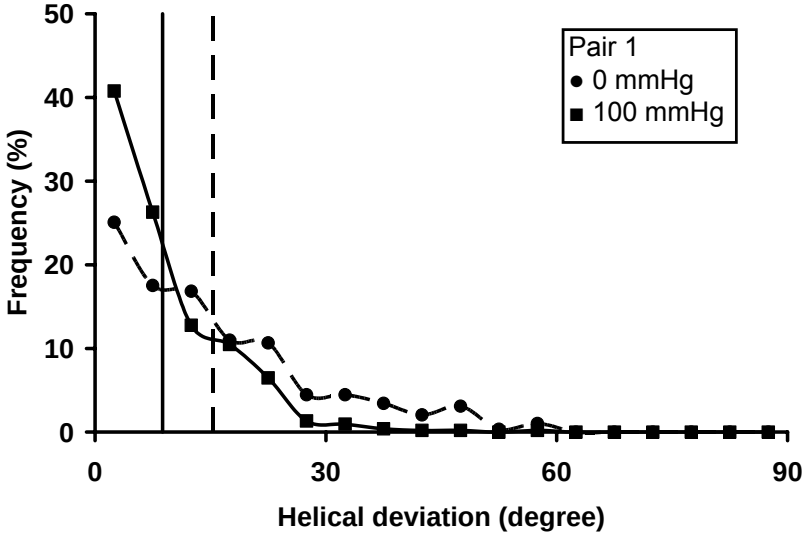

(A)

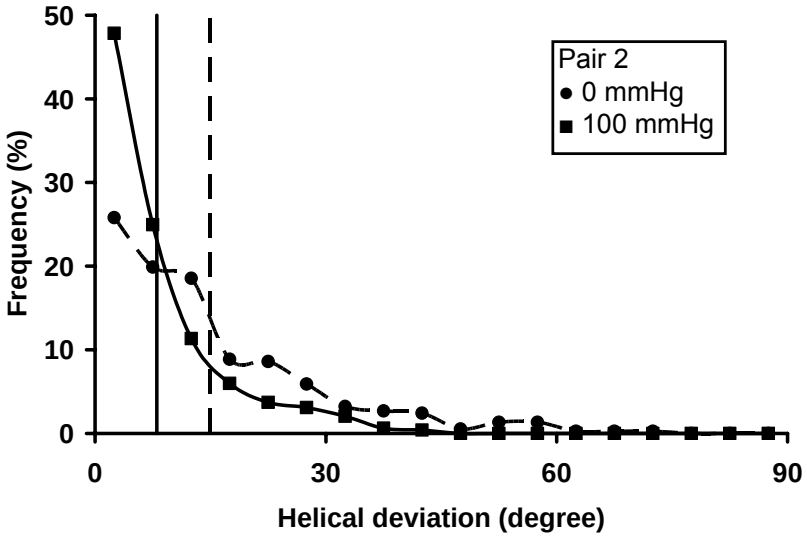

(B)

Figure 5.28: Histograms of the helical deviations of VSMC nuclei at 0 mmHg (●) and 100 mmHg (■) in pair 1 (A) and pair 2 (B) were shown. The numbers of VSMC nuclei were counted in 18 evenly distributed bins between 0° and 90°. The means of the helical deviations of VSMC nuclei at 0 mmHg (dashed line) and 100 mmHg (solid line) were also plotted.

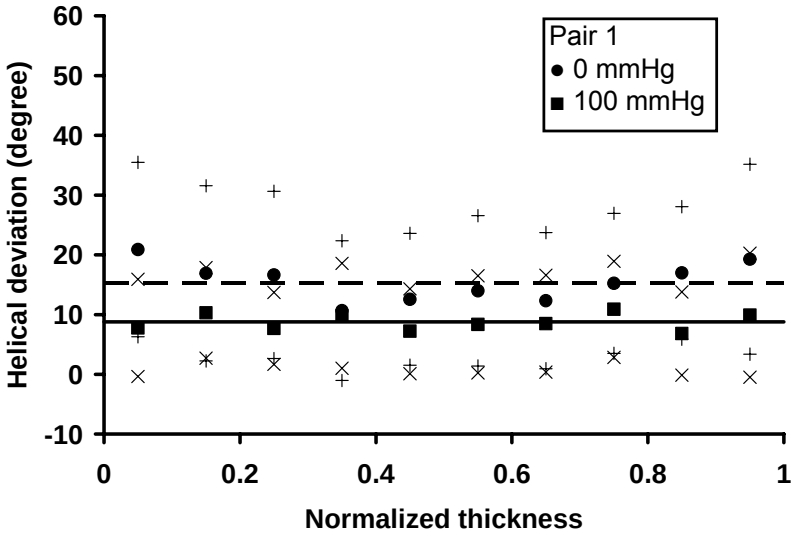

(A)

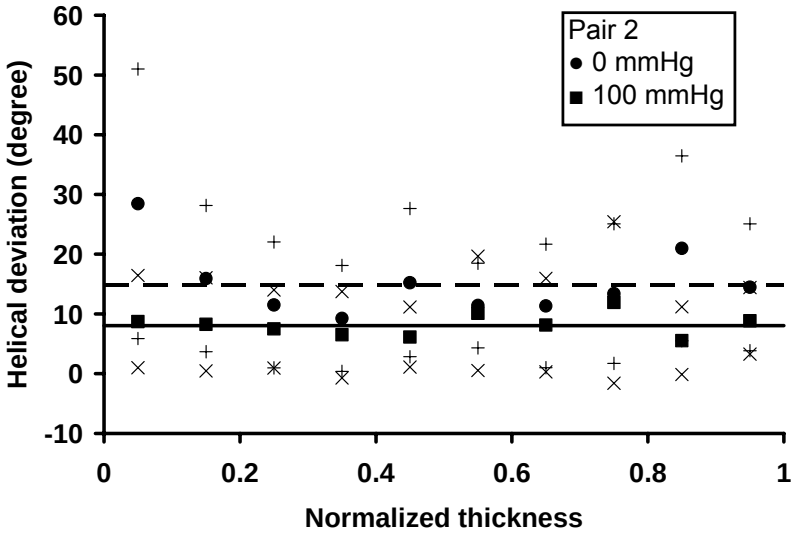

(B)

Figure 5.29: The transmural distributions of helical deviations in pair 1 (A) and pair 2 (B) were shown as the mean (● for 0 mmHg; ■ for 100 mmHg) ± S.D. (+ for 0 mmHg; × for 100 mmHg) of local measurements in 10 bins between 0 and 1 normalized thickness. The means of the helical deviations of VSMC nuclei at 0 mmHg (dashed line) and 100 mmHg (solid line) were also plotted.

The radial angles of VSMC nuclei at 0 mmHg were -0.10 ± 11.78° (n = 291) for pair 1 and 0.76 ± 10.10° (n = 372) for pair 2. The radial angles of VSMC nuclei at 100 mmHg were 0.27 ± 6.36° (n = 525) for pair 1 and 0.36 ± 6.94° (n = 485) for pair 2. The probability distribution of each data set of radial angles was generally governed by a normal probability distribution except the radial angles of pair 2 at 0 mmHg (Table 5.3) and visualized using a histogram (Figure 5.30). There was no significant difference between the average radial angles of VSMC nuclei at 0 mmHg and at 100 mmHg (p = 0.63 for pair 1; p = 0.83 for pair 2). The transmural distribution of radial angles showed no significant trend (Table 5.4) and was uniform either at 0 mmHg or at 100 mmHg (Figure 5.31). Although both of average radial angles at 0 mmHg and 100 mmHg were close to zero, the standard deviation of radial angles was larger at 0 mmHg than at 100 mmHg.

The radial deviations of VSMC nuclei at 0 mmHg were 8.89 ± 7.71° (n = 291) for pair 1 and 7.25 ± 7.07° (n = 372) for pair 2. The radial deviations of VSMC at 100 mmHg were 4.85 ± 4.11° (n = 525) for pair 1 and 5.36 ± 4.43° (n = 485) for pair 2. The probability distribution of each data set of radial deviations was not governed by a normal probability distribution (Table 5.3) and visualized using a histogram (Figure 5.32). In both pairs of data, the radial deviation of VSMC nuclei was significantly larger at 0 mmHg than at 100 mmHg ($p < 0.01$ for both pairs). The transmural distribution of radial deviations at 0 mmHg showed no significant trend for pair 1 and a significant but weak negative trend for pair 2. There was no significant trend in the transmural distribution of radial deviations at 100 mmHg (Table 5.4). However, radial deviations at 0 mmHg were smallest between 0.6 and 0.7 normalized thickness and increased toward the inner and the outer boundaries (Figure 5.33). The distributions of radial deviations at 0 mmHg showed significant negative trends (r_s = -0.14, p = 0.02 for pair 1; r_s = -0.25, $p < 0.01$ for pair 2) in the inner 70% of the wall thickness and significant positive trends (r_s = 0.18, p = 0.04

for pair 1; $r_s = 0.25$, $p < 0.01$ for pair 2) in the outer 40% of the wall thickness. The radial deviations of VSMC nuclei were uniformly distributed through the arterial wall at 100 mmHg (Figure 5.33).

Distributions of Circumferential Stresses

The average opening angle and helical deviation, 41.87° and 8.43°, respectively, were used in the heterogeneous and homogeneous models. The opening angle of porcine common carotid arteries was 41.87 ± 21.22° (n = 13) and ranged from 0.64° to 75.21°. For each artery, the average area fractions of elastin and collagen fibers in each layer were used in the model.

Table 5.5 shows estimated parameters for the heterogeneous and homogeneous model. Since λ_{RP} is a function of r in the heterogeneous model, it is shown as the range of stretch ratio in the direction of the collagen fibers. Assuming a uniform strain of collagen fibers at physiological pressure (100 mmHg) and axial stretch ($\lambda_z = 1.5$), a recruiting point was highest at the inner surface (Figure 5.34).

In both normotensive and hypertensive arteries, the intramural distribution of circumferential stresses computed using the heterogeneous model was skewed "U"-shaped with the highest stress at the outer boundary (Figure 5.35 – 5.43). The gradient of circumferential stress was the highest near the intima. The circumferential stress decreased sharply at the boundary between the IEL and the media, and gradually increased toward the outer layer. The circumferential stress was lowest and generally uniform in the inner media.

The circumferential stress, computed using the homogeneous model, was highest at the intimal layer and gradually decreased toward the outer layer (Figure 5.44). The intramural distributions of circumferential stresses computed using the heterogeneous model were more uniform compared to the one computed using the homogeneous model (Figure 5.45).

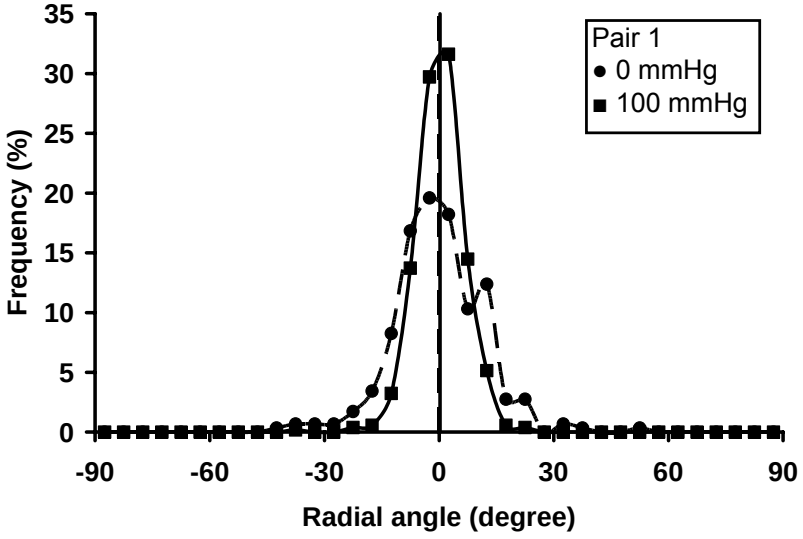

(A)

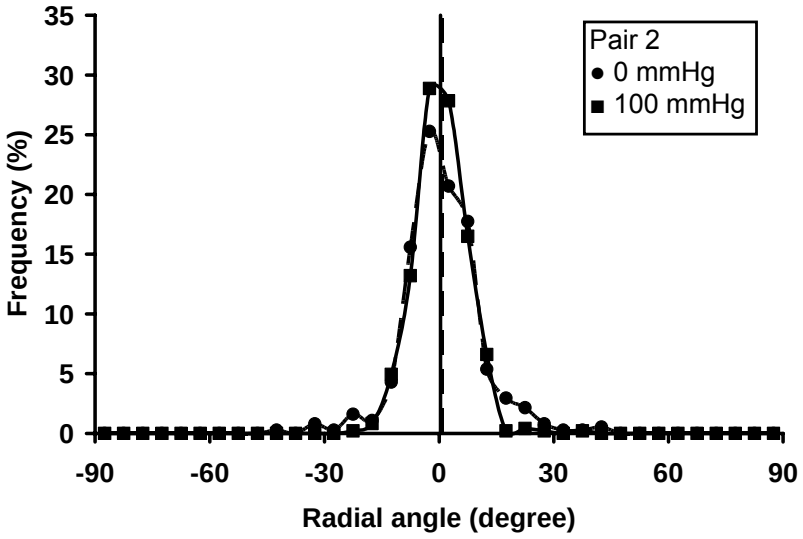

(B)

Figure 5.30: Histograms of the radial angles of VSMC nuclei at 0 mmHg (●) and 100 mmHg (■) in pair 1 (A) and pair 2 (B) were shown. The numbers of VSMC nuclei were counted in 36 evenly distributed bins between -90° and 90°. The means of the radial angles of VSMC nuclei at 0 mmHg (dashed line) and 100 mmHg (solid line) were also plotted.

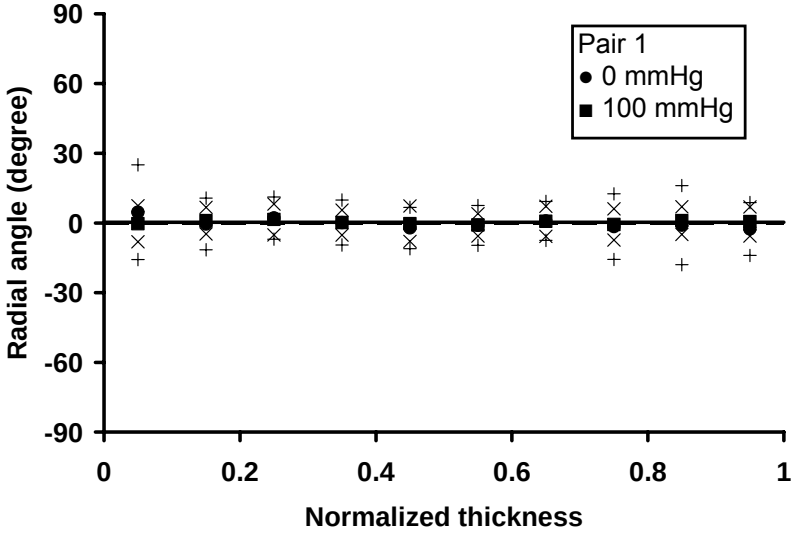

(A)

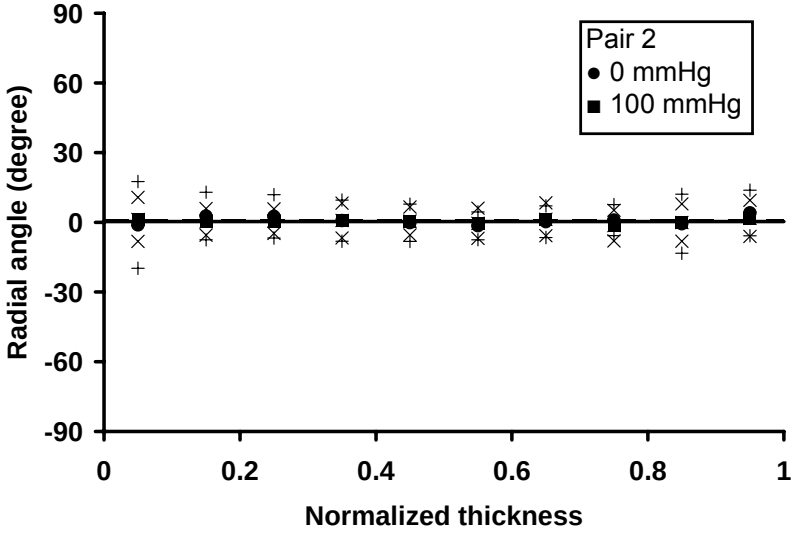

(B)

Figure 5.31: The transmural distributions of radial angles in pair 1 (A) and pair 2 (B) were shown as the mean (● for 0 mmHg; ■ for 100 mmHg) ± S.D. (+ for 0 mmHg; × for 100 mmHg) of local measurements in 10 bins between 0 and 1 normalized thickness. The means of the radial angles of VSMC nuclei at 0 mmHg (dashed line) and 100 mmHg (solid line) were also plotted.

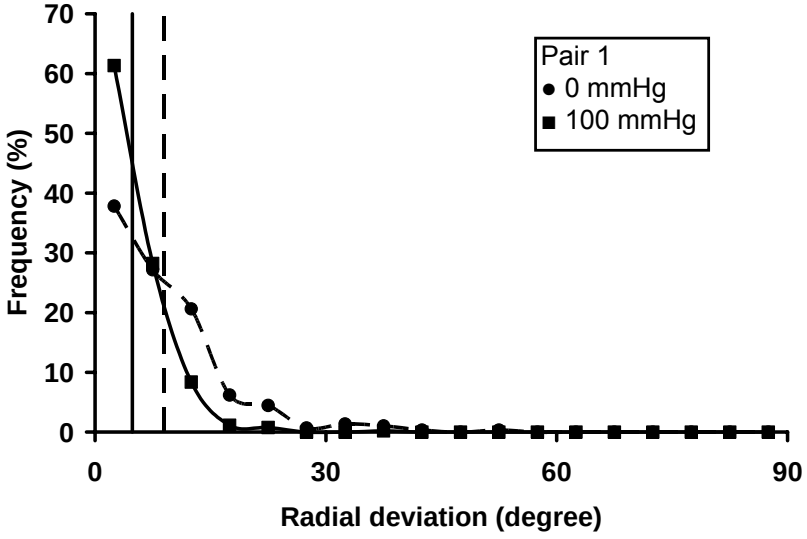

(A)

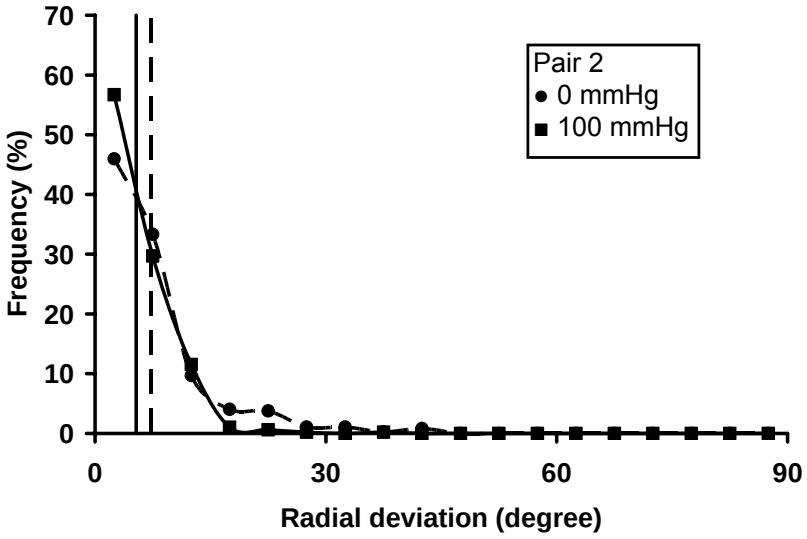

(B)

Figure 5.32: Histograms of the radial deviations of VSMC nuclei at 0 mmHg (●) and 100 mmHg (■) in pair 1 (A) and pair 2 (B) were shown. The numbers of VSMC nuclei were counted in 18 evenly distributed bins between 0° and 90°. The means of the radial deviations of VSMC nuclei at 0 mmHg (dashed line) and 100 mmHg (solid line) were also plotted.

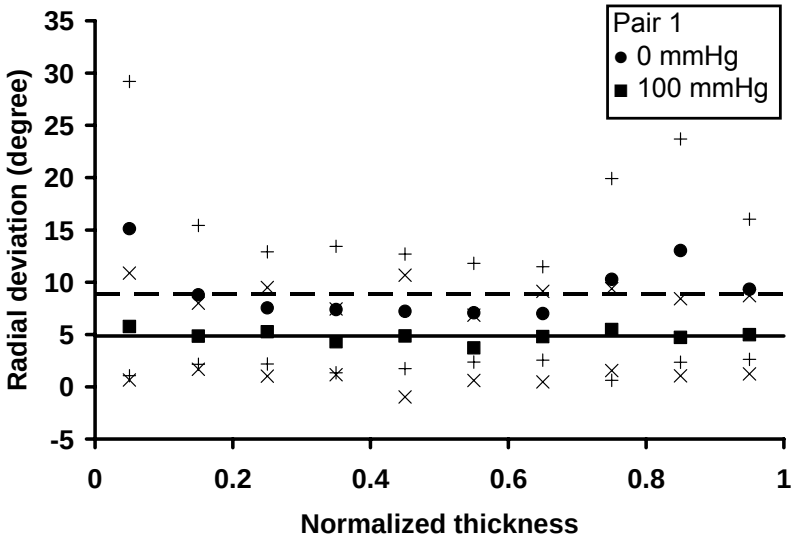

(A)

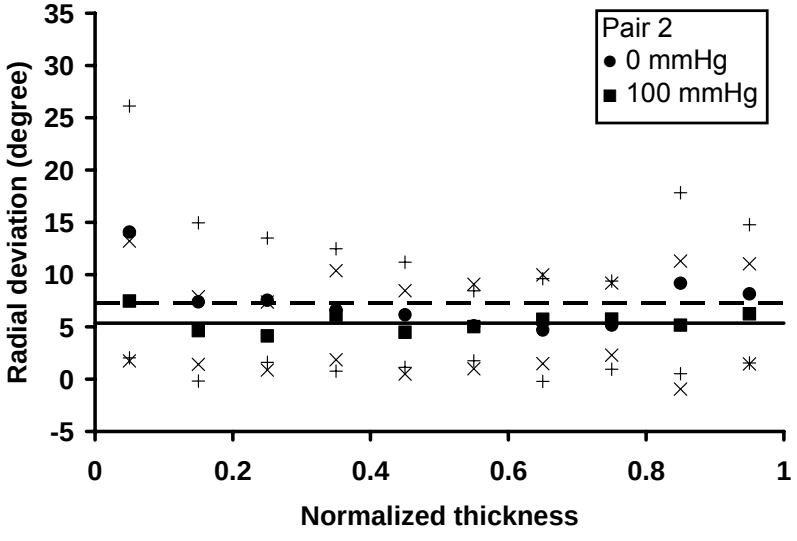

(B)

Figure 5.33: The transmural distributions of radial deviations in pair 1 (A) and pair 2 (B) were shown as the mean (● for 0 mmHg; ■ for 100 mmHg) ± S.D. (+ for 0 mmHg; × for 100 mmHg) of local measurements in 10 bins between 0 and 1 normalized thickness. The means of the radial deviations of VSMC nuclei at 0 mmHg (dashed line) and 100 mmHg (solid line) were also plotted.

Table 5.5: Material constants for elastin and collagen fibers, the range of recruiting points for the heterogeneous model, and the recruiting point for the homogeneous model estimated by minimizing the error function (Ω) are shown for normotensive arteries (#1001 – #1005) and hypertensive arteries (#2001 – #2004).

	c'_e	c'_{c1}	c_{c2}	λ_{RP}	R^2
#1001	4.28	6.04	3.74	1.00 – 1.49	0.9949
#1002	3.92	6.02	3.80	1.00 – 1.49	0.9949
#1003	3.97	6.04	3.72	1.00 – 1.49	0.9949
#1004	4.18	6.03	3.74	1.00 – 1.49	0.9948
#1005	3.74	6.11	3.67	1.00 – 1.49	0.9949
#2001	4.01	6.05	3.73	1.00 – 1.49	0.9949
#2002	3.88	6.06	3.71	1.00 – 1.49	0.9949
#2003	4.06	6.05	3.72	1.00 – 1.49	0.9949
#2004	3.95	6.03	3.76	1.00 – 1.49	0.9949
Homogeneous	3.25	2.57	0.78	1.04	0.9960

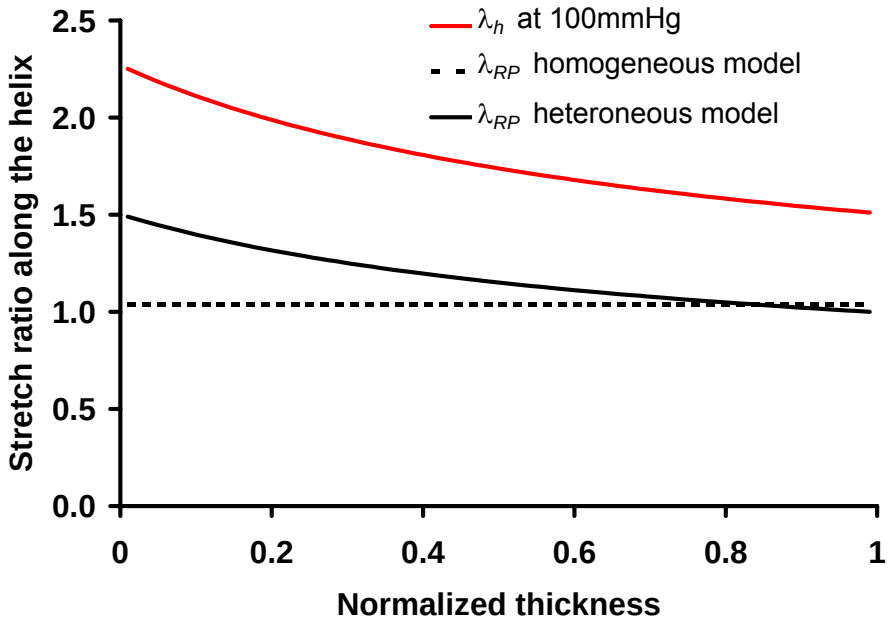

Figure 5.34: The distribution of recruiting points in the heterogeneous model (black solid line) is plotted along with the stretch ratio of the artery along the helix at 100 mmHg and $\lambda_z = 1.5$ (red solid line) and the recruiting point in the homogeneous model (dotted line), which is a constant through the thickness.

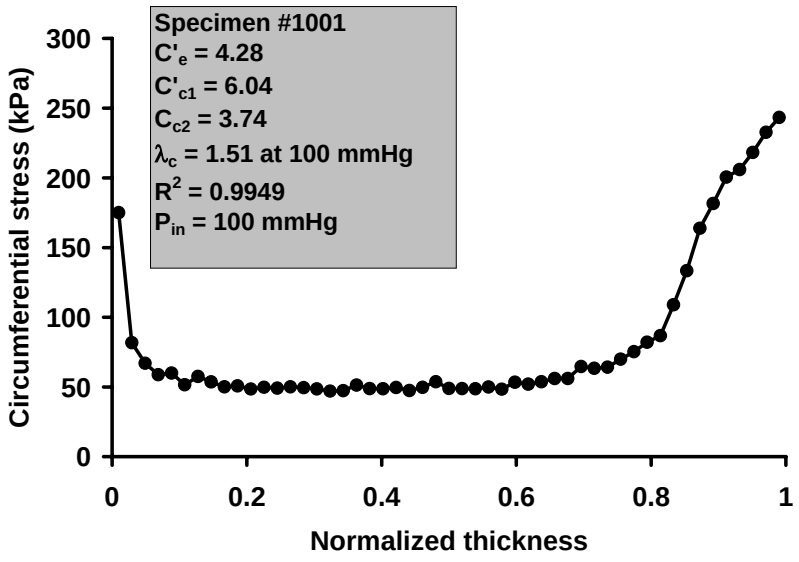

Figure 5.35: The intramural distribution of circumferential stresses (•) in 51 layers computed using the heterogeneous model for sample #1001 (normotensive).

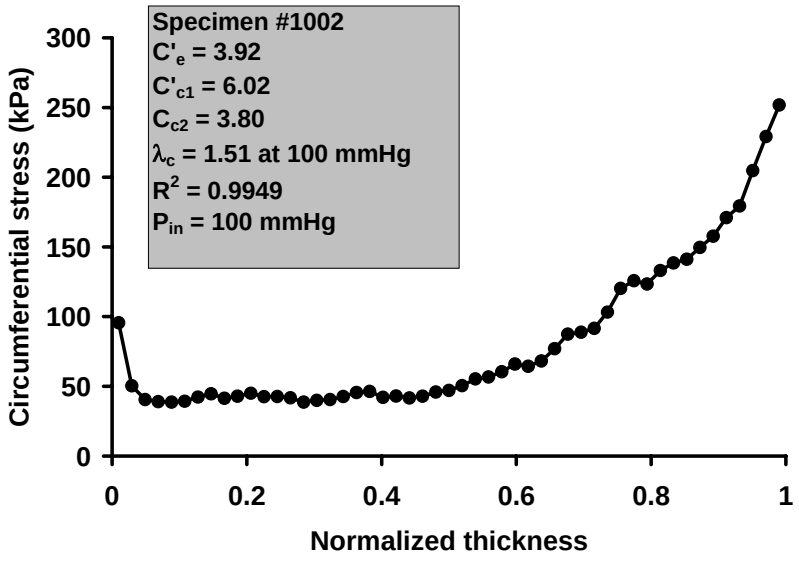

Figure 5.36: The intramural distribution of circumferential stresses (•) in 51 layers computed using the heterogeneous model for sample #1002 (normotensive).

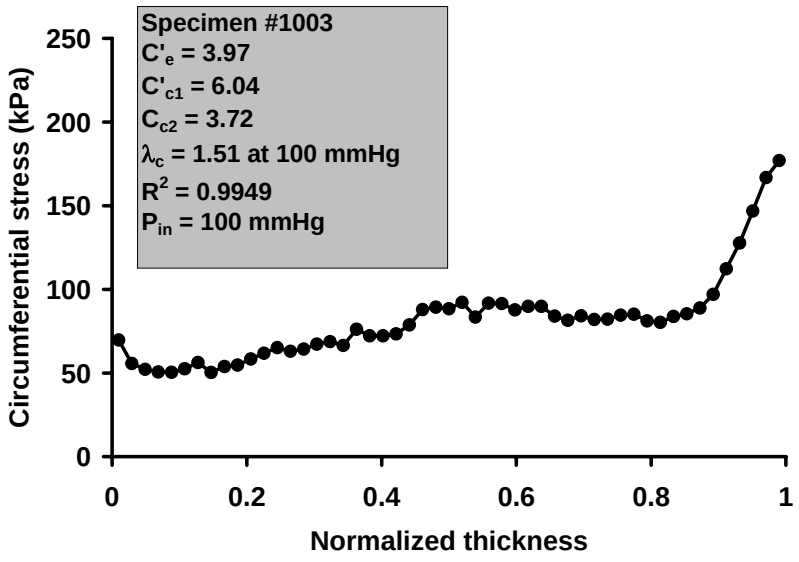

Figure 5.37: The intramural distribution of circumferential stresses (•) in 51 layers computed using the heterogeneous model for sample #1003 (normotensive).

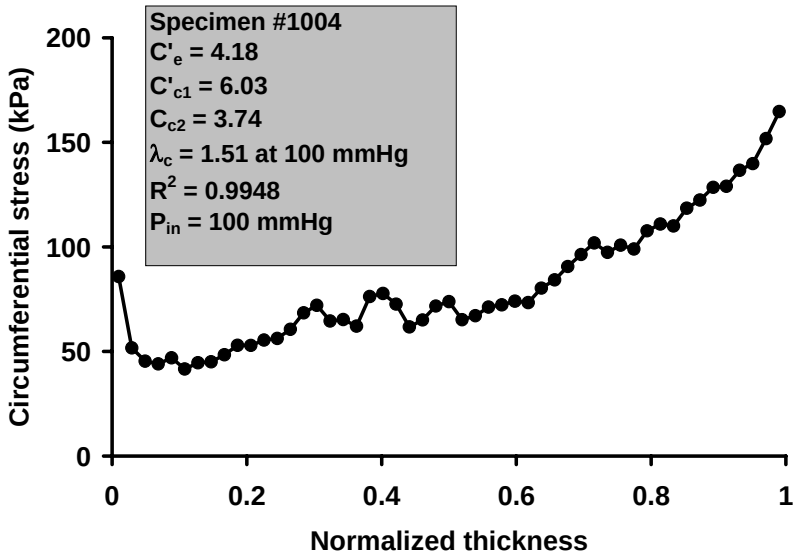

Figure 5.38: The intramural distribution of circumferential stresses (•) in 51 layers computed using the heterogeneous model for sample #1004 (normotensive).

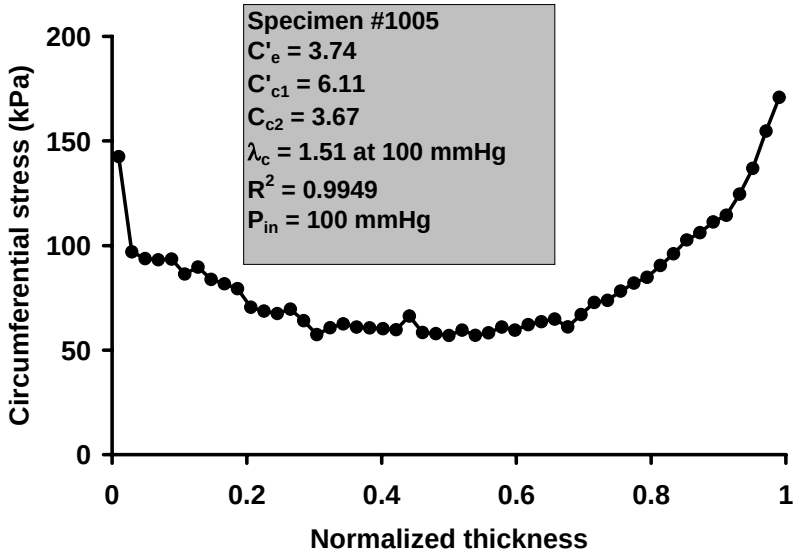

Figure 5.39: The intramural distribution of circumferential stresses (•) in 51 layers computed using the heterogeneous model for sample #1005 (normotensive).

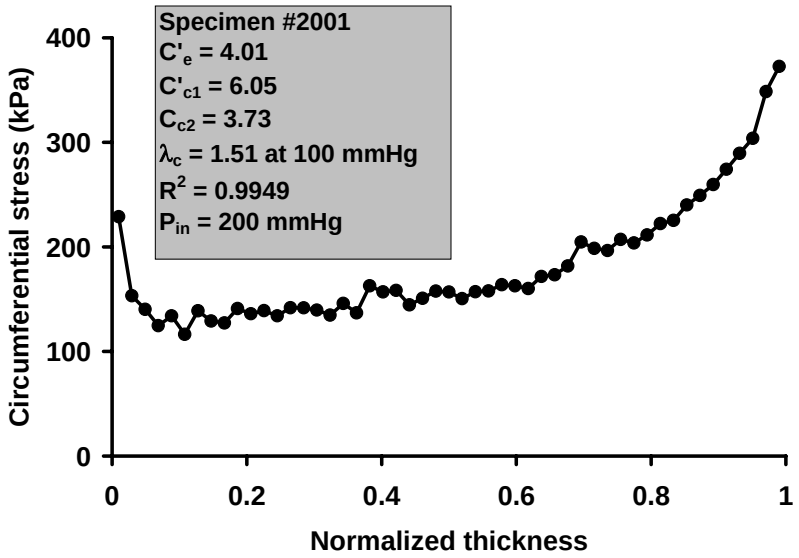

Figure 5.40: The intramural distribution of circumferential stresses (•) in 51 layers computed using the heterogeneous model for sample #2001 (hypertensive).

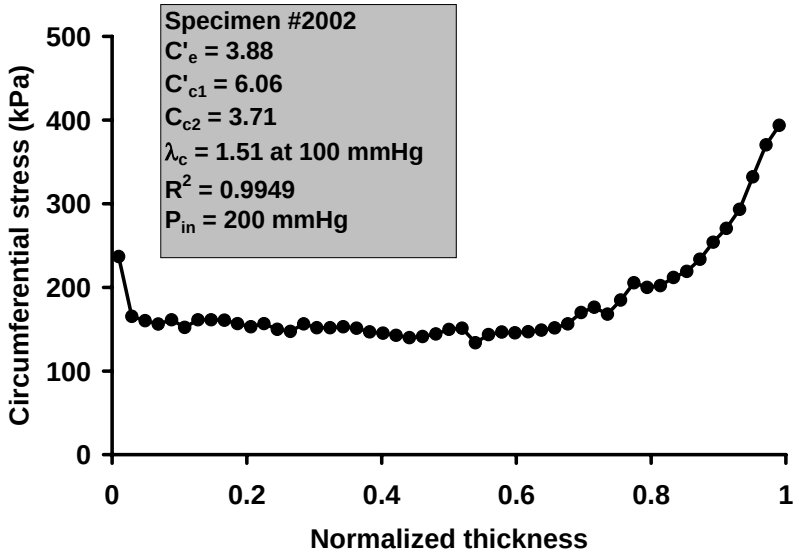

Figure 5.41: The intramural distribution of circumferential stresses (•) in 51 layers computed using the heterogeneous model for sample #2002 (hypertensive).

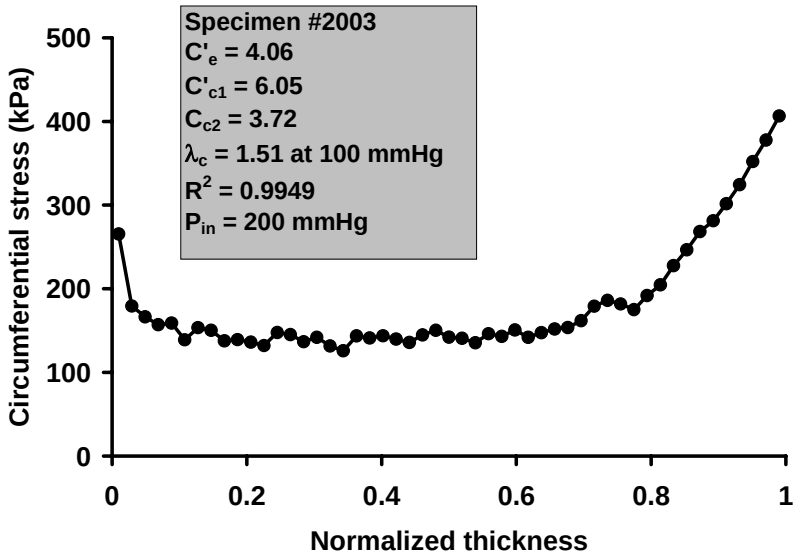

Figure 5.42: The intramural distribution of circumferential stresses (•) in 51 layers computed using the heterogeneous model for sample #2003 (hypertensive).

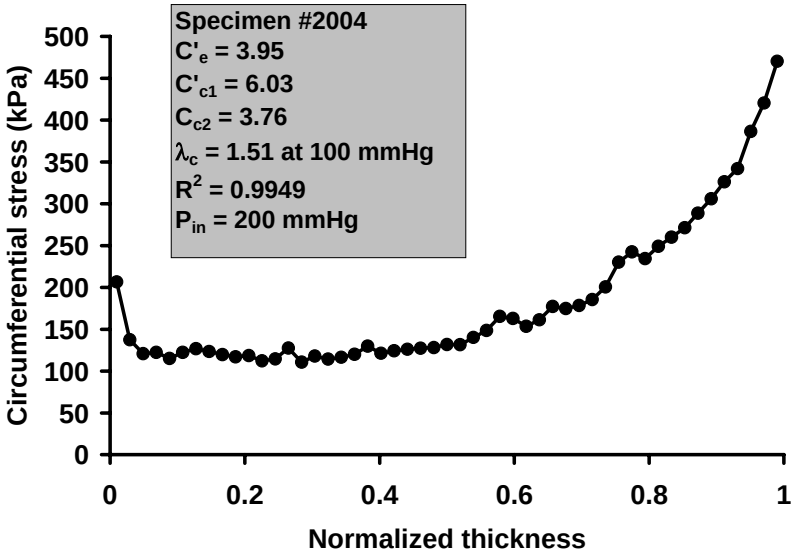

Figure 5.43: The intramural distribution of circumferential stresses (•) in 51 layers computed using the heterogeneous model for sample #2004 (hypertensive).

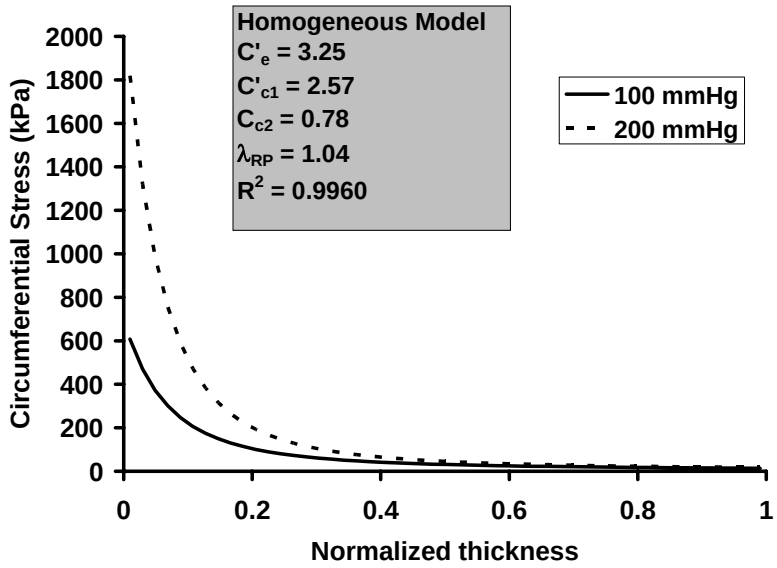

Figure 5.44: The intramural distributions of circumferential stresses at 100 mmHg (solid line) and at 200 mmHg (dashed line) computed using the homogeneous model.

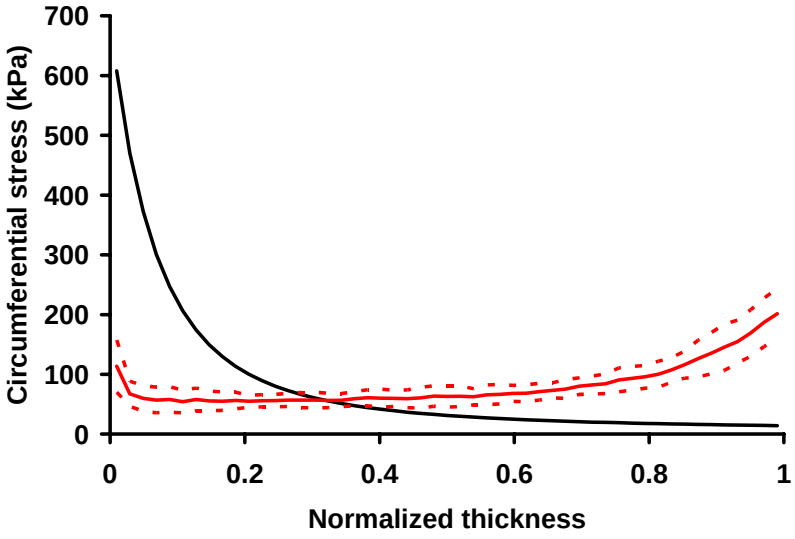

(A)

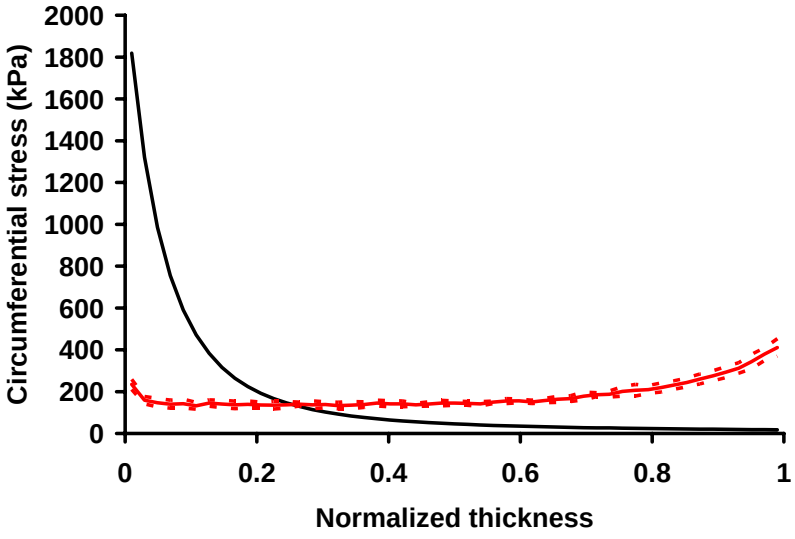

(B)

Figure 5.45: The intramural distributions of circumferential stresses computed using the homogeneous model (black solid line) and the heterogeneous model shown as mean (red solid line) ± S.D. (red dashed line) at 100 mmHg (A) and 200 mmHg (B) were plotted together.

Correlation between Circumferential Stress and the Expression and Activation of MMP-2 and MMP-9

Table 5.6 shows the Spearman rank correlation coefficients between the computed circumferential stress and the expression and activation of MMP-2 and MMP-9 for individual specimens. In normotensive arteries, circumferential stresses computed using the heterogeneous model positively correlated to the expression of MMP-2 (mean $r_s = 0.72$; $p = 0.01$; n = 5), the expression of MMP-9 (mean $r_s = 0.70$; $p < 0.01$; n = 5), and the activation of MMP-2 and MMP-9 (mean $r_s = 0.80$; $p < 0.01$; n = 5). In hypertensive arteries, circumferential stresses computed using the heterogeneous model also positively correlated to the expression of MMP-2 (mean $r_s = 0.82$; $p = 0.01$; n = 4), the expression of MMP-9 (mean $r_s = 0.83$; $p < 0.01$; n = 4), and the activation of MMP-2 and MMP-9 (mean $r_s = 0.81$; $p < 0.01$; n = 4).

In normotensive arteries, circumferential stresses computed using the homogeneous model negatively correlated to the expression of MMP-2 (mean $r_s = -0.79$; $p < 0.01$; n = 5), the expression of MMP-9 (mean $r_s = -0.56$; $p = 0.01$; n = 5), and the activation of MMP-2 and MMP-9 (mean $r_s = -0.86$; $p < 0.01$; n = 5). In hypertensive arteries, circumferential stresses computed using the homogeneous model also negatively correlated to the expression of MMP-2 (mean $r_s = -0.84$; $p < 0.01$; n = 4), the expression of MMP-9 (mean $r_s = -0.69$; $p < 0.01$; n = 4), and the activation of MMP-2 and MMP-9 (mean $r_s = -0.83$; $p < 0.01$; n = 4).

Circumferential strains computed using incompressibility negatively correlated to the expression and activation of MMP-2 and MMP-9, which is inconsistent with the positive correlation between MMP-2 and MMP-9 and mechanical stretch established in cell culture studies. Both of computed circumferential stresses using the heterogeneous and the homogeneous models significantly correlated to the expression and activation of MMP-2 and MMP-9. However, the heterogeneous model predicted that higher

circumferential stress in the ECM scaffold correlates to higher expression and activation of MMP-2 and MMP-9, while the homogeneous model predicted the opposite relationships.

Table 5.6: Spearman rank correlation coefficients (r_s) between the predicted local circumferential stress (σ_θ) and the expression and activation of MMP-2 and MMP-9 for normotensive arteries (#1001 – #1005) and hypertensive arteries (#2001 – #2004). All correlations were statistically significant ($p < 0.01$; *$p < 0.05$) except one case (†$p = 0.06$).

	Model	MMP-2 expression vs. σ_θ (r_s)	MMP-9 expression vs. σ_θ (r_s)	Gelatinolytic activity vs. σ_θ (r_s)
#1001	heterogeneous	0.7054	0.8613	0.6709
	homogeneous	-0.8586	-0.4767	-0.9001
#1002	heterogeneous	0.9233	0.8172	0.9360
	homogeneous	-0.8757	-0.6173	-0.8828
#1003	heterogeneous	0.4017	0.7442	0.7788
	homogeneous	-0.6219	-0.8170	-0.8734
#1004	heterogeneous	0.9383	0.3231*	0.9543
	homogeneous	-0.8907	-0.2179†	-0.9119
#1005	heterogeneous	0.6506	0.7300	0.6434
	homogeneous	-0.7079	-0.6545	-0.7070
#2001	heterogeneous	0.9386	0.8302	0.9227
	homogeneous	-0.8658	-0.6896	-0.9285
#2002	heterogeneous	0.6611	0.6919	0.6893
	homogeneous	-0.7805	-0.6895	-0.7255
#2003	heterogeneous	0.7455	0.8558	0.7277
	homogeneous	-0.8293	-0.6420	-0.9309
#2004	heterogeneous	0.9260	0.9262	0.9115
	homogeneous	-0.8646	-0.7319	-0.7374

CHAPTER 5

DISCUSSION

Distributions of Elastin and Collagen

The area fraction of elastin was greatest at the IEL and was generally uniform through most of the medial layer with a moderate increase in the EEL. Based on the Spearman rank correlation coefficients, the distribution of elastin showed a positive trend toward the outer layer. However, the distribution of elastin showed a negative trend toward the outer boundary of the media when the thick EEL was excluded. Although the distribution of elastin may be specific to the types and species of arteries, similar trends were observed in other studies. In bovine carotid arteries, the area fraction of elastin decreased toward the outer media (Hasan and Greenwald 1995). The concentration of medial elastin decreased from the intima to the adventitia in the human aortas of children aged between 8 days and 12 years (Feldman and Glagov 1971).

The area fraction of collagen fibers in the media was small and relatively uniform in the inner media and gradually increased toward the outer boundary of the media. The area fraction of collagen fibers was the largest at the medial-adventitial border including the EEL. In the inner half of the wall, collagen fibers were denser at the IEL compared to the inner media. Spearman rank correlation coefficients for the distribution of collagen fibers indicated a strong positive trend toward the outer layer. The result is qualitatively in agreement with observations from previous studies which showed relatively high amounts of collagen fibers near the outer media (Feldman and Glagov 1971; Merrilees et al. 1987; Hasan and Greenwald 1995; Stergiopulos et al. 2001).

The distributions of elastin and collagen fibers are expected to be the product of cell activities and influence the mechanical behavior of arterial tissue. The layer of dense

collagen fibers at the outer boundary of the media was also observed in human cerebral arteries (Finlay et al. 1995; Rowe et al. 2003). Although the origin of collagen fibers in this layer is unclear, the coalignment of collagen fibers and VSMCs suggests that these collagen fibers are produced and organized by VSMCs. Collagen fibers in the inner adventitia were also aligned more circumferentially than those in the outer adventitia, where collagen fibers were more obliquely aligned (Canham et al. 1992). The structural redundancy of collagen fibers in the medial-adventitial border may be needed to maintain structural stability between layers with different microstructures. This suggests that the outer layer of the arterial media may provide more mechanical strength compared to the inner layer. The IEL showed a small peak in the area fraction of collagen fibers suggesting its role in providing mechanical strength at the inner boundary of the media. The higher content of matrix proteins at both sides of the media suggests the importance of passive mechanical support in these regions. The uniform distribution of elastin in the media suggests that the network of elastin lamellae, interconnected by branching and merger, facilitate relatively uniform load transfer through the media.

The distribution of collagen fibers are expected to contribute to the reduction of stress gradients through the arterial wall. Considering the differences in stiffness between elastin and collagen fibers, the intramural distribution of stress is more sensitive to the distribution of collagen fibers than elastin distribution. The larger area fraction of collagen fibers in the outer media implies that structural stiffness is higher in the outer media than the inner media. Due to the cylindrical geometry and incompressibility, the increase of strain in response to the increase of pressure is always higher at the inner layer. Under physiologic conditions, the pulsatility of blood flow also causes higher strain fluctuation at the inner layer than the outer layer. Thus, higher structural stiffness in the outer layer compensates for low strain in the outer layer and makes the distribution of stress more uniform. The distribution of collagen fibers may indicate that VSMCs work to maintain the optimum mechanical environment for their functionality. In addition to

the residual stress, the distribution of collagen seems to contribute to a more uniform distribution of stress.

The heterogeneity of the ECM may contribute to localized cell activities in response to the mechanical stimuli. The distributions of elastin and collagen fibers may influence the variation in coupling between matrix proteins and cells through an arterial wall and affect the mechanical environment sensed by VSMCs. Many studies suggest the role of specific types of ECM proteins in transmitting mechanical signals to anchored cells. Wilson et al. (1995) suggest that specific matrix-cell interactions may be involved in mechanotransduction, which may differ from those involved in adhesion. Koyama et al. (1996) showed that the structure of cytoskeleton and the formation of focal adhesions depends on the type of ECM protein cells are anchored to. Many studies suggest that ECM-cytoskeleton interactions are involved in mechanotransduction, which appears to be mediated by transmembrane ECM receptors such as integrin (Carey 1991; Wilson et al. 1995).

The distribution of elastin and collagen fibers may play a role in regulating VSMC functions. Peyton and Putnam (2005) showed that the motility and cytoskeletal assembly of VSMCs depend on the stiffness of the underlying substrate and the concentration of ECM protein covalently attached to the substrate. Thus, the mechanical properties of the ECM may regulate the contractility and migration of VSMCs. Elastin is known to modulate VSMC phenotype. It was shown that elastin inhibits proliferation and regulates migration of VSMCs by modulating the contractile organization of VSMCs (Karnik et al. 2003a; Karnik et al. 2003b). Thus, elastin induces a quiescent contractile state in VSMCs and stabilizes the arterial structure. High concentrations of elastin at the IEL and the EEL may act as barriers for preventing VSMC migration across these borders.

In this study, the distributions of elastin and collagen fibers through the wall of young porcine common carotid arteries were measured using their optical properties. The

optical measures are influenced by many factors such as conditions for staining and imaging. The opacity of the embedding medium and photo bleaching of the sections can cause variations in the overall intensity of elastin images. Conditions for staining to enhance collagen birefringence can cause variations in the overall intensity of collagen images. Thus, the method for optimal measurement is only semi-quantitative. It was assumed that the average intensity of pixels is linearly proportional to the concentration of matrix protein in the area of interest. With this assumption, the normalized distributions of elastin and collagen fibers are maintained regardless of their estimated concentrations.

VSMC Nuclear Geometry

The lengthening of VSMC nuclei in response to an increase of luminal pressure affirms the structural continuity among the ECM, cytoskeleton, and nuclear matrix. The deformation of cell nuclei in response to the external force was also observed in other types of tissue. Arnoczky et al. (2002) observed the lengthening of cell nuclei in tendons from adult Spraque-Dawley rats under tensile load. Tensions in the ECM and cytoskeleton are likely responsible for the mechanical strain of VSMC nuclei at 100 mmHg. Our results suggest that VSMC nuclei have potential for acting as local strain gauges in the arterial tissue.

The distributions of both major and circumferential lengths of VSMC nuclei were uniform at 100 mmHg. These results suggest that the strain of VSMC nuclei under physiologic loading is uniform through the arterial media in agreement with previous observations made by Fung (1984). Assuming incompressibility and the uniform distribution of circumferential strain through arterial wall at 100 mmHg, it is expected that the length of VSMC nuclei is shortest in the innermost layer and monotonically increases toward the outer layer at 0 mmHg. However, this was only true for the inner 70% of the media. Although the Spearman rank correlation coefficients showed a

positive trend in the distributions of the major and circumferential lengths of VSMC nuclei at 0 mmHg, the trend in the outer 40% of the media was either not significant or significantly negative. This could imply that the coupling between ECM and VSMC is different in the outer media from the rest of the media. Another possibility is that the phenotype of VSMCs in the outer media may be different from that in the rest of the media. Synthetic phenotype VSMCs express less amounts of contractile and adhesion proteins compared to contractile phenotype VSMCs. The organization of cytoskeleton and contractile elements is also different between two phenotypes of VSMCs (Worth et al. 2001). Since cytoskeleton and contractile elements acts as a force transmitter between focal adhesions and the nuclear envelope, the quantitative change and reorganization of cytoskeleton and contractile elements may change the coupling between ECM and VSMCs and the mechanical behavior of VSMC nuclei. More detailed microscopic data are necessary to verify these possibilities.

The stretch of VSMC nuclei in the circumferential direction was smaller compared to the circumferential stretch of arterial tissue. This suggests that the modulus of VSMC nuclear matrix may be higher than the modulus of cytoskeleton and surrounding tissue. However, the modulus of the nuclear envelope is thought to be close to the modulus of elastin, which is ~0.6 MPa (Fung 1993). Kuo and Seow (2004) estimated a modulus of 685 ± 116 kPa for the nuclear envelope of a porcine tracheal smooth muscle cell. Thus, the difference in the stretch ratios between VSMC nuclei and arterial tissue is not likely due to the modulus difference. Rather, the difference may due to the mechanism for the transmission of mechanical load from cell boundaries to a nuclear envelope. The nuclear envelope of VSMC is connected to the cell membrane via actin filaments, which transmit tensional forces. Once actin filaments lose their tension during depressurization, the deformations of VSMC nuclei may depends on compressive body forces and involve interactions with tissue components which bear compression rather than tension. Another possibility is that the reference configuration of VSMC

strain is not the cut-opened configuration of an arterial sector. It was shown that the removal of VSMCs has no effect on the opening angle of arteries (Greenwald et al. 1997). This suggests that VSMCs may not have residual strain at no load conditions, thus the reference configuration of VSMC strain may be different from the zero stress configuration of arteries. A detailed microstructural study of VSMC under various loading conditions is necessary to investigate possibilities mentioned above.

The uniform distribution of VSMC nuclear strain at 100 mmHg implies the uniform strain of collagen fibers through the media. VSMCs are responsible for the remodeling of collagen fibers in the media. The coalignment of VSMCs and collagen fibers was observed in mechanically conditioned tissue-engineered blood vessel constructs (Seliktar et al. 2000) and in the media of arteries *in situ* (Canham et al. 1986; Finlay et al. 1991). The reorganization of collagen fibers mediated by VSMCs was observed *in vitro*. When cyclic circumferential stretch was applied to the tissue-engineered blood vessel constructs composed of VSMC-seeded collagen-gel scaffold, VSMC-mediated reorganization of surrounding collagen matrix resulted in the circumferential alignment of collagen fibers as well as VSMCs *in vitro* (Seliktar et al. 2000). VSMC nuclei, cytoskeleton, and collagen fibers can be considered as a continuous mechanical structure, where the length of a VSMC nucleus depends on the deformation of cytoskeleton and collagen fibers to which the cell is anchored.

The helical and radial angles of VSMCs at both pressures were symmetric. Such symmetry was also observed in the helical angles of smooth muscle and collagen fibers in the media of human brain arteries *in situ* (Finlay et al. 1991) and in the stained patch of human aortic media (Holzapfel et al. 2002). Assuming the symmetry between left-handed and right-handed helices, the average of helical angles should be zero. Although the average of helical angles was significantly different from 0° in three groups, the differences were small and thought to be due to the alignment error. Porcine common carotid arteries are generally straight in the axial direction. However, the curvature of

arteries does exist and changes *in vivo* depending on the posture of a host animal. Since the error was small, the helical angles were considered to be symmetric in the analysis. The average of radial angles was not significantly different from 0° indicating that inward- and outward-spiral orientations of VSMC nuclei are symmetric.

Although the orientation of VSMC nuclei was symmetric at both pressures, the orientation of VSMC nuclei were more uniform and coherent at 100 mmHg as shown by insignificant Spearman rank correlation coefficients and decreased standard deviations compared to those at 0 mmHg, respectively. Such a trend was also seen for collagen fibers in the subendothelium, the media, and the adventitia of human cerebral arteries as they were more aligned at higher pressures (Canham et al. 1992; Finlay et al. 1995). While the helical and radial deviations of VSMC nuclei were uniformly distributed at 100 mmHg, they were higher near both boundaries of the media at 0 mmHg, especially near the intima. The wavy nature of inner layers at 0 mmHg due to compressive forces in the circumferential direction is thought to be responsible for the increased variability in the helical and radial angles. With the incompressibility assumption, it is expected that the variability of VSMC orientation increases more toward inner layers as pressure decreases. Considering that the arteries were kept axially stretched at 0 mmHg, stretched collagen fibers in the intima and the adventitia may also be responsible for the distribution of helical and radial deviations. Collagen fibers are known to be aligned more longitudinally (i.e. larger helical deviation) at the subendothelium and the adventitia than at the media. The changes in collagen orientation are more gradual at the medial-adventitial border than at the intimal-medial border (Canham et al. 1992; Finlay et al. 1995). It was shown that the degree of anisotropy changes in response to the deformation in the axial and/or circumferential direction (Dobrin 1986). The changes in the helical and radial deviation in response to pressure change suggest that the orientation of collagen fibers changes in response to the tissue deformation. Such change may be partially responsible for the change of arterial anisotropy and was included in some SEFs

(Holzapfel et al. 2002; Zulliger et al. 2004). More experimental data are in need to characterize the interaction and coupling between VSMCs and ECM *in situ*.

Distribution of Circumferential Stress

In this study, a heterogeneous mechanical model of arterial tissue including the distributions of elastin and collagen fibers was developed. This model is a novel extension of the constrained-mixture models and represents the heterogeneous structure of the arterial media. Using the heterogeneous model, we investigated potential effects of the heterogeneity of ECM proteins on the transmural distributions of stress and strain and its implications for the physiological response of VSMCs. For comparison, stresses were also computed using a homogeneous model with uniform area fractions of elastin and collagen fibers and a fixed collagen recruiting point through the arterial wall. To improve the utility of models for studying cellular behaviors, it is necessary to introduce microstructural information into mechanical modeling.

The opening angle of common carotid arteries from six to seven-month-old pigs was a highly variable measure ranging from 0.64° to 75.21°. In this study, the cross-section of a radially cut and opened arterial ring was used as the reference geometry for the computation of strain. Hence residual strain was included in both the heterogeneous and the homogeneous models. In previous studies, homogeneous models accounting for residual strain showed that including residual strain significantly reduces the stress gradient near the intima (Chuong and Fung 1986; Matsumoto and Hayashi 1996; Rachev et al. 1996; Chaudhry et al. 1997). In this study, residual strain reduced the stress gradient near the intima but was not enough to make the circumferential stress uniform through the arterial wall using the homogeneous model. This is mainly due to the smaller opening angle of young porcine carotid arteries (~42°) compared to those reported for other arteries. For example, a mean opening angle of rabbit carotid arteries reported by Li and Hayashi (1996) is 95°, which was also not enough to make the circumferential stress

uniform. In addition, it was shown that the opening angle is dependent on elastin but not on collagen fibers and VSMCs (Greenwald et al. 1997). Thus, the increase of opening angle with age may relate to the decrease of elastin with age. Considering the low turnover rate of elastin, such a change may be due to the plastic deformation of elastin rather than growth or remodeling activity. Thus, residual strain computed from the opening angle is generally not enough to make the stress distribution reasonably uniform through the arterial wall.

The transmural distributions of local circumferential stress were computed using models assuming homogeneous and heterogeneous material properties. In the homogeneous model, circumferential stress peaked at the intima and decreased toward the outer layer. The distribution of circumferential stress in the media computed using the homogeneous model is qualitatively in agreement with the results from previously introduced models assuming a homogeneous media, e.g. (Holzapfel and Gasser 2000). It is necessary, although not sufficient, to verify the methodology. The transmural distribution of circumferential stress in the heterogeneous model was significantly different from the homogeneous model and skewed "U"-shaped with the higher stresses at the IEL and the EEL. The result of the heterogeneous model suggests, as noted, that both boundaries of the media, especially the outer media, may provide more mechanical support of luminal pressure. The distribution of circumferential stress computed using the heterogeneous model was closer to a uniform distribution when compared to the circumferential stress distribution computed using the homogeneous model. Such a distribution is mainly due to the distribution of collagen fibers and the assumption introduced about collagen recruiting. This implies that the heterogeneity of ECM proteins is critical for the uniform distribution of external forces in addition to residual stress.

A limitation of the methodology is the use of average pressure-diameter relations. Using measurements taken with each specimen may enhance the correlation between cellular activities and model predictions. However, the previously measured pressure-

diameter relations of the same type of arteries were used in this study to avoid possible cellular responses to the change of mechanical environment during the measurements. With this limitation, actual values for stresses may be different from computed stresses, but the distributions still hold under proposed assumptions. Other limitations are from the assumptions used in the modeling. The reference configurations of collagen fibers were computed assuming a uniform strain distribution under physiologic conditions. Although, it is a reasonable assumption based on the histological observations of VSMC nuclei, the microstructural information on collagen fibers under various loading conditions is still necessary to verify the reference configurations of collagen fibers. The SEFs for elastin and collagen fibers used in the model are in widely accepted forms. However, these SEFs are theoretical and need to be supported by experiments using the corresponding components.

Distributions of Expression and Activation of MMP-2 and MMP-9

The expressions of MMP-2 and MMP-9 and their gelatinolytic activities in young poncine common carotid arteries cultured *ex vivo* were generally higher in the outer media. The results qualitatively agreed with previous observations, which reported higher expression and activation of MMP-2 and MMP-9 in the outer media of arteries *ex vivo* (Chesler et al. 1999; Mavromatis et al. 2000) or *in vivo* (Wilson et al. 2002). Results from experiments using cultured VSMCs showed that mechanical stretch positively correlates to the production of MMP-2 and MMP-9 by VSMCs (O'Callaghan and Williams 2000; Asanuma et al. 2003). Thus, VSMCs in the outer media may sense higher mechanical strain resulting in higher expression and activation of MMP-2 and MMP-9. However, circumferential strains in arteries computed assuming incompressibility are generally low in the outer media at physiologic loading conditions. This is inconsistent with results from experiments using cultured VSMCs. This contradiction raised a question whether mechanical strain is the stimulus for the production of MMP-2 and MMP-9 by VSMCs or

not. In addition, since it is the matrix proteins that transmit loads to VSMCs, the stress and strain computed using a phenomenological model, especially assuming homogeneity, may not represent what is sensed by VSMCs.

The high levels of MMP-2 and MMP-9 in the outer media suggests localized remodeling activities in this region of arterial tissue. MMP-2 and MMP-9 are known to be involved in the VSMC migration (Johnson and Galis 2004). MMP-9 was also shown to be involved in the VSMC-mediated fibrillar collagen assembly (Johnson and Galis 2004; Defawe et al. 2005). Xu et al. (2000) observed localized gene expression for collagen type I in the outer media and adventitia of rabbit aortas in response to an acute increase in blood pressure. They suggested that mechanical stress associated with increase in pressure is responsible for the distribution of collagen gene expression. Thus, the localization of MMP-2 and MMP-9 seems to be associated with the mechanical role of the outer media in response to the alteration in blood pressure. Considering arteries are from six to seven-month-old pigs, the expression and activation of MMP-2 and MMP-9 may also be related to the normal outward growth of these arteries under physiologic conditions.

In this study, the expression and activation of MMP-2 and MMP-9 were correlated to circumferential stresses in normotensive and hypertensive arteries, separately. The intensities of immunostaining for MMP-2 and MMP-9 in porcine carotid arteries were slightly lower in hypertensive arteries than normotensive arteries. Similarly, arteries and veins investigated in an *ex vivo* organ culture system have been reported to show lower tissue levels of MMP-2 and MMP-9 at higher luminal pressures. The tissue levels of MMP-2 was lower in porcine carotid arteries perfused *ex vivo* with steady flow at 200 mmHg than those perfused at 100 mmHg (Chesler et al. 1999). The tissue levels of MMP-2 and MMP-9 were also reduced in human saphenous veins at higher pressure (Mavromatis et al. 2000). However, the difference in the detected amount of MMP-2 and MMP-9 does not mean the difference in the production of MMP-2 and MMP-9 between

normotensive and hypertensive arteries. Various cell functions affect the levels of the expression and activation of MMP-2 and MMP-9 detected in arterial tissue. Compared to *in vivo* experiments, *ex vivo* organ culture experiments provides better control over the biochemical and mechanical environment of arterial tissue. However, changes in mechanical environment triggers a biological chain reaction, which ultimately affects the balance of biological products in arterial tissue. Thus, further analysis by Mavromatis et al. (2000) revealed that actual production of MMP-2 and MMP-9 by VSMCs increased at higher pressure. They found that the increased extracellular superoxide due to decreased tissue levels of extracellular superoxide dismutase increased post-translational processing leading to MMP protein degradation. Also increased levels of MMP-9 in the culture media suggested rapid secretion and low tissue retention of MMP-9 (Mavromatis et al. 2000). On the contrary, the tissue levels of MMP-2 and MMP-9 in mouse carotid arteries were observed to increase at higher pressure (Lehoux et al. 2004). This suggests that the ratios of MMP-2 and MMP-9 retained in tissue may be species-dependent. Thus, the correlation between pressures and the tissue levels of MMP-2 and MMP-9 was not shown, and extensive biochemical analysis was beyond the scope of this study.

MMP-2 and MMP-9 are also expressed and activated by other types of cells, especially macrophages and fibroblasts in the media and adventitia. Once released, MMP-9 can diffuse in the interstitial space due to its low tissue retention (Mavromatis et al. 2000), which may affect the distribution of the expression and activation of MMP-9 shown in this study. However, the EEL forms a barrier, which is expected to block the diffusion of such molecules between the media and the adventitia. Since the distributions of MMP-2 and MMP-9 levels were quantified in the range between the IEL and the EEL, the effect of fibroblasts in the adventitia and the diffusion of MMP-9 on our result were considered to be minimal. Also, the effects of inflammatory cells on the expression and activation of MMP-2 and MMP-9 were considered to be small, since an *ex vivo* organ culture study utilizes excised arteries and lacks additional recruitment of inflammatory

cells such as macrophages. Major limitations in *ex vivo* organ culture experiments are the lack of interactions between arteries and surrounding tissue and the inability to induce inflammatory responses seen in *in vivo* experiments (Capers et al. 1997).

Correlation between Circumferential Stress and the Expression and Activation of MMP-2 and MMP-9

The localized expression and activation of MMP-2 and MMP-9 were compared to the distributions of circumferential stress and strain computed using the heterogeneous and homogeneous models. In both models, the circumferential strain is highest at the inner boundary and gradually decreased toward the outer layer. The distribution of circumferential strain in both models and the distribution of circumferential stress in the homogeneous model negatively correlated to the distributions of the expression and activation of MMP-2 and MMP-9.

However, the stress distribution determined from the heterogeneous model positively correlated to the expression and activation of MMP-2 and MMP-9. This makes conforming connections between results from experimental studies using cultured VSMCs and arterial tissues. Assuming that the cells are uniformly coupled to substrates in cell culture experiments, it is reasonable to expect that mechanical stress as well as strain positively correlates to the observed cellular response. As noted earlier, strains at the tissue level may not be the strain sensed by VSMCs. Thus, the collocation and correlation of stress in the heterogeneous model with tissue levels of MMP-2 and MMP-9 is in agreement with results from cell culture studies. We interpret this agreement with the expected biological response to stress as support for the validity of the model and the likely importance of mechanical stress in arterial remodeling.

The result suggests that the remodeling activities of VSMCs may correlate better with stresses rather than strains. It is well accepted that the arterial wall remodels by thickening in response to increased wall stress in order to decrease it back to normal

levels (Liu and Fung 1989; Matsumoto and Hayashi 1994). This implies that areas of high stress may be sites of localized remodeling. Fridez et al. (2003) observed that, in response to induced hypertension, the outermost layer of rat carotid artery thickens more as compared to the inner layers. This suggests that circumferential stress in the outermost layer may be higher than that in the inner layer, which is consistent with the stress distribution computed using the heterogeneous model developed in this study. Xu et al. (2000) showed that induced hypertension also initiates rapid gene expression for collagen type I predominantly in the outer media and adventitia of rabbit aortas. Increased collagen support, as the authors note, suggests that these zones of the aortic wall may provide an increase in tensile support. The heterogeneous model developed in this study shows the importance of mechanical stress in understanding these results. In contrast to these results, Matsumoto and Hayashi (1994) observed a higher thickening of the innermost layer in the adaptation of rat aorta to Goldblatt hypertension at 8 weeks. The difference between results may due to experimental methods, the type of arteries, and/or the host animal of arteries.

The distributions of stresses and responses of cells observed in this study may not be applicable to other types of arteries, but the methodology developed will be applicable in general. It is important to note that microstructure varies along the arterial tree. Thus, we need to take a more complex view of arterial remodeling processes, both adaptive and maladaptive, and recognize that they may be specific to each arterial type. We conclude that the heterogeneity of the tissue microstructure, whether in the arterial wall or tissue engineered construct, should be considered explicitly when using mechanical models to better understand cellular functions *in situ*.

CHAPTER 6

CONCLUSIONS AND FUTURE WORKS

Conclusions

In this study, we proposed a novel mathematical model of arterial tissue representing the heterogeneous nature of the arterial media. The heterogeneous model accounts for nonlinearity, residual strain, anisotropy, and structural heterogeneity. To our knowledge, this is the first mechanical model of arterial tissue that includes the heterogeneous distributions of ECM components through the arterial media. Major matrix proteins, elastin and collagen fibers, were assumed to be hyperelastic materials and described using SEFs. Residual strains were included considering the zero stress configuration as a circular sector with the opening angle. Anisotropy was represented by the direction of collagen fibers, which was measured as the helical angle of VSMC nuclei. Structural heterogeneity was represented by the distributions of elastin and collagen fibers, which were quantified using their optical properties. The reference configuration of elastin was assumed to be the zero stress configuration of arterial tissue. The recruiting points of collagen fibers were computed assuming uniform strain of collagen fibers under physiological loading conditions.

The distributions of circumferential stresses computed using the heterogeneous model and homogeneous model were compared to investigate the effect of structural heterogeneity. Also, the heterogeneous model was indirectly validated by correlating circumferential stresses with the expression and activation of MMP-2 and MMP-9 using porcine common carotid arteries. From this study, following conclusions were drawn:

- Common carotid arteries from young pigs show significant heterogeneity in the medial structure.

- The length of VSMC nuclei in porcine common carotid arteries increases in response to the tension in the circumferential direction.
- The orientations of VSMC nuclei in porcine common carotid arteries are symmetric.
- The length and orientation of VSMC nuclei in porcine common carotid arteries at physiologic loading are uniform across the arterial wall.
- The opening angle of porcine common carotid arteries reduces the gradient of circumferential stress, but it is not sufficient to make a uniform stress distribution.
- The structural heterogeneity of the media makes circumferential stress even more uniform than only accounting for the residual strain.
- The material properties of porcine common carotid arteries are heterogeneous with stiffer outer layers.
- The expression and activations of MMP-2 and MMP-9 in porcine common carotid arteries positively correlate with circumferential stresses computed using the heterogeneous model.

Future Works

Our long term goal is to promote the understanding of the mechanobiology of VSMCs and the physiology and pathophysiology of arteries. This study contributed to the long term goal by providing insights into the effect of structural heterogeneity on the mechanical environment and responses of VSMCs. The limitations and problems revealed in this study provide recommendations for further improvements:

- *Explore quantitative measures of the structural elements of arterial tissue*

  Quantitative descriptions of structural components are essential for the proper representation of the mechanical environment of cells. In this study, the heterogeneous distributions of area fractions of elastin and collagen fibers were measured. In addition to the amounts of matrix proteins, characterizing their local

structure and the coupling between matrix and cells are important to understand the mechanical environment of cells. Histology-based measures are often semi-quantitative. Thus, techniques for the quantification of microstructural elements also need to be developed.

Our result suggests that the types of VSMCs may vary across the arterial wall. In other words, the internal structures, especially those related to intracellular mechanotransduction, of VSMCs may change across the thickness. The different organization of cytoskeleton and contractile elements may differentiate the coupling between ECM and VSMCs and the mechanical behavior of VSMC nuclei. This needs to be verified using more detailed microscopic data.

- *Improve a mathematical model for better representation of mechanics of vascular tissue*

The limitations of the heterogeneous model, proposed in this study, lies in assumptions made. Stretch ratios of collagen fibers were computed assuming uniform strain under physiologic loading conditions. As shown by the dependence of the opening angle on elastin, each component of arterial tissue has its own reference configuration, which is critical for accurate computation of stresses and strains. Currently, the reference configuration of each element is generally not available. Comparison between model predictions and recorded mechanical responses of arteries can provide insights into the reference configurations of constituents of arterial tissue.

In composite models including the heterogeneous model, proposed in this study, the SEF of arterial tissue was decoupled into the SEFs of elastin and collagen fibers. More experimental data are needed to refine the SEF of each vascular component. Also, the development of new experimental methods will help better understanding of vascular mechanics.

Although the distributions of stresses and structural components observed in this study may not be applicable to other types of arteries, the methodology developed will be applicable in general. It is known that the composition of structural proteins vary along the arterial tree. The heterogeneity of microstructure is also expected to change in different types of arteries. Applying the methods developed to various types of arteries will improve the understanding of physiology and pathophysiology of particular type of arteries.

- *Explore biological makers for the measures of mechanosensitive responses of cells*

Many functions of cells, including the production of matrix proteins, have been shown to be mechanosensitive. The expression and activation of MMP-2 and MMP-9 is one of such functions related to vascular remodeling. To gain more insights into the vascular remodeling, it is important to understand the relationships between different functions of cells. Changes in mechanical environment often trigger a biological chain reaction, which ultimately affects the balance of biological products in arterial tissue. Thus, to isolate the effect of mechanical stimuli on the particular function of cells, experiments need to be carefully designed.

APPENDIX A

PROTOCOLS FOR EXPERIMENT AND HISTOLOGY

Solutions for Organ Culture Study

Phosphate Buffered Saline (PBS)

To make 1 L PBS:

1. 500 ml of deionized-distilled water
2. Add a bottle of Dulbecco's PBS (Sigma D-5773)
3. Add 10 ml Antibiotic-Antimycotic (Sigma P-0906)
4. Add deionized-distilled water to make 1 L
5. Sterilize by microfiltering (pore size: 0.2 μm)

Perfusion Medium

Solution A

1. Warm 400 ml deionized-distilled water
2. Add 63 g Dextran powder (Sigma, average molecular weight 170,000)
3. Add stir bar and mix

Solution B

1. 400 ml deionized-distilled water
2. Add 17.4 g Dulbecco's modified Eagle's medium (DMEM, Sigma D-1152)
3. Add 3.7 g sodium bicarbonate ($NaHCO_3$)
4. Add 10 ml Antibiotic-Antimycotic (Sigma P-0906)
5. Add 10 ml 200 mmol L-glutamine (Sigma)
6. Bring total volume to 500 ml with deionized-distilled water

To make 1 L perfusion medium

1. Mix solutions A and B
2. Adjust pH to 7.4
3. Sterilize by microfiltering (pore size: 0.2 μm)
4. Store 450 ml in each 500 ml bottle
5. Note: add 50 ml of calf serum (HyClone) before use

Bath Medium

To make 1 L bath medium

1. 700 ml deionized-distilled water
2. Add 17.4 g DMEM (Sigma D-1152)
3. Add 3.7 g sodium bicarbonate ($NaHCO_3$)
4. Add 10 ml Antibiotic-Antimycotic (Sigma D-0906)
5. Add 10 ml 200 mmol L-glutamine (Sigma)
6. Bring total volume to 900 ml with deionized-distilled water
7. Adjust pH to 7.4
8. Sterilize by microfiltering (pore size: 0.2 μm)
9. Store 450 ml in each 500 ml bottle
10. Note: add 50 ml of calf serum (HyClone) before use

Protocols for Histology

Immunohistochemistry for MMP-2 or MMP-9

Note: All antibodies and related reagents are temperature sensitive. Please keep at 4℃ or on ice at all times. This will maintain the longevity of the reagent and limit antibody or reagent related problems with experiments.

1. Frozen sections are thawed immediately before use at room temperature, between 10 – 30 minutes prior to start of the procedure. The frozen sections are fixed in acetone 5 min. and air dried 5 min.

2. Sections are washed in 1X PBS 5 min.
3. Block endogenous peroxidase using 0.3% H_2O_2 in methanol (or PBS) for 30 min. at room temperature. (dilute 2.0 ~ 2.5 ml of 30% H_2O_2 in 200 ~ 250 ml methanol or PBS) OR 0.3% H_2O_2 in 0.3% Normal Sera in PBS for 5 minutes. (2.0 ml of 30% H_2O_2 and 600 µl of Normal Sera in 200 ml PBS)
4. Rehydrate in 1X PBS twice for 5 min. each, room temp.
5. Block tissue using 10% normal serum in PBS for 20 min at room temperature.
6. Prepare the working dilution of primary antibody in PBS (50 µl 1st antibody + 950 µl PBS). Refer to previous work done with the antibody to determine working dilution or refer to spec. sheet of antibody for starting dilution (if using antibody for the first time you will need to run a series of dilutions to determine the optimal working concentration). Blot off blocking agent and apply primary antibody (~130 µl for each 7 sections). Incubate sections in a humid chamber for 1 h at room temperature.
7. Blot off excess antibody and wash slides in 1X PBS twice for 5 minutes each at room temperature. Prepare working dilution of the biotinylated secondary antibody in 1X PBS, and add 2% of normal serum from the source animal of the secondary antibody. (For 1000 µl, add 2.5 µl of 2nd antibody and 20 µl of normal serum to 1000-22.5 µl of PBS) Prepare secondary antibody at a 1/400 dilution. Apply and incubate 30 min, at room temperature in a humid chamber.
8. Prepare the working dilution of ABS-peroxidase complex from the Vector ABC-Peroxidase Elite Kit (#PK-6100) after application of secondary antibody. Mix 2.5 ml of 1X PBS, one drop of reagent A, and one drop of reagent B and allow to sit at 4 °C 30 minutes prior to use.
9. Blot off excess antibody and wash slides in 1X PBS twice for 5 min. each at room temperature.

10. Apply prepared ABC mixture to each slide. Incubate in a humid chamber for 1 h at room temperature.
11. Blot off excess solution and wash slides in 1X PBS twice for 5 minutes each.
12. Immediately before use, prepare the substrate solution as follows. To 5 ml of dH_2O, add 2 drops of Buffer Stock Solution and mix well. Add 4 drops of DAB Stock Solution and mix well. Add 2 drops of the Hydrogen Peroxidase Solution and mix well. If a gray-black stain is desired, add 2 drops of the Nickel Solution and mix well. Incubate tissue sections with the substrate at room temperature until suitable staining develops Development times should be determined by the investigator but generally 2-10 minutes provides good staining intensity. Wash the sections for 5 minutes in water
13. If needed, lightly counterstain sections with haematoxylin.

In Situ Zymography

Materials

- Fluorescent substrate (1 mg/ml): Solutions can be made by dissolving the lyophilized gelatin from pig skin, Oregon Green® 488 conjugate (G-13198, Molecular Probe) in 5 ml dH_2O to give 1 mg/ml solutions in PBS. The gelatin substrates may require sonication and heating to 50°C to aid dissolution. Store solution at 4°C with the addition of sodium azide at a final concentration of 2 mM. For long-term storage, divide solutions into aliquots and freeze at -20°C. (500 µl aliquot)
- Tris buffer (100 ml): Tris-HCl (50 mM, pH 7.4, 0.788 g) containing 10 mM Ca chloride (0.111 g) and 0.05% Brij 35 (167 µl).
- 1% agarose melted in Tris buffer: Dissolve 0.05 g of agarose (Sigma, A-0701: Type VII-A: Low Gelling Temperature) in 5 ml Tris buffer at 65°C.

Procedure

1. Lower temperature to 50°C.
2. Mix (1:1, 500 μl: 500 μl) Fluorescent substrate (1 mg/ml) with 1% agarose melted in Tris buffer.
3. Spread the liquid mixture (about 10 μl) on prewarmed (max heat on slide heater) glass slides by a maneuver similar to that used to produce blood smears.
4. Allow the film to gel at room temperature and inspect with microscope.
5. Discard slides with nonhomogeneous-appearing substrate layers.
6. Cut frozen sections (6 – 10 μm) of unfixed tissue and apply them on top of the substrate film.
7. Add a drop of the Tris buffer over each tissue section and place a coverslip on top.
8. Incubate slides in a horizontal position, light-protected, in humidified chambers at 37°C for various length of time.
9. Examine lysis of the substrate under fluorescent microscope with an FITC filter.

Direct Red (picrosirius red) Detection of Collagen in Vascular Tissue

1. Deparaffinize and rehydrate paraffin embedded sections
2. Sections are then stained for 75 minutes in a solution of 0.1% Direct Red (Sirius red F3B, Sigma-Aldrich) in saturated picric acid solution.
3. Wash slide in 0.5% acetic acid in dH_2O for 5 minutes
4. Wash slide in dH_2O for 5 minutes.
5. Dehydrate slides in ascending grade alcohol, and xylene.
6. Apply a drop of Permount and coverslip.

Hoechst Nucleus Staining

1. Fixed paraffin embedded tissue is deparaffinized, and rehydrated in descending grades of alcohol (using regular protocol). Sections are washed in dH_2O for 5 minutes.
2. Stain with Hoechst 33258 (bis-benzamide, Molecular Probe) 1 μg/ml (Stock solution is 10 μg/ml) for 30 minutes under dark condition.
3. Wash twice in PBS for 5 min each.
4. Coverslip using fluorescent mount medium (Fluoromount)
5. Store in dark box at 4°C.

APPENDIX B

MATLAB CODE

Quantification of MMP-2, MMP-9, Elastin, and Collagen

Trace the Inner and Outer Boundaries of the Media (trace_boundary.m)

```
% trace_boundary.m
% This program reads an image file
%   Masked image of MMP-2 immunostaining
%   Masked image of MMP-9 immunostaining
%   Masked image of in situ zymography
%   image of elastin
%   superimposed image of collagen fibers
% and traces the inner and outer boundaries of arterial sector
% according to control point selection by user

% Slide ID of image origin
slidenum='(YK7-1-1b)';
% Image ID indicating it is a part of arterial ring
datanum='19';
% File Name of the image
filename=[slidenum ' FITC' datanum '.jpg'];

% This program is currently set for elastin
elastin=imread(filename);
% Display original image
figure(3);
imagesc(elastin);
colormap(gray);

hold on

% IEL tracing

% Initially, the list of points is empty.
xy = [];
% Interpolation spacing vector
ts = [];
% IEL boundary point cloud matrix
IEL = [];
```

```
n = 0;
% Loop, picking up the points.
disp('Pick points on IEL');
disp('Left mouse button picks points.');
disp('Right mouse button picks last point.');
but = 1;
while but == 1
   [xi,yi,but] = ginput(1);
   plot(xi,yi,'bo')
   n = n+1;
   xy(:,n) = [xi;yi];

   if (n>1)
      % Interpolate with a spline curve and finer spacing.
      d = round(sqrt((xy(1,n)-xy(1,n-1))^2+(xy(2,n)-xy(2,n-1))^2));
      ts=[ts,n-1:(1/d):n];
   end
end

t = 1:n;
IEL = spline(t,xy,ts);
% Plot the interpolated curve.
plot(IEL(1,:),IEL(2,:),'b.');

% EEL tracing

% Initially, the list of points is empty.
xy = [];
% Interpolation spacing vector
ts = [];
% IEL boundary point cloud matrix
EEL = [];
n = 0;
% Loop, picking up the points.
disp('Pick points on EEL');
disp('Left mouse button picks points.');
disp('Right mouse button picks last point.');
but = 1;
while but == 1
   [xi,yi,but] = ginput(1);
   plot(xi,yi,'ro')
   n = n+1;
   xy(:,n) = [xi;yi];

   if (n>1)
      % Interpolate with a spline curve and finer spacing.
```

```
      d = round(sqrt((xy(1,n)-xy(1,n-1))^2+(xy(2,n)-xy(2,n-1))^2));
      ts=[ts,n-1:(1/d):n];
   end
end

t = 1:n;
EEL = spline(t,xy,ts);
% Plot the interpolated curve.
plot(EEL(1,:),EEL(2,:),'r.');
hold off

% Store boundary tracing points
tracefile=[slidenum ' Boundary tracing ' datanum '.mat'];
save(tracefile,'IEL','EEL');
```

Quantify the Distribution of Measurement (e.g. elastin_distribution.m)

```
% elastin_distribution.m
% This program reads Elastin image and Boundary points cloud
% Generate elastin distribution between IEL and EEL

% clear memory
clear

% Slide ID
slidenum='(YK7-1-1b)';
% Images constitutes whole arterial ring
series_datanum=[1 2 3 4 5 6 7 8 9 10 11 12 13 14 15 16 17 18 19];
temp=size(series_datanum);
series_size=temp(2);

for i=1:series_size
datanum=num2str(series_datanum(i),'%02u');
filename=[slidenum ' FITC' datanum '.jpg'];
% Name of output file
distfile=[slidenum ' Elastin Distribution ' datanum '.mat'];
% variable for average pixel intensity of each layer
% total 51 layer
eldist=zeros(51,2);
% read the image of a sector
elastin=imread(filename);

% display elastin image
figure(4);
imagesc(elastin);
colormap(gray);
```

```
% Read Boundary Tracing Pts Cloud
tracefile=[slidenum ' Boundary tracing ' datanum '.mat'];
load(tracefile,'IEL','EEL');

% hold on
[maxy, maxx]=size(elastin);

h = waitbar(0,'DATA is on its way...');

% each pixel is mapped onto circular ring
% by computing shortest distances to the inner and outer boundaries
% by computing the transmural location, the layer number is determined
% update the average pixel intensity of the layer

for xx=1:1:maxx
   for yy=1:1:maxy
      % shortest distance between current point and IEL
      dist1=sqrt((IEL(1,:)-xx).^2+(IEL(2,:)-yy).^2);
      [d1,ii]=min(dist1);
      % The line through (x1,y1) and (x2,y2) is given by the two point
      % form y-y1=(y2-y1)/(x2-x1)*(x-x1)
      % current point (xx,yy), IEL point (xi,yi)
      xi=IEL(1,ii);
      yi=IEL(2,ii);
      if (round(d1)>0)  % if current point is NOT on IEL
         dist2=abs((xx-xi)*(yi-EEL(2,:))-(xi-EEL(1,:))*(yy-yi))/d1;
         [dd,ee]=min(dist2);
         if (round(dd)==0)
            xo=EEL(1,ee);
            yo=EEL(2,ee);
            d2=sqrt((xo-xx)^2+(yo-yy)^2);
            thickness=sqrt((xo-xi)^2+(yo-yi)^2);
            if (round(thickness)==round(d1+d2))
               % plot(xx,yy,'y.');
               layer=ceil(d1/thickness*50);
               eldist(layer,1)=eldist(layer,1)+1;
               eldist(layer,2)=eldist(layer,2)*(eldist(layer,1)-
1)/eldist(layer,1)+(double(elastin(yy,xx))+1)/eldist(layer,1);
            end
         end
      end
   end
   waitbar(xx/maxx);
end
xx
```

```
close(h);
save(distfile,'eldist');
distfile
% hold off
end
```

Quantification of VSMC Nuclear Geometry

Projection of Three-Dimensional Data on the Imaging Plane (SMC2DProj.m)

```
% SMC2DProj.m
% Generate 2D projection of 3D z-stack onto the xy plane

%% User NEEDS to assign following variables

% Slide ID
slidenum='(YK7-3-19) 40x 02-1';
% the number of optical sections
zstack_num=29;
% Threshold value for binary image
threshold=0.60;
h=ones(5,5)/25;

% Threshold, Smoothen and Restack optical sections

for i=1:zstack_num
   imagenum=num2str(i-1,'%03d');
   filename=[slidenum imagenum '.jpg'];
   % Read original image
   optical_section=imread(filename);
   % smoothing
   I2 = imfilter(optical_section,h,'replicate');
   % Covert to binary image
   bw_image=im2bw(I2, threshold);

  % Stack the processed images of optical sections
   zstack(:,:,i)=bw_image(:,:);
end
% the size of z stack in Y-direction
yy=size(zstack,1);
% the size of z stack in X-direction
xx=size(zstack,2);
all_projection=zeros(yy,xx);
for j=1:zstack_num
   all_projection=all_projection|zstack(:,:,j);
```

```
end

imshow(all_projection);
savefilename=[slidenum ' 2D.jpg'];
imwrite(all_projection,savefilename,'jpg');
```

Identify VSMC Nuclei (smc_select.m)

```
% smc_select.m
% This program visualize confocal microscopy data in 2D and 3D spaces
% and help user to select smooth muscle cell nuclei
%
% Created on 2003-11-07 by Yu Shin Kim
% last revised on 09/05/2006

clear

%% User NEEDS to assign following variables

% Slide ID
slidenum='(YK7-3-19) 40x 02-1';
% the number of optical sections
zstack_num=29;
% Conversion factor for x and y dimension
xy_dim=0.45;
% Conversion factor for z dimension
z_spacing=0.79;
%% END of user input

% Threshold value for binary image
threshold=0.45;
h=ones(3,3)/9;

% Threshold, Smoothen and Restack optical sections
for i=1:zstack_num
   imagenum=num2str(i-1,'%03d');
   filename=[slidenum imagenum '.jpg'];
   % Read original image
   optical_section=imread(filename);

   % smoothing
   I2 = imfilter(optical_section,h,'replicate');
   zstack1(:,:,i)=I2;

end
```

```
% Basic variables for visualization

% the size of z stack in Y-direction
yy=size(zstack1,1);
% the size of z stack in X-direction
xx=size(zstack1,2);
% The aspect ratio of z-direction with respect to x and y pixel dimension
aspect_ratio_z=xy_dim/z_spacing;

% smoothing on YZ plane
for i=1:xx
   opt_sec(:,:)=zstack1(i,:,:);
   I4 = imfilter(opt_sec,h,'replicate');
   zstack2(i,:,:)=I4;
end
% smoothing on XZ plane
for i=1:yy
   opt_sec(:,:)=zstack2(:,i,:);
   I3 = imfilter(opt_sec,h,'replicate');
   zstack3(:,i,:)=I3;
end
% thresholding
for i=1:zstack_num
   opt_sec1(:,:)=zstack3(:,:,i);
   bw2=im2bw(opt_sec1, threshold);
   zstack4(:,:,i)=bw2(:,:);
end

% erode
se=[1 1 1 1 1];
for i=1:xx
   opt_sec2(:,:)=zstack4(i,:,:);
   I4 = imerode(opt_sec2,se);
   zstack(i,:,:)=I4;
end


% Label connected components in 3D binary image
% L, a label matrix, contains labels for the connected components
% 26-connected neighborhood is used for connectivity test in 3D
[L,objectnum]=bwlabeln(zstack,26);

objectnum

% Acquire the number of voxels in each object
```

```
stats=regionprops(L,'Area');
% Filter objects with less than 500 voxels
for i=1:1:objectnum
   if stats(i).Area<500
      zstack=zstack-ismember(L,i);
   end
end

% Label connected components in filtered z-stack
[L,objectnum]=bwlabeln(zstack,26);
objectnum

% The 2D projection of z-stack to imaging plane
all_projection=zeros(yy,xx);
for j=1:zstack_num
   all_projection=all_projection|zstack(:,:,j);
end
% Set the color of objects gray (0.5)
all_projection=all_projection/2;

% the number of selected SMC nuclei
smc_count=0;
smc_list=[];
% Counter
i=1;

while (i<=objectnum)

 % Select ith object
   ith_object=ismember(L,i);

 % Show a projection of the object on 2D surface
   projection=zeros(yy,xx);
   for j=1:zstack_num
      projection=projection|ith_object(:,:,j);
   end
   projection=projection/2;
 % Selected object will appear as white, otherwise gray.
   projection=projection+all_projection;

   figure(1);
   clf;
   % Cartesian coordinate
   axis xy;
   hold on;
   imshow(projection);
```

```
  % 3D visualization of selected object.
    figure(2);
    clf;
    p=patch(isosurface(ith_object,0.5),'FaceColor','blue','EdgeColor','none');
    view(60,35);
  % the data aspect ratio in the current axes
    daspect([1 1 aspect_ratio_z]);
    xlabel('x');
    ylabel('y');
    zlabel('z');
    camlight;
    lighting gouraud;

  % Identify object type
    i  % counter display
    selection=input('SMC Nuclei (1) Noise (2) Go back (3):');
    if selection==1
       disp('included')
       smc_count=smc_count+1;
       smc_list(smc_count)=i;
    end
    i=i+1;
    if ((selection==3) & (i>2))
       i=i-2;
       if smc_list(smc_count)==i
          smc_count=smc_count-1;
       end
    end
end
disp('The number of SMC nuclei selected')
smc_count

datafile=[slidenum '.mat'];
save(datafile,'L','objectnum','smc_count','smc_list');
```

Quantify VSMC Nuclear Geometry in Terms of the Imaging Coordinate System

(smc_measure.m)

```
% smcmeasure.m
% Measure the dimensional characteristics of selected objects (SMC nuclei)
% Created on 11/13/2003 by Yu Shin Kim
% Last revised on 11/19/2003
```

```
% conversion (1 x 3)
%   The conversion factors from one voxel unit to micrometer
% voxel_list (n x 3)
%   The location (x,y,z) of n voxels in voxel unit (1)
% voxel_num (scalar)
%   The number of voxels in each object
% voxel_coordinate (n x 3)
%   The physical location (x,y,z) of n voxels in micrometer
% centroid_obj (1 x 3)
%   The centroid of each object in voxel space
% centroid_coordinate (1 x 3)
%   The physical location (x,y,z) of centroid
% centroid_to_voxel (n x 1)
%   The vectors from the centroid and n voxels in micrometer
% eigen_vector (3 x 3)
%   Three column vectors from minor axis to major axis.
% length (3 x 2)
%   The length of object along principal axes from minor to major one.
%   ith row corresponds to ith eigen vector
%   1st column is in the positive direction, 2nd is in the negative direction.
%
%

clear

%% User NEEDS to assign following variables

% Slide ID
slidenum='(YK7-3-19) 40x 02-1';
% Conversion factor for x and y dimension
xy_dim=0.45;
% Conversion factor for z dimension
z_spacing=0.79;

%% END of user input

% Conversion vector
conversion=[xy_dim xy_dim z_spacing];
% The aspect ratio of z-direction with respect to x and y pixel dimension
% for 3D visualization in voxel space
aspect_ratio_z=xy_dim/z_spacing;

% retrieve data from selection process
datafile=[slidenum '.mat'];
load(datafile,'L','objectnum','smc_count','smc_list');
```

```
% define new variables
smc_count_measured=0;
smc_list_measured=[];

% Get basic object properties
% Centroid of each object, The list of voxels in each object
stats=regionprops(L,'Centroid','PixelList');

% counter: sequential number of selected SMC nuclei
i=1;
while (i<=smc_count)

   % The label of selected object in the label matrix L
   object_id=smc_list(i);

   % List of the locations of the voxels in the object
   voxel_list=stats(object_id).PixelList;
   % The number of voxels in the object
   voxel_num=size(voxel_list,1);
   % Calculate physical locations of each voxel
   voxel_coordinate=voxel_list.*(ones(voxel_num,1)*conversion);

   centroid_obj=stats(object_id).Centroid;
   % Calculate physical location of the centroid (physical coord)
   centroid_coordinate=centroid_obj.*conversion;

   % The vectors from the centroid and each voxel (physical coord)
   centroid_to_voxel=voxel_coordinate-ones(voxel_num,1)*centroid_coordinate;

   % Covariance matrix S
   S=cov(voxel_coordinate);

   % Find eigenvalues (D) and eigenvectors (eigen_vector)
   % Matrix eigen_vector is the modal matrix - its columns are the eigenvectors of S.
   [eigen_vector,D]=eig(S);

   % Find two points with max distance from centroid in (+) and (-) directions
   % Max length matrix ixj - ith eigenvector x (+)(-) direction
   length=zeros(3,2);
   x1=zeros(3,2);
   y1=zeros(3,2);
   z1=zeros(3,2);

   for ii=1:3
     % maximum length in the positive direction of principal vector
      length(ii,1)=max(centroid_to_voxel*eigen_vector(:,ii));
```

```
  % maximum length in the negative direction of principal vector
    length(ii,2)=min(centroid_to_voxel*eigen_vector(:,ii));
  % coordinates for principal axes visualization
    x1(ii,:)=eigen_vector(1,ii)*2*length(ii,:)+centroid_coordinate(1);
    y1(ii,:)=eigen_vector(2,ii)*2*length(ii,:)+centroid_coordinate(2);
    z1(ii,:)=eigen_vector(3,ii)*2*length(ii,:)+centroid_coordinate(3);
end

% 3D visualization of the principal axes in real coordinate system

figure(3);
clf;
hold on
plot3(x1(1,:),y1(1,:),z1(1,:),'-om','LineWidth',2,'MarkerSize',10);
plot3(x1(2,:),y1(2,:),z1(2,:),'-or','LineWidth',2,'MarkerSize',10);
plot3(x1(3,:),y1(3,:),z1(3,:),'-og','LineWidth',2,'MarkerSize',10);
view(60,35);
% the data aspect ratio in the current axes
daspect([1 1 1]);
xlabel('X');
ylabel('Y');
zlabel('Z');

% 3D visualization of selected object and principal axes in voxel space.
% conversion back to voxel unit
inv_conv=1./conversion;

eigen_vector2=eigen_vector.*(inv_conv'*ones(1,3));
magnitude=sqrt(sum(eigen_vector2.^2));

% Normalize V2
eigen_vector2=eigen_vector2(:,:)./(ones(3,1)*magnitude);
% Convert length from micrometer to voxel unit
length2=length.*(magnitude'*ones(1,2));

for ii=1:3
   x1(ii,:)=eigen_vector2(1,ii)*2*length2(ii,:)+centroid_obj(1);
   y1(ii,:)=eigen_vector2(2,ii)*2*length2(ii,:)+centroid_obj(2);
   z1(ii,:)=eigen_vector2(3,ii)*2*length2(ii,:)+centroid_obj(3);
end

object3D=ismember(L,object_id);
figure(4);
clf;
hold on
p=patch(isosurface(object3D,0.5),'FaceColor','blue','EdgeColor','none');
```

```
    plot3(x1(1,:),y1(1,:),z1(1,:),'-om','LineWidth',2,'MarkerSize',10);
    plot3(x1(2,:),y1(2,:),z1(2,:),'-or','LineWidth',2,'MarkerSize',10);
    plot3(x1(3,:),y1(3,:),z1(3,:),'-og','LineWidth',2,'MarkerSize',10);
    view(60,35);
    % the data aspect ratio in the current axes
    daspect([1 1 aspect_ratio_z]);
    xlabel('x');
    ylabel('y');
    zlabel('z');
    camlight;
    lighting gouraud;

% Check normality
sqrt(sum(eigen_vector.^2))
    % Decide the final acceptance of the object
    smc_list(i)
    selection=input('Accept (1) Decline (2) Quit(3):');
    if selection==1
        disp('included')
        smc_count_measured=smc_count_measured+1;
        smc_list_measured(smc_count_measured)=smc_list(i);

        principal_direction(:,:,smc_count_measured)=eigen_vector;

        principal_length(:,:,smc_count_measured)=length;
        centroid(smc_count_measured,:)=centroid_coordinate;
      % volume (converted to micrometer^3)
        volume(smc_count_measured)=voxel_num*(xy_dim^2)*z_spacing;
    end

    if selection==3
        i=smc_count;
    end
i=i+1
end
% angle between major axis and xy-plane
angle=90-rad2deg(acos(principal_direction(3,3,:)));
% length along major axis
ll=principal_length(3,1,:)-principal_length(3,2,:);

datafile=[slidenum 'measure.mat'];
% physical dimensions
save(datafile,'L','smc_count_measured','smc_list_measured','principal_direction','principa
l_length','centroid','volume');
```

Trace the Inner and Outer Boundaries of the Media (boundary_trace.m)

```
% boundary_trace.m
%
% Due to the small window of view (512 x 512 pixel, 0.45 micron/pxl)
% Three or Four images were taken to cover the thickness of arterial sector
% Since the angle is small, boundaries can be approximated as lines
% Boundary line equation (first-order approximation)
% IEL and Media-EEL boundary line equation

clear

% load lumen-side 2D projected image
image1=imread('(YK7-3-19) 40x 02-1 2D.jpg');
% load outer layer-side 2D projected image
image3=imread('(YK7-3-19) 40x 02-3 2D.jpg');

% display lumen-side image
bw1=im2bw(image1,0.5);
bw3=im2bw(image3,0.5);

figure(1);
imagesc(bw1);
colormap(gray);
hold on

xy_dimension=0.45;
n=0;
A=[];
b=[];

% Label objects and retrieve object property
[L1,Num1]=bwlabeln(bw1,8);
stats1=regionprops(L1,'Centroid');

% Plot Centroid locations
for i=1:Num1
   temp=stats1(i).Centroid;
   x=temp(1);
   y=temp(2);
   plot(x,y,'ro')
end

but=1;
while but == 1
   [xi,yi,but]=ginput(1);
```

```
    xx=round(xi);
    yy=round(yi);
    obj=L1(yy,xx);

    if obj ~= 0
        xy=stats1(obj).Centroid;
        n=n+1;
        plot(xy(1),xy(2),'bo')
        % Physical Coordinate
        A(n,:)=xy*xy_dimension;
        b(n,1)=-1;
    end
end

% c1 X + c2 Y + 1 = 0: c=[c1 c2]
c=A\b
% normalization: Ci(1)X+Ci(2)Y+Ci(3)=0 in physical coordinate
Ci = [c(1)/norm(c) c(2)/norm(c) 1/norm(c)]

hold off

load('2D_alignment.mat','uxy12','uxy23');

% display outer-side image
figure(2);
imagesc(bw3);
colormap(gray);
hold on

xy_dimension=0.45;
n=0;
A3=[];
b3=[];

% Label objects and retrieve object property
[L3,Num3]=bwlabeln(bw3,8);
stats3=regionprops(L3,'Centroid');

% Plot Centroid locations
for i=1:Num3
    temp=stats3(i).Centroid;
    x=temp(1);
    y=temp(2);
    plot(x,y,'ro')
end
```

```
but=1;
while but == 1
   [xi,yi,but]=ginput(1);
   xx=round(xi);
   yy=round(yi);
   obj=L3(yy,xx);

   if obj ~= 0
      xy=stats3(obj).Centroid;
      n=n+1;
      plot(xy(1),xy(2),'bo')
      A3(n,1)=xy(1)*xy_dimension+uxy12(1)+uxy23(1);  % Physical Coordinate
      A3(n,2)=xy(2)*xy_dimension+uxy12(2)+uxy23(2);  % Physical Coordinate
      b3(n,1)=-1;
   end
end

% c1 X + c2 Y + 1 = 0: c=[c1 c2]
c=A3\b3
% normalization: Ci(1)X+Ci(2)Y+Ci(3)=0 in physical coordinate
Co = [c(1)/norm(c) c(2)/norm(c) 1/norm(c)]

hold off

% Check plot
figure(3);
hold on
% Plot Centroid locations
for i=1:Num1
   temp=stats1(i).Centroid;
   x=temp(1)*xy_dimension;
   y=temp(2)*xy_dimension;
   plot(x,y,'ro')
end
for i=1:Num3
   temp=stats3(i).Centroid;
   x=temp(1)*xy_dimension+uxy12(1)+uxy23(1);
   y=temp(2)*xy_dimension+uxy12(2)+uxy23(2);
   plot(x,y,'go')
end

p(1)=-Ci(1)/Ci(2);
p(2)=-Ci(3)/Ci(2);
f=polyval(p,A(:,1));
plot(A(:,1),f,'r-')
```

```
p(1)=-Co(1)/Co(2);
p(2)=-Co(3)/Co(2);
f=polyval(p,A3(:,1));
plot(A3(:,1),f,'g-')

hold off

save('boundaries.mat','Ci','Co','A','A3');
```

Align *Z*-Stacks through the Thickness (image_alignment.m)

```
% image_alignment.m
%
% To compute the intramural location of each VSMC nucleus
% Images of inner, middle, and outer media need to be aligned
% This program
% determines relative locations of images 1, 2, and 3
% 1-lumen to inner media, 2-mid region, 3-outer media to EEL

clear

image1=imread('(YK7-3-19) 40x 02-1 2D.jpg');
image2=imread('(YK7-3-19) 40x 02-2 2D.jpg');
image3=imread('(YK7-3-19) 40x 02-3 2D.jpg');

xy_dimension=0.45;

bw1=im2bw(image1,0.5);
bw2=im2bw(image2,0.5);
bw3=im2bw(image3,0.5);

figure(1);
imagesc(bw1);
colormap(gray);
figure(2);
imagesc(bw2);
colormap(gray);
figure(3);
imagesc(bw3);
colormap(gray);

% retrive center location of objects in each image
[L1,Num1]=bwlabel(bw1,8);
[L2,Num2]=bwlabel(bw2,8);
[L3,Num3]=bwlabel(bw3,8);
```

```
stats1=regionprops(L1,'Centroid');
stats2=regionprops(L2,'Centroid');
stats3=regionprops(L3,'Centroid');

% Plot SMC centroids

figure(1)
hold on
for i=1:Num1
   temp=stats1(i).Centroid;
   x=temp(1);
   y=temp(2);
   plot(x,y,'ro')
end
hold off
figure(2)
hold on
for i=1:Num2
   temp=stats2(i).Centroid;
   x=temp(1);
   y=temp(2);
   plot(x,y,'ro')
end
hold off
figure(3)
hold on
for i=1:Num3
   temp=stats3(i).Centroid;
   x=temp(1);
   y=temp(2);
   plot(x,y,'ro')
end
hold off

% alignment matrix
totaltemp=zeros(1,2);
% alignment between image 1 and 2 (compare 3 object pairs)
for i=1:3
   disp('pick the object on figure 1 which will aligned to object on figure 2');
   figure(1)
   hold on
   [xi,yi]=ginput(1);
   x=round(xi);
   y=round(yi);
   obj=L1(y,x)
   temp1=stats1(obj).Centroid;
```

```
    plot(temp1(1),temp1(2),'bo')
    hold off

    disp('pick the object on figure 2 which will aligned to object on figure 1');
    figure(2)
    hold on
    [xi,yi]=ginput(1);
    x=round(xi);
    y=round(yi);
    obj=L2(y,x)
    temp2=stats2(obj).Centroid;
    plot(temp2(1),temp2(2),'bo')
    hold off

    uxytemp=temp1-temp2
    totaltemp=totaltemp+uxytemp
end
uxy12=totaltemp/3*xy_dimension

totaltemp=zeros(1,2);
% alignment between image 2 and 3 (compare 3 object pairs)
for i=1:3
    disp('pick the object on figure 2 which will aligned to object on figure 3');
    figure(2)
    hold on
    [xi,yi]=ginput(1);
    x=round(xi);
    y=round(yi);
    obj=L2(y,x)
    temp2=stats2(obj).Centroid;
    plot(temp2(1),temp2(2),'bo')
    hold off

    disp('pick the object on figure 3 which will aligned to object on figure 2');
    figure(3)
    hold on
    [xi,yi]=ginput(1);
    x=round(xi);
    y=round(yi);
    obj=L3(y,x)
    temp3=stats3(obj).Centroid;
    plot(temp3(1),temp3(2),'bo')
    hold off

    uxytemp=temp2-temp3
    totaltemp=totaltemp+uxytemp
```

```
end
uxy23=totaltemp/3*xy_dimension

% Check plot
figure(4);
clf
hold on
for i=1:Num1
   temp=stats1(i).Centroid;
   x=temp(1);
   y=temp(2);
   plot(x,y,'ro')
end
for i=1:Num2
   temp=stats2(i).Centroid;
   x=temp(1)+uxy12(1)/xy_dimension;
   y=temp(2)+uxy12(2)/xy_dimension;
   plot(x,y,'bo')
end
for i=1:Num3
   temp=stats3(i).Centroid;
   x=temp(1)+uxy12(1)/xy_dimension+uxy23(1)/xy_dimension;
   y=temp(2)+uxy12(2)/xy_dimension+uxy23(2)/xy_dimension;
   plot(x,y,'go')
end
hold off

save('2D_alignment.mat','uxy12','uxy23');
```

Quantify the Distribution of VSMC Nuclear Geometry in Terms of the Local Coordinate System (distribution.m)

```
% distribution.m
% this program quantifies distributions of VSMC geometry
%
% Measure intramural location of each SMC nuclei
% Measure relative orientation of SMC in reference to lumen

clear
slidenum='(YK7-3-19) 40x 02';

datafile=[slidenum '-1measure.mat'];
load(datafile);
```

```
load('2D_alignment.mat','uxy12','uxy23');
load('boundaries.mat','Ci','Co','A','A3');

center_x=[];
center_y=[];

major_length=[];
major_2D_length=[];
% Using projection angle onto r-theta
major_2D_length2=[];
% Using projection angle onto theta-z
major_2D_length3=[];
 % Projection angle onto r-theta plane
proj_angle_rt=[];
% Projection angle onto theta-z plane
proj_angle_tz=[];
relative_angle=[];
intramural_loc=[];
helical_angle=[];
counter=0

figure(1);
hold on

p(1)=-Ci(1)/Ci(2);
p(2)=-Ci(3)/Ci(2);
f=polyval(p,A(:,1));
plot(A(:,1),f,'r-')

p(1)=-Co(1)/Co(2);
p(2)=-Co(3)/Co(2);
f=polyval(p,A3(:,1));
plot(A3(:,1),f,'g-')

lumen_o=[Ci(2) -Ci(1)];
direction=lumen_o/norm(lumen_o);
% Orient Ref direction CCW: positive
if direction(1)<0
   direction = -direction;
end
% Radial outward vector: positive
direction_r = [-direction(2) direction(1)];

% unit vector r in xyz-coordinate sys
tr=[direction_r 0];
% unit vector theta in xyz-coordinate sys
```

```
tt=[direction 0];
% unit vector z in xyz-coordinate sys
tz=[0 0 -1];

% transformation matrix from xyz to r-theta-z sys.
trans=[tr;tt;tz];

stats=regionprops(L,'Centroid','PixelList');

for i=1:smc_count_measured
   counter=counter+1

   center=centroid(i,:);
   x0=center(1);
   y0=center(2);

   center_x(counter)=x0;
   center_y(counter)=y0;

   % intersection on inner boundary
   c3=Ci(1)*y0-Ci(2)*x0;
   Ai=[Ci(1) Ci(2); Ci(2) -Ci(1)];
   bi=[-Ci(3); -c3];
   xy1=Ai\bi;
   % intersection on outer boundary
   Ao=[Co(1) Co(2); Ci(2) -Ci(1)];
   bo=[-Co(3); -c3];
   xy2=Ao\bo;
   % Intramural location
   d1=sqrt((x0-xy1(1))^2+(y0-xy1(2))^2);
   d2=sqrt((x0-xy2(1))^2+(y0-xy2(2))^2);
   intramural_loc(counter)=d1/(d1+d2);

   plot(x0,y0,'ro')
   plot([xy1(1) xy2(1)],[xy1(2) xy2(2)],'r-')

   % relative orientation & helical orientation

   % Coordinate Transformation
   smc_xyz=[principal_direction(:,3,i)];
   % long axis orientation in rtz coord
   smc_rtz=trans*smc_xyz;
norm(smc_rtz)

   % set orientation on positive theta direction
   if smc_rtz(2)<0
```

```
    smc_rtz = -smc_rtz;
  end
  % projection onto r-theta plane
  smc_rt=[smc_rtz(1);smc_rtz(2)];
  % projection angle onto r-theta plane
  proj_angle_rt(counter) = acos(norm(smc_rt));
  % normalize projected vector
  smc_rt_n=smc_rt/norm(smc_rt);

  % projection onto theta-z plane
  smc_tz=[smc_rtz(2);smc_rtz(3)];
  % projection angle onto theta-z plane
  proj_angle_tz(counter) = acos(norm(smc_tz));
  % normalize projected vector
  smc_tz_n=smc_tz/norm(smc_tz);

  % relative angle
  relative_angle(counter)=90-(acos(smc_rt_n(1)))*180/pi;

  % helical angle (REF: z-vector out of screen is positive)
  helical_angle(counter)=90-(acos(smc_tz_n(2)))*180/pi;

  % length of major axis
  major_length(counter)=principal_length(3,1,i)-principal_length(3,2,i);

  % length of 2D projected major axis
  centroid_obj=stats(smc_list_measured(i)).Centroid;
  voxel_list=stats(smc_list_measured(i)).PixelList;
  center_2D=centroid(1:2);
  pixel_list=voxel_list(:,1:2);

  pixel_num=size(pixel_list,1);
  ctr_to_pxl=pixel_list-ones(pixel_num,1)*center_2D;

  major_2D_length(counter)=0.45*(max(ctr_to_pxl*direction')-
min(ctr_to_pxl*direction'));

major_2D_length2(counter)=major_length(counter)*cos(relative_angle(counter)/180*pi)
*cos(proj_angle_rt(counter));

major_2D_length3(counter)=major_length(counter)*cos(helical_angle(counter)/180*pi)*
cos(proj_angle_tz(counter));
end

datafile=[slidenum '-2measure.mat'];
load(datafile);
```

```
stats=regionprops(L,'Centroid','PixelList');
for i=1:smc_count_measured
   counter=counter+1

   center=centroid(i,:);
   x0=center(1)+uxy12(1);
   y0=center(2)+uxy12(2);

   center_x(counter)=x0;
   center_y(counter)=y0;

   % intersection on inner boundary
   c3=Ci(1)*y0-Ci(2)*x0;
   Ai=[Ci(1) Ci(2); Ci(2) -Ci(1)];
   bi=[-Ci(3); -c3];
   xy1=Ai\bi;
   % intersection on outer boundary
   Ao=[Co(1) Co(2); Ci(2) -Ci(1)];
   bo=[-Co(3); -c3];
   xy2=Ao\bo;
   % Intramural location
   d1=sqrt((x0-xy1(1))^2+(y0-xy1(2))^2);
   d2=sqrt((x0-xy2(1))^2+(y0-xy2(2))^2);
   intramural_loc(counter)=d1/(d1+d2);

   plot(x0,y0,'bo')
   plot([xy1(1) xy2(1)],[xy1(2) xy2(2)],'b-')

   % relative orientation & helical orientation

   % Coordinate Transformation
   smc_xyz=[principal_direction(:,3,i)];
    % long axis orientation in rtz coord
   smc_rtz=trans*smc_xyz;
norm(smc_rtz)
   % set orientation on positive theta direction
   if smc_rtz(2)<0
      smc_rtz = -smc_rtz;
   end
   % projection onto r-theta plane
   smc_rt=[smc_rtz(1);smc_rtz(2)];
   % projection angle onto r-theta plane
   proj_angle_rt(counter) = acos(norm(smc_rt));
   % normalize projected vector
   smc_rt_n=smc_rt/norm(smc_rt);
```

```
    % projection onto theta-z plane
    smc_tz=[smc_rtz(2);smc_rtz(3)];
    % projection angle onto theta-z plane
    proj_angle_tz(counter) = acos(norm(smc_tz));
    % normalize projected vector
    smc_tz_n=smc_tz/norm(smc_tz);

    % relative angle
    relative_angle(counter)=90-(acos(smc_rt_n(1)))*180/pi;

    % helical angle (REF: z-vector out of screen is positive)
    helical_angle(counter)=90-(acos(smc_tz_n(2)))*180/pi;

    % length of major axis
    major_length(counter)=principal_length(3,1,i)-principal_length(3,2,i);

    % length of 2D projected major axis
    centroid_obj=stats(smc_list_measured(i)).Centroid;
    voxel_list=stats(smc_list_measured(i)).PixelList;
    center_2D=centroid(1:2);
    pixel_list=voxel_list(:,1:2);

    pixel_num=size(pixel_list,1);
    ctr_to_pxl=pixel_list-ones(pixel_num,1)*center_2D;

    major_2D_length(counter)=0.45*(max(ctr_to_pxl*direction')-
min(ctr_to_pxl*direction'));

major_2D_length2(counter)=major_length(counter)*cos(relative_angle(counter)/180*pi)
*cos(proj_angle_rt(counter));

major_2D_length3(counter)=major_length(counter)*cos(helical_angle(counter)/180*pi)*
cos(proj_angle_tz(counter));
end

datafile=[slidenum '-3measure.mat'];
load(datafile);
stats=regionprops(L,'Centroid','PixelList');
for i=1:smc_count_measured
    counter=counter+1

    center=centroid(i,:);
    x0=center(1)+uxy12(1)+uxy23(1);
    y0=center(2)+uxy12(2)+uxy23(2);

    center_x(counter)=x0;
```

```
    center_y(counter)=y0;

    % intersection on inner boundary
    c3=Ci(1)*y0-Ci(2)*x0;
    Ai=[Ci(1) Ci(2); Ci(2) -Ci(1)];
    bi=[-Ci(3); -c3];
    xy1=Ai\bi;
    % intersection on outer boundary
    Ao=[Co(1) Co(2); Ci(2) -Ci(1)];
    bo=[-Co(3); -c3];
    xy2=Ao\bo;
    % Intramural location
    d1=sqrt((x0-xy1(1))^2+(y0-xy1(2))^2);
    d2=sqrt((x0-xy2(1))^2+(y0-xy2(2))^2);
    intramural_loc(counter)=d1/(d1+d2);

    plot(x0,y0,'go')
    plot([xy1(1) xy2(1)],[xy1(2) xy2(2)],'g-')

    % relative orientation & helical orientation

    % Coordinate Transformation
    smc_xyz=[principal_direction(:,3,i)];
    % long axis orientation in rtz coord
    smc_rtz=trans*smc_xyz;
norm(smc_rtz)
    % set orientation on positive theta direction
    if smc_rtz(2)<0
       smc_rtz = -smc_rtz;
    end

    % projection onto r-theta plane
    smc_rt=[smc_rtz(1);smc_rtz(2)];
    % projection angle onto r-theta plane
    proj_angle_rt(counter) = acos(norm(smc_rt));
    % normalize projected vector
    smc_rt_n=smc_rt/norm(smc_rt);

    % projection onto theta-z plane
    smc_tz=[smc_rtz(2);smc_rtz(3)];
    % projection angle onto theta-z plane
    proj_angle_tz(counter) = acos(norm(smc_tz));
    % normalize projected vector
    smc_tz_n=smc_tz/norm(smc_tz);

    % relative angle
```

```
    relative_angle(counter)=90-(acos(smc_rt_n(1)))*180/pi;

    % helical angle (REF: z-vector out of screen is positive)
    helical_angle(counter)=90-(acos(smc_tz_n(2)))*180/pi;

    % length of major axis
    major_length(counter)=principal_length(3,1,i)-principal_length(3,2,i);

    % length of 2D projected major axis
    centroid_obj=stats(smc_list_measured(i)).Centroid;
    voxel_list=stats(smc_list_measured(i)).PixelList;
    center_2D=centroid(1:2);
    pixel_list=voxel_list(:,1:2);

    pixel_num=size(pixel_list,1);
    ctr_to_pxl=pixel_list-ones(pixel_num,1)*center_2D;

    major_2D_length(counter)=0.45*(max(ctr_to_pxl*direction')-
min(ctr_to_pxl*direction'));

major_2D_length2(counter)=major_length(counter)*cos(relative_angle(counter)/180*pi)
*cos(proj_angle_rt(counter));

major_2D_length3(counter)=major_length(counter)*cos(helical_angle(counter)/180*pi)*
cos(proj_angle_tz(counter));
end

hold off

proj_angle_rt=(proj_angle_rt*180/pi)';
proj_angle_tz=(proj_angle_tz*180/pi)';

center_x=center_x';
center_y=center_y';

major_length=major_length';
major_2D_length=major_2D_length';
major_2D_length2=major_2D_length2';
major_2D_length3=major_2D_length3';
relative_angle=relative_angle';
intramural_loc=intramural_loc';
helical_angle=helical_angle';

savefile=[slidenum ' distribution.mat'];
save(savefile,'major_length','relative_angle','intramural_loc','helical_angle');
```

Implementation of the Heterogeneous Model

Optimize Parameters by Minimizing the Error Function (optima.m)

```
% optima.m
% Optimization - Uniform collagen strain at 100 mmHg assumption
% This program optimizes model variables by minimizing error from
% experimental data

% INPUT DATA
% lambda_theta         51x10
% lambda_theta2        51x12
% lambda_r             51x10
% lambda_r2            51x12
% t                   51x10
% t2                  51x12
% rmean               51x10
% rmean2              51x12
% Ie                  51x1
% Ic                  51x1
% P_exp               1x10

% lc                  51x10
% lc2                 51x12
% hd0                 51x1
% hd                  51x10
% hd2                 51x12
% h0                  51x1

% To be determined
% l0                  51x1
% lambda_c            51x10
% lambda_c2           51x12
% FeCe, FcCc1, Cc2


P_exp_kPa = P_exp * 0.1333224;

lambda_h =
sqrt(1.5^2*(sin(hd0).^2*ones(1,10))+lambda_theta.^2.*(cos(hd0).^2*ones(1,10)));
lambda_h2 =
sqrt(1.5^2*(sin(hd0).^2*ones(1,12))+lambda_theta2.^2.*(cos(hd0).^2*ones(1,12)));

% Guess
guess_Cc2 = 3.01:0.01:4.00;
```

```
c100 = zeros(1,100);
r_sq2 = zeros(1,100);

for ki=1:100

Cc2 = guess_Cc2(ki);

% Guess Collagen stretch at 100 mmHg
guess_pool = 1.350:0.0001:1.550;
% r-square
R_sq = zeros(1,2001);

for i=1:1:2001

    % collagen stretch at 100mmHg
    lambda_c100 = guess_pool(i);
    % collagen recruiting points
    lambda_rp = lambda_h(:,9)/lambda_c100;
    % collagen stretch ratio
    lambda_c = lambda_h./(lambda_rp*ones(1,10));

    % unit-step matrix
    unitstep = lambda_c>1;
    unitstepr = unitstep==0;
    lambda_c = lambda_c.*unitstep + unitstepr;

    %Substitute2:
    S2=exp(Cc2*(0.5*(lambda_c.^2-1)).^2).*(lambda_c.^2-1).*lambda_c.^2;

    % coefficient of FeCe
    coeff_e=sum((Ie*ones(1,10)).*(lambda_theta.^2-lambda_r.^2).*t./rmean);
    % coefficient of FcCc1
    coeff_c=sum((Ic*ones(1,10)).*(S2.*cos(hd).^2).*t./rmean);

    % multiple regression
    X = [coeff_e' coeff_c'];
    y = P_exp_kPa';
    a = X\y;

    % result based on guessed collagen stretch at 100 mmHg
    FeCe = a(1);
    FcCc1 = a(2);

    % estimate P
    P_est_kPa = coeff_e*FeCe + coeff_c*FcCc1;
```

```
    % error function
    avg_P_exp = mean(P_exp_kPa);
    SSE = sum((P_exp_kPa - P_est_kPa).^2);
    SSR = sum((P_exp_kPa - avg_P_exp).^2);
    r_square = 1 - SSE/SSR;

    R_sq(i) = r_square;

end

% find local maxima
% plot(guess_pool,R_sq);
[C,I]=max(R_sq);

% OPTIMAL collagen stretch at 100mmHg
lambda_c100 = guess_pool(I);
% collagen recruiting points
lambda_rp = lambda_h(:,9)/lambda_c100;
% collagen stretch ratio
lambda_c = lambda_h./(lambda_rp*ones(1,10));

% unit-step matrix
unitstep = lambda_c>1;
unitstepr = unitstep==0;
lambda_c = lambda_c.*unitstep + unitstepr;

%Substitute2:
S2=exp(Cc2*(0.5*(lambda_c.^2-1)).^2).*(lambda_c.^2-1).*lambda_c.^2;

% coefficient of FeCe
coeff_e=sum((Ie*ones(1,10)).*(lambda_theta.^2-lambda_r.^2).*t./rmean);
% coefficient of FcCc1
coeff_c=sum((Ic*ones(1,10)).*(S2.*cos(hd).^2).*t./rmean);

% multiple regression
X = [coeff_e' coeff_c'];
y = P_exp_kPa';
a = X\y;

% result based on guessed collagen stretch at 100 mmHg
FeCe = a(1);
FcCc1 = a(2);

% estimate P
P_est_kPa = coeff_e*FeCe + coeff_c*FcCc1;
P_est = P_est_kPa / 0.1333224;
```

```
% error function
avg_P_exp = mean(P_exp_kPa);
SSE = sum((P_exp_kPa - P_est_kPa).^2);
SSR = sum((P_exp_kPa - avg_P_exp).^2);
r_square = 1 - SSE/SSR;

if lambda_rp(51) < 1
   r_square = 0;
end

r_sq2(ki) = r_square;
c100(ki) = lambda_c100;
end

plot(guess_Cc2,r_sq2);
max(c100)
min(c100)

[C,I]=max(r_sq2);
% Optimal Cc2
Cc2 = guess_Cc2(I);
% OPTIMAL collagen stretch at 100mmHg
lambda_c100 = c100(I);
% collagen recruiting points
lambda_rp = lambda_h(:,9)/lambda_c100;
% collagen stretch ratio
lambda_c = lambda_h./(lambda_rp*ones(1,10));

% unit-step matrix
unitstep = lambda_c>1;
unitstepr = unitstep==0;
lambda_c = lambda_c.*unitstep + unitstepr;

%Substitute2:
S2=exp(Cc2*(0.5*(lambda_c.^2-1)).^2).*(lambda_c.^2-1).*lambda_c.^2;

% coefficient of FeCe
coeff_e=sum((Ie*ones(1,10)).*(lambda_theta.^2-lambda_r.^2).*t./rmean);
% coefficient of FcCc1
coeff_c=sum((Ic*ones(1,10)).*(S2.*cos(hd).^2).*t./rmean);

% multiple regression
X = [coeff_e' coeff_c'];
y = P_exp_kPa';
a = X\y;
```

```
% result based on guessed collagen stretch at 100 mmHg
FeCe = a(1);
FcCc1 = a(2);

% estimate P
P_est_kPa = coeff_e*FeCe + coeff_c*FcCc1;
P_est = P_est_kPa / 0.1333224;

% error function
avg_P_exp = mean(P_exp_kPa);
SSE = sum((P_exp_kPa - P_est_kPa).^2);
SSR = sum((P_exp_kPa - avg_P_exp).^2);
r_square = 1 - SSE/SSR;

% END OF OPTIMIZATION

% collagen stretch ratio
lambda_c2 = lambda_h2./(lambda_rp*ones(1,12));
% unit-step matrix
unitstep2 = lambda_c2>1;
unitstepr2 = unitstep2==0;
lambda_c2 = lambda_c2.*unitstep2 + unitstepr2;

%Substitute2:
S22=exp(Cc2*(0.5*(lambda_c2.^2-1)).^2).*(lambda_c2.^2-1).*lambda_c2.^2;

% coefficient of FeCe
coeff_e2=sum((Ie*ones(1,12)).*(lambda_theta2.^2-lambda_r2.^2).*t2./rmean2);
% coefficient of FcCc1
coeff_c2=sum((Ic*ones(1,12)).*(S22.*cos(hd2).^2).*t2./rmean2);

% estimate P
P_est_kPa2 = coeff_e2*FeCe + coeff_c2*FcCc1;
P_est2 = P_est_kPa2 / 0.1333224;

% Lagrange multiplier
p_e=(Ie*ones(1,12)).*(lambda_theta2.^2-lambda_r2.^2).*t2./rmean2;
p_c=(Ic*ones(1,12)).*(S22.*cos(hd2).^2).*t2./rmean2;

for k=1:50
   p_e(k+1,:)=p_e(k,:)+p_e(k+1,:);
   p_c(k+1,:)=p_c(k,:)+p_c(k+1,:);
end

p=(ones(51,1)*P_est_kPa2)+FeCe*((Ie*ones(1,12)).*lambda_r2.^2-p_e)-FcCc1*p_c;
```

```
% True stress estimation
sigma_theta=-
p+FeCe*((Ie*ones(1,12)).*lambda_theta2.^2)+FcCc1*((Ic*ones(1,12)).*S22.*cos(hd2).^
2);

sigma_r = -p + FeCe*((Ie*ones(1,12)).*lambda_r2.^2);
sigma_z = -p +
FeCe*1.5^2*(Ie*ones(1,12))+FcCc1*((Ic*ones(1,12)).*S22.*sin(hd2).^2);;
```

Compute Stress Distributions Using the Heterogeneous Model (Stress100.m for normotensive arteries)

```
% Stress100.m
% This program computes
% Stress Distribution at 100 mmHg using the heterogeneous model
% with aquired parameters

% INPUT DATA
% r100exp   52x1

% target lumen pressure
P_target_kPa = 100 * 0.1333224;
r100 = zeros(52,1);
r100(1) = 3.2320;

% pseudo cumulative area of each layer
a100exp = zeros(51,1);
for i=1:51
   a100exp(i) = r100exp(i+1)^2 - r100exp(1)^2;
end

% layer boundary at 100
for i=1:51
   r100(i+1) = sqrt(a100exp(i) + r100(1)^2);
end

% rmean at 100
rm100 = zeros(51,1);
for i=1:51;
   rm100(i) = sqrt((r100(i+1)^2+r100(i)^2)/2);
end

lambda_theta100 = lambda_theta2(:,9);
```

```
lambda_r100 = lambda_r2(:,9);
hd100 = hd2(:,9);
t100 = zeros(51,1);

% pseudo rm0
rm0 = rm100./lambda_theta100;

flag = 0;
err_prev = (P_target_kPa - P_est_kPa2(9))^2;

while (flag == 0)
   % Update Radius Data
   r100(1) = r100(1) - 0.0001;
   for i=1:51
      r100(i+1) = sqrt(a100exp(i) + r100(1)^2);
   end
   for i=1:51;
      rm100(i) = sqrt((r100(i+1)^2+r100(i)^2)/2);
   end

   % Update thickness
   for i=1:51
      t100(i) = r100(i+1)-r100(i);
   end

   % Update lambda_theta
   lambda_theta100 = rm100./rm0;

   % Update lambda_r
   lambda_r100 = 1/1.5./lambda_theta100;

   % Update helical angle
   hd100 = atan(1.5/2/pi*h0./rm100);

   % Update lambda h
   lambda_h100 = sqrt(1.5^2*sin(hd0).^2+lambda_theta100.^2.*cos(hd0).^2);

   % Update collagen stretch
   lambda_c_100 = lambda_h100./lambda_rp;
   % unit-step matrix
   unitstep = lambda_c_100 > 1;
   unitstepr = unitstep==0;
   lambda_c_100 = lambda_c_100.*unitstep + unitstepr;

   %Substitute2:
```

```
   S2=exp(Cc2*(0.5*(lambda_c_100.^2-1)).^2).*(lambda_c_100.^2-
1).*lambda_c_100.^2;

   % coefficient of FeCe
   coeff_e=sum(Ie.*(lambda_theta100.^2-lambda_r100.^2).*t100./rm100);
   % coefficient of FcCc1
   coeff_c=sum(Ic.*(S2.*cos(hd100).^2).*t100./rm100);
   % estimate P
   P100_est_kPa = coeff_e*FeCe + coeff_c*FcCc1;
   P100_est = P100_est_kPa / 0.1333224

   % error function
   err = (P_target_kPa - P100_est_kPa)^2
   if (err > err_prev)
      flag = 1;
   end
   err_prev = err;
end

   % Update Radius Data
   r100(1) = r100(1) + 0.0001;
   for i=1:51
      r100(i+1) = sqrt(a100exp(i) + r100(1)^2);
   end
   for i=1:51;
      rm100(i) = sqrt((r100(i+1)^2+r100(i)^2)/2);
   end

   % Update thickness
   for i=1:51
      t100(i) = r100(i+1)-r100(i);
   end

   % Update lambda_theta
   lambda_theta100 = rm100./rm0;

   % Update lambda_r
   lambda_r100 = 1/1.5./lambda_theta100;

   % Update helical angle
   hd100 = atan(1.5/2/pi*h0./rm100);

   % Update lambda h
   lambda_h100 = sqrt(1.5^2*sin(hd0).^2+lambda_theta100.^2.*cos(hd0).^2);

   % Update collagen stretch
```

```
    lambda_c_100 = lambda_h100./lambda_rp;
    % unit-step matrix
    unitstep = lambda_c_100 > 1;
    unitstepr = unitstep==0;
    lambda_c_100 = lambda_c_100.*unitstep + unitstepr;

    %Substitute2:
    S2=exp(Cc2*(0.5*(lambda_c_100.^2-1)).^2).*(lambda_c_100.^2-
1).*lambda_c_100.^2;

    % coefficient of FeCe
    coeff_e=sum(Ie.*(lambda_theta100.^2-lambda_r100.^2).*t100./rm100);
    % coefficient of FcCc1
    coeff_c=sum(Ic.*(S2.*cos(hd100).^2).*t100./rm100);
    % estimate P
    P100_est_kPa = coeff_e*FeCe + coeff_c*FcCc1;
    P100_est = P100_est_kPa / 0.1333224

    % error function
    err = (P_target_kPa - P100_est_kPa)^2;

% Stress Distribution

% Lagrange multiplier
p_e=Ie.*(lambda_theta100.^2-lambda_r100.^2).*t100./rm100;
p_c=Ic.*(S2.*cos(hd100).^2).*t100./rm100;

for k=1:50
    p_e(k+1,:)=p_e(k,:)+p_e(k+1,:);
    p_c(k+1,:)=p_c(k,:)+p_c(k+1,:);
end

p=(ones(51,1)*P100_est_kPa)+FeCe*(Ie.*lambda_r100.^2-p_e)-FcCc1*p_c;

% True stress estimation
s100_theta=-p+FeCe*(Ie.*lambda_theta100.^2)+FcCc1*(Ic.*S2.*cos(hd100).^2);

s100_r = -p + FeCe*(Ie.*lambda_r100.^2);
s100_z = -p + FeCe*1.5^2*Ie+FcCc1*(Ic.*S2.*sin(hd100).^2);;
```

Implementation of the Homogeneous Model

Optimize Parameters by Minimizing the Error Function (optima_homo.m)

```
% optima_homo.m
% This program uses the homogeneous model
% Optimization -
% Uniform collagen recruiting assumption
% Homogeneous Media Assumed

% INPUT DATA
% lambda_theta         51x10
% lambda_theta2        51x12
% lambda_r             51x10
% lambda_r2            51x12
% t                   51x10
% t2                  51x12
% rmean               51x10
% rmean2              51x12
% Ie                  51x1
% Ic                  51x1
% P_exp               1x10

% lc                  51x10
% lc2                 51x12
% hd                  51x10
% hd2                 51x12
% h0                  51x1

% To be determined
% l0                  51x1
% lambda_c            51x10
% lambda_c2           51x12
% FeCe, FcCc1, Cc2

% New INPUT data
% hd0                 51x1

P_exp_kPa = P_exp * 0.1333224;

lambda_h =
sqrt(1.5^2*(sin(hd0).^2*ones(1,10))+lambda_theta.^2.*(cos(hd0).^2*ones(1,10)));
lambda_h2 =
sqrt(1.5^2*(sin(hd0).^2*ones(1,12))+lambda_theta2.^2.*(cos(hd0).^2*ones(1,12)));

% Guess
guess_Cc2 = 0.01:0.01:1.00;

c100 = zeros(1,100);
r_sq2 = zeros(1,100);
```

```
for ki=1:100

Cc2 = guess_Cc2(ki);

% Guess Collagen recruiting point
guess_pool = 1.0000:0.0001:1.3000;
% r-square
R_sq = zeros(1,3001);

for i=1:1:3001

    % collagen recruitment point
    lambda_rp = guess_pool(i);
    % collagen stretch ratio
    lambda_c = lambda_h/lambda_rp;

    % unit-step matrix
    unitstep = lambda_c>1;
    unitstepr = unitstep==0;
    lambda_c = lambda_c.*unitstep + unitstepr;

    %Substitute2:
    S2=exp(Cc2*(0.5*(lambda_c.^2-1)).^2).*(lambda_c.^2-1).*lambda_c.^2;

    % coefficient of FeCe
    coeff_e=sum((Ie*ones(1,10)).*(lambda_theta.^2-lambda_r.^2).*t./rmean);
    % coefficient of FcCc1
    coeff_c=sum((Ic*ones(1,10)).*(S2.*cos(hd).^2).*t./rmean);

    % multiple regression
    X = [coeff_e' coeff_c'];
    y = P_exp_kPa';
    a = X\y;

    % result based on guessed collagen stretch at 100 mmHg
    FeCe = a(1);
    FcCc1 = a(2);

    % estimate P
    P_est_kPa = coeff_e*FeCe + coeff_c*FcCc1;

    % error function
    avg_P_exp = mean(P_exp_kPa);
    SSE = sum((P_exp_kPa - P_est_kPa).^2);
    SSR = sum((P_exp_kPa - avg_P_exp).^2);
```

```
    r_square = 1 - SSE/SSR;

    R_sq(i) = r_square;

end

% find local maxima
%plot(guess_pool,R_sq);
[C,I]=max(R_sq);

% OPTIMAL collagen recruiting point
lambda_rp = guess_pool(I);
% collagen stretch ratio
lambda_c = lambda_h/lambda_rp;

% unit-step matrix
unitstep = lambda_c>1;
unitstepr = unitstep==0;
lambda_c = lambda_c.*unitstep + unitstepr;

%Substitute2:
S2=exp(Cc2*(0.5*(lambda_c.^2-1)).^2).*(lambda_c.^2-1).*lambda_c.^2;

% coefficient of FeCe
coeff_e=sum((Ie*ones(1,10)).*(lambda_theta.^2-lambda_r.^2).*t./rmean);
% coefficient of FcCc1
coeff_c=sum((Ic*ones(1,10)).*(S2.*cos(hd).^2).*t./rmean);

% multiple regression
X = [coeff_e' coeff_c'];
y = P_exp_kPa';
a = X\y;

% result based on guessed collagen stretch at 100 mmHg
FeCe = a(1);
FcCc1 = a(2);

% estimate P
P_est_kPa = coeff_e*FeCe + coeff_c*FcCc1;
P_est = P_est_kPa / 0.1333224;

% error function
avg_P_exp = mean(P_exp_kPa);
SSE = sum((P_exp_kPa - P_est_kPa).^2);
SSR = sum((P_exp_kPa - avg_P_exp).^2);
r_square = 1 - SSE/SSR;
```

```
r_sq2(ki) = r_square;
c100(ki) = lambda_rp;
end

plot(guess_Cc2,r_sq2);
max(c100)
min(c100)

[C,I]=max(r_sq2);

% Optimal Cc2
Cc2 = guess_Cc2(I);

% OPTIMAL collagen stretch at 100mmHg
lambda_rp = c100(I);
% collagen stretch ratio
lambda_c = lambda_h/lambda_rp;

% unit-step matrix
unitstep = lambda_c>1;
unitstepr = unitstep==0;
lambda_c = lambda_c.*unitstep + unitstepr;

%Substitute2:
S2=exp(Cc2*(0.5*(lambda_c.^2-1)).^2).*(lambda_c.^2-1).*lambda_c.^2;

% coefficient of FeCe
coeff_e=sum((Ie*ones(1,10)).*(lambda_theta.^2-lambda_r.^2).*t./rmean);
% coefficient of FcCc1
coeff_c=sum((Ic*ones(1,10)).*(S2.*cos(hd).^2).*t./rmean);

% multiple regression
X = [coeff_e' coeff_c'];
y = P_exp_kPa';
a = X\y;

% result based on guessed collagen stretch at 100 mmHg
FeCe = a(1);
FcCc1 = a(2);

% estimate P
P_est_kPa = coeff_e*FeCe + coeff_c*FcCc1;
P_est = P_est_kPa / 0.1333224;

% error function
```

```
avg_P_exp = mean(P_exp_kPa);
SSE = sum((P_exp_kPa - P_est_kPa).^2);
SSR = sum((P_exp_kPa - avg_P_exp).^2);
r_square = 1 - SSE/SSR;

% END OF OPTIMIZATION

% collagen stretch ratio
lambda_c2 = lambda_h2/lambda_rp;
% unit-step matrix
unitstep2 = lambda_c2>1;
unitstepr2 = unitstep2==0;
lambda_c2 = lambda_c2.*unitstep2 + unitstepr2;

%Substitute2:
S22=exp(Cc2*(0.5*(lambda_c2.^2-1)).^2).*(lambda_c2.^2-1).*lambda_c2.^2;

% coefficient of FeCe
coeff_e2=sum((Ie*ones(1,12)).*(lambda_theta2.^2-lambda_r2.^2).*t2./rmean2);
% coefficient of FcCc1
coeff_c2=sum((Ic*ones(1,12)).*(S22.*cos(hd2).^2).*t2./rmean2);

% estimate P
P_est_kPa2 = coeff_e2*FeCe + coeff_c2*FcCc1;
P_est2 = P_est_kPa2 / 0.1333224;

% Lagrange multiplier
p_e=(Ie*ones(1,12)).*(lambda_theta2.^2-lambda_r2.^2).*t2./rmean2;
p_c=(Ic*ones(1,12)).*(S22.*cos(hd2).^2).*t2./rmean2;

for k=1:50
   p_e(k+1,:)=p_e(k,:)+p_e(k+1,:);
   p_c(k+1,:)=p_c(k,:)+p_c(k+1,:);
end

p=(ones(51,1)*P_est_kPa2)+FeCe*((Ie*ones(1,12)).*lambda_r2.^2-p_e)-FcCc1*p_c;

% True stress estimation
sigma_theta=-
p+FeCe*((Ie*ones(1,12)).*lambda_theta2.^2)+FcCc1*((Ic*ones(1,12)).*S22.*cos(hd2).^
2);

sigma_r = -p + FeCe*((Ie*ones(1,12)).*lambda_r2.^2);
sigma_z = -p +
FeCe*1.5^2*(Ie*ones(1,12))+FcCc1*((Ic*ones(1,12)).*S22.*sin(hd2).^2);;
```

Compute Stress Distributions Using the Homogeous Model (Stress100h.m for normotensive arteries)

```
% Stress100h.m
% This model computes distribution of stress at 100 mmHg
% Using the homogeneous model

% INPUT DATA
% r100exp   52x1

% target lumen pressure
P_target_kPa = 100 * 0.1333224;
r100 = zeros(52,1);
r100(1) = 3.2320;

% pseudo cumulative area of each layer
a100exp = zeros(51,1);
for i=1:51
   a100exp(i) = r100exp(i+1)^2 - r100exp(1)^2;
end

% layer boundary at 100
for i=1:51
   r100(i+1) = sqrt(a100exp(i) + r100(1)^2);
end

% rmean at 100
rm100 = zeros(51,1);
for i=1:51;
   rm100(i) = sqrt((r100(i+1)^2+r100(i)^2)/2);
end

lambda_theta100 = lambda_theta2(:,9);
lambda_r100 = lambda_r2(:,9);
hd100 = hd2(:,9);
t100 = zeros(51,1);

% pseudo rm0
rm0 = rm100./lambda_theta100;

flag = 0;
err_prev = (P_target_kPa - P_est_kPa2(9))^2;

while (flag == 0)
   % Update Radius Data
```

```
r100(1) = r100(1) - 0.0001;
for i=1:51
   r100(i+1) = sqrt(a100exp(i) + r100(1)^2);
end
for i=1:51;
   rm100(i) = sqrt((r100(i+1)^2+r100(i)^2)/2);
end

% Update thickness
for i=1:51
   t100(i) = r100(i+1)-r100(i);
end

% Update lambda_theta
lambda_theta100 = rm100./rm0;

% Update lambda_r
lambda_r100 = 1/1.5./lambda_theta100;

% Update helical angle
hd100 = atan(1.5/2/pi*h0./rm100);

% Update lambda h
lambda_h100 = sqrt(1.5^2*sin(hd0).^2+lambda_theta100.^2.*cos(hd0).^2);

% Update collagen stretch
lambda_c_100 = lambda_h100/lambda_rp;
unitstep = lambda_c_100 > 1;   % unit-step matrix
unitstepr = unitstep==0;
lambda_c_100 = lambda_c_100.*unitstep + unitstepr;

%Substitute2:
S2=exp(Cc2*(0.5*(lambda_c_100.^2-1)).^2).*(lambda_c_100.^2-
1).*lambda_c_100.^2;

% coefficient of FeCe
coeff_e=sum(Ie.*(lambda_theta100.^2-lambda_r100.^2).*t100./rm100);
% coefficient of FcCc1
coeff_c=sum(Ic.*(S2.*cos(hd100).^2).*t100./rm100);
% estimate P
P100_est_kPa = coeff_e*FeCe + coeff_c*FcCc1;
P100_est = P100_est_kPa / 0.1333224

% error function
err = (P_target_kPa - P100_est_kPa)^2
if (err > err_prev)
```

```
        flag = 1;
    end
    err_prev = err;
end

    % Update Radius Data
    r100(1) = r100(1) + 0.0001;
    for i=1:51
        r100(i+1) = sqrt(a100exp(i) + r100(1)^2);
    end
    for i=1:51;
        rm100(i) = sqrt((r100(i+1)^2+r100(i)^2)/2);
    end

    % Update thickness
    for i=1:51
        t100(i) = r100(i+1)-r100(i);
    end

    % Update lambda_theta
    lambda_theta100 = rm100./rm0;

    % Update lambda_r
    lambda_r100 = 1/1.5./lambda_theta100;

    % Update helical angle
    hd100 = atan(1.5/2/pi*h0./rm100);

    % Update lambda h
    lambda_h100 = sqrt(1.5^2*sin(hd0).^2+lambda_theta100.^2.*cos(hd0).^2);

    % Update collagen stretch
    lambda_c_100 = lambda_h100/lambda_rp;
    % unit-step matrix
    unitstep = lambda_c_100 > 1;
    unitstepr = unitstep==0;
    lambda_c_100 = lambda_c_100.*unitstep + unitstepr;

    %Substitute2:
    S2=exp(Cc2*(0.5*(lambda_c_100.^2-1)).^2).*(lambda_c_100.^2-
1).*lambda_c_100.^2;

    % coefficient of FeCe
    coeff_e=sum(Ie.*(lambda_theta100.^2-lambda_r100.^2).*t100./rm100);
    % coefficient of FcCc1
    coeff_c=sum(Ic.*(S2.*cos(hd100).^2).*t100./rm100);
```

```
    % estimate P
    P100_est_kPa = coeff_e*FeCe + coeff_c*FcCc1;
    P100_est = P100_est_kPa / 0.1333224

    % error function
    err = (P_target_kPa - P100_est_kPa)^2;

% Stress Distribution

% Lagrange multiplier
p_e=Ie.*(lambda_theta100.^2-lambda_r100.^2).*t100./rm100;
p_c=Ic.*(S2.*cos(hd100).^2).*t100./rm100;

for k=1:50
    p_e(k+1,:)=p_e(k,:)+p_e(k+1,:);
    p_c(k+1,:)=p_c(k,:)+p_c(k+1,:);
end

p=(ones(51,1)*P100_est_kPa)+FeCe*(Ie.*lambda_r100.^2-p_e)-FcCc1*p_c;

% True stress estimation
s100_theta=-p+FeCe*(Ie.*lambda_theta100.^2)+FcCc1*(Ic.*S2.*cos(hd100).^2);

s100_r = -p + FeCe*(Ie.*lambda_r100.^2);
s100_z = -p + FeCe*1.5^2*Ie+FcCc1*(Ic.*S2.*sin(hd100).^2);;
```

REFERENCES

Alberts, B., Bray, D., Lewis, J., Raff, M., Roberts, K. and Watson, J. D. (1994). Molecular biology of the cell. New York, Garland Publishing.

Armentano, R. L., Barra, J. G., Levenson, J., Simon, A. and Pichel, R. H. (1995). "Arterial wall mechanics in conscious dogs: assessment of viscous, inertial, and elastic moduli to characterize aortic wall behavior." Circulation Research **76**: 468-478.

Arnoczky, S. P., Lavagnino, M., Whallon, J. H. and Hoonjan, A. (2002). "In situ cell nucleus deformation in tendons under tensile load; a morphological analysis using confocal laser microscopy." Journal of Orthopaedic Research **20**(1): 29-35.

Arribas, S. M., Hillier, C., Gonzalez, C., McGrory, S., Dominiczak, A. F. and McGrath, J. C. (1997). "Cellular aspects of vascular remodeling in hypertension revealed by confocal microscopy." Hypertension **30**: 1455-1464.

Asanuma, K., Magid, R., Johnson, C., Nerem, R. M. and Galis, Z. S. (2003). "Uniaxial strain upregulates matrix-degrading enzymes produced by human vascular smooth muscle cells." American Journal of Physiology - Heart and Circulatory Physiology **284**: H1778-H1784.

Avolio, A., Jones, D. and Tafazzoli-Shadpour, M. (1998). "Quantification of alterations in structure and function of elastin in the arterial media." Hypertension **32**: 170-175.

Badreck-Amoudi, A., Patel, C. K., Kane, T. P. C. and Greenwald, S. E. (1996). "The effect of age on residual strain in the rat aorta." Journal of Biomechanical Engineering **118**: 440-444.

Baraga, J. J., Rava, R. P., Taroni, P., Kittrell, C., Fitzmaurice, M. and Feld, M. S. (1990). "Laser induced fluorescence spectroscopy of normal and atherosclerotic human aorta using 306-310 nm excitation." Lasers in Surgery and Medicine **10**(3): 245-261.

Blomfield, J. and Farrar, J. F. (1967). "Fluorescence spectra of arterial elastin." Biochemical and Biophysical Research Communications **28**(3): 346-351.

Brownlee, R. D. and Langille, B. L. (1991). "Arterial adaptations to altered blood flow." Canadian Journal of Physiology and Pharmacology **69**(7): 978-83.

Canham, P. B., Finlay, H. M., Kiernan, J. A. and Ferguson, G. G. (1999). "Layered structure of saccular aneurysms assessed by collagen birefringence." Neurological Research **21**(7): 618-626.

Canham, P. B., Finlay, H. M., Whittaker, P. and Starkey, J. (1986). "The tunica muscularis of human brain arteries: three-dimensional measurements of alignment of the smooth muscle mechanical axis, by polarized light and the universal stage." Neurological Research **8**(2): 66-74.

Canham, P. B., Henderson, R. M. and Peters, M. W. (1982). "Coalignment of the muscle cell and nucleus, cell geometry and Vv in the tunica media of monkey cerebral arteries, by electron microscopy." Journal of Microscopy **127**: 311-319.

Canham, P. B., Whittaker, P., Barwick, S. E. and Schwab, M. E. (1992). "Effect of pressure on circumferential order of adventitial collagen in human brain arteries." Canadian Journal of Physiology and Pharmacology **70**(2): 296-305.

Capers, Q., Alexander, R. W., Lou, P., De Leon, H., Wilcox, J. N., Ishizaka, N., Howard, A. B. and Taylor, W. R. (1997). "Monocyte chemoattractant protein-1 expression in aortic tissues of hypertensive rats." Hypertension **30**(6): 1397-1402.

Carew, T. E., Vaishnav, R. N. and Patel, D. J. (1968). "Compressibility of the arterial wall." Circulation Research **23**(1): 61-68.

Carey, D. J. (1991). "Control of growth and differentiation of vascular cells by extracellular matrix proteins." Annual Review of Physiology **53**: 161-177.

Chaudhry, H. R., Bukiet, B., Davis, A., Ritter, A. B. and Findley, T. (1997). "Residual stresses in oscillating thoracic arteries reduce circumferential stresses and stress gradients." Journal of Biomechanics **30**(1): 57-62.

Chesler, N. C., Ku, D. N. and Galis, Z. S. (1999). "Transmural pressure induces matrix-degrading activity in porcine arteries ex vivo." American journal of physiology **277(5 pt 2)**: H2002-9.

Chuong, C. J. and Fung, Y. C. (1983). "Three-dimensional stress distribution in arteries." Journal of Biomechanical Engineering **105**: 268-274.

Chuong, C. J. and Fung, Y. C. (1986). "On residual stresses in arteries." Journal of Biomechanical Engineering **108**: 189-192.

Clark, J. M. and Glagov, S. (1985). "Transmural organization of the arterial media: the lamellar unit revisited." Arteriosclerosis **5**(1): 19-34.

Conklin, B. S., Richter, E. R., Kreutziger, K. L., Zhong, D.-S. and Chen, C. (2002). "Development and evaluation of a novel decellularized vascular xenograft." Medical Engineering and Physics **24**: 173-183.

Cooke, P. H. and Fay, F. S. (1972). "Correlation between fiber length, ultrastructure, and the length-tension relationship of mammalian smooth muscle." Journal of Cell Biology **52**: 105-116.

Davis, E. C. (1993). "Smooth muscle cell to elastic lamina connections in developing mouse aorta: Role in aortic medial organization." Laboratory Investigation **68**(1): 89-99.

Davis, E. C. (1993). "Stability of elastin in the developing mouse aorta: a quantitative radioautographic study." Histochemistry **100**(1): 17-26.

Davis, N. P. (2002). Axial stretch as a means of lengthening arteries: an investigation in organ culture. Atlanta, Georgia Institute of Technology.

Davis, N. P., Han, H. C., Wayman, B. and Vito, R. P. (2005). "Sustained Axial Loading Lengthens Arteries in Organ Culture." Annals of Biomedical Engineering **33**(7): 867-877.

Debelle, L. and Tamburro, A. M. (1999). "Elastin: molecular description and function." The International Journal of Biochemistry & Cell Biology **31**: 261-272.

Defawe, O. D., Kenagy, R. D., Choi, C., Wan, S. Y. C., Deroanne, C., Nusgens, B., Sakalihasan, N., Colige, A. and Clowes, A. W. (2005). "MMP-9 regulates both positively and negatively collagen gel contraction: a nonproteolytic function of MMP-9." Cardiovascular Research **66**: 402-409.

Demiray, H. (1972). "A note on the elasticity of soft biological tissues." Journal of Biomechanics **5**(3): 309-311.

Dickhout, J. G. and Lee, R. M. K. W. (2000). "Increased medial smooth muscle cell length is responsible for vascular hypertrophy in young hypertensive rats." American Journal of Physiology - Heart and Circulatory Physiology **279**: H2085-H2094.

Dobrin, P. B. (1986). "Biaxial anisotropy of dog carotid artery: estimation of circumferential elastic modulus." Journal of Biomechanics **19**(5): 351-358.

Dobrin, P. B. (1999). "Distribution of lamellar deformations: implications for properties of the arterial media." Hypertension **33**(3): 806-810.

Dollery, C. M., McEwan, J. R. and Henney, A. M. (1995). "Matrix metalloproteinases and cardiovascular disease." Circulation Research **77**(5): 863-868.

Doyle, J. M. and Dobrin, P. B. (1971). "Finite deformation analysis of the relaxed and contracted dog carotid artery." Microvascular research **3**: 400-415.

Ehlers, E. G. (1987). Optical mineralogy: theory and technique. Palo Alto, CA, Blackwell Scientific Publications.

Fay, F. S. and Delise, C. M. (1973). "Contraction of isolated smooth-muscle cells - structural changes." Proceedings of the National Academy of Sciences of the United States of America **70**(3): 641-645.

Feldman, S. A. and Glagov, S. (1971). "Transmedial collagen and elastin gradients in human aortas: reversal with age." Atherosclerosis **13**: 385-394.

Fey, E. G., Wan, K. M. and Penman, S. (1984). "Epithelial cytoskeletal framework and nuclear matrix-intermediate filament scaffold: three-dimensional organization and protein composition." Journal of Cell Biology **98**: 1973-1984.

Finlay, H. M., Dixon, J. G. and Canham, P. B. (1991). "Fabric organization of the subendothelium of the human brain artery by polarized-light microscopy." Arteriosclerosis, thrombosis, and vascular biology **11**: 681-690.

Finlay, H. M., McCullough, L. and Canham, P. B. (1995). "Three-dimensional collagen organization of human brain arteries at different transmural pressures." Journal of Vascular Research **32**: 301-312.

Fischer, E. I. C., Armentano, R. L., Pessana, F. M., Graf, S., Romero, L., Christen, A. I., Simon, A. and Levenson, J. (2002). "Endothelium-dependent arterial wall tone elasticity modulated by blood viscosity." American Journal of Physiology - Heart and Circulatory Physiology **282**: H389-H394.

Fitzmaurice, M., Bordagaray, J. O., Engelmann, G. L., Richards-Kortum, R., Kolubayev, T., Feld, M. S., Ratliff, N. B. and Kramer, J. R. (1989). "Argon ion laser-excited autofluorescence in normal and atherosclerotic aorta and coronary arteries: morphologic studies." American Heart Journal **118**(5 pt 1): 1028-1038.

Fridez, P., Zulliger, M., Bobard, F., Montorzi, G., Miyazaki, H., Hayashi, K. and Stergiopulos, N. (2003). "Geometrical, functional, and histomorphometric adaptation of rat carotid artery in induced hypertension." Journal of Biomechanics **36**: 671-680.

Fung, Y. C. (1965). Foundations of Solid Mechanics. Englewood Cliffs, NJ, Prentice-Hall.

Fung, Y. C. (1973). "Biorheology of soft tissues." Biorheology **10**(2): 139-155.

Fung, Y. C. (1984). Biodynamics: circulation. New York, NY, Springer-Verlag.

Fung, Y. C. (1993). Biomechanics: mechanical properties of living tissues. New York, Springer-Verlag.

Galis, Z. S., Sukhova, G. K. and Libby, P. (1995). "Microscopic localization of active proteases by in situ zymography: detection of matrix metalloproteinase activity in vascular tissue." FASEB **9**(10): 974-980.

Greenwald, S. E., Moore, J. E., Rachev, A., Kane, T. P. C. and Meister, J.-J. (1997). "Experimental investigation of the distribution of residual strains in the artery wall." Journal of Biomechanical Engineering **119**: 438-444.

Han, H.-C. and Ku, D. N. (2001). "Contractile responses in arteries subjected to hypertensive pressure in seven-day organ culture." Annals of Biomedical Engineering **29**: 467-475.

Hasan, N. and Greenwald, S. E. (1995). "Variation in the concentration of scleroproteins across the arterial wall." Journal of Pathology **176**(supplement): 26A.

Holzapfel, G. A. and Gasser, T. C. (2000). "A new constitutive framework for arterial wall mechanics and a comparative study of material models." Journal of Elasticity **61**: 1-48.

Holzapfel, G. A., Gasser, T. C. and Stadler, M. (2002). "A structural model for the viscoelastic behavior of arterial walls: continuum formulation and finite element analysis." European Journal of Mechanics A/Solids **21**: 441-463.

Holzapfel, G. A. and Weizsacker, H. W. (1998). "Biomechanical behavior of the arterial wall and its numerical characterization." Computers in Biology and Medicine **28**: 377-392.

Humphrey, J. D. (1995). "Mechanics of the arterial wall: review and directions." Critical Reviews in Biomedical Engineering **23**(1-2): 1-162.

Ingber, D. E. (1993). "Cellular tensegrity: defining new rules of biological design that govern the cytoskeleton." Journal of Cell Science **104**: 613-627.

Jackson, Z. S., Gotlieb, A. I. and Langille, B. L. (2002). "Wall tissue remodeling regulates longitudinal tension in arteries." Circulation Research **90**: 918-925.

Johnson, C. and Galis, Z. S. (2004). "Matrix metalloproteinase-2 and -9 differentially regulate smooth muscle cell migration and cell-mediated collagen organization." Arteriosclerosis, thrombosis, and vascular biology **24**: 54-60.

Junqueira, L. C. U., Bignolas, G. and Brentani, R. R. (1979). "Picrosirius staining plus polarization microscopy, a specific method for collagen detection in tissue sections." Histochemical Journal **11**: 447-455.

Junqueira, L. C. U., Montes, G. S. and Krisztan, R. M. (1979). "The collagen of the vertebrate peripheral nervous system." Cell and Tissue Research **202**: 453-460.

Junqueira, L. C. U., Montes, G. S. and Sanchez, E. M. (1982). "The influence of tissue section thickness on the study of collagen by the Picrosirius-polarization method." Histochemistry **74**(1): 153-156.

Kamiya, A. and Togawa, T. (1980). "Adaptive regulation of wall shear stress to flow change in the canine carotid artery." American Journal of Physiology **239**(1): H14-21.

Karnik, S. K., Brooke, B. S., Bayes-Genis, A., Sorensen, L., Wythe, J. D., Schwartz, R. S., Keating, M. T. and Li, D. Y. (2003a). "A critical role for elastin signaling in vascular morphogenesis and disease." Development **130**(2): 411-423.

Karnik, S. K., Wythe, J. D., Sorensen, L., Brooke, B. S., Urness, L. D. and Li, D. Y. (2003b). "Elastin induces myofibrillogenesis via a specific domain, VGVAPG." Matrix Biology **22**: 409-425.

Koyama, H., Raines, E. W., Bornfeldt, K. E., Roberts, J. M. and Ross, R. (1996). "Fibrillar collagen inhibits arterial smooth muscle proliferation through regulation of Cdk2 inhibitors." Cell **87**: 1069-1078.

Ku, D. N. (1997). "Blood flow in arteries." Annual Review of Fluid Mechanics **29**: 399-434.

Kuo, K.-H. and Seow, C. Y. (2004). "Contractile filament architecture and force transmission in swine airway smooth muscle." Journal of Cell Science **117**(8): 1503-1511.

Langille, B. L. (1996). "Arterial remodeling: relation to hemodynamics." Canadian Journal of Physiology and Pharmacology **74**(7): 834-841.

Lee, R. T., Schoen, F. J., Loree, H. M., Lark, M. W. and Libby, P. (1996). "Circumferential stress and matrix metalloproteinase 1 in human coronary atherosclerosis: implications for plaque rupture." Arteriosclerosis, Thrombosis, and Vascular Biology **16**(8): 1070-1073.

Lefevre, M. and Rucker, R. B. (1980). "Aorta elastin turnover in normal and hypercholesterolemic japanese quail." Biochimica et Biophysica Acta **630**(4): 519-529.

Lehoux, S., Lemarié, C. A., Esposito, B., Lijnen, H. R. and Tedgui, A. (2004). "Pressure-induced matrix metalloproteinase-9 contributes to early hypertensive remodeling." Circulation **109**: 1041-1047.

Li, C. and Xu, Q. (2000). "Mechanical stress-initiated signal transductions in vascular smooth muscle cells." Cellular Signalling **12**: 435-445.

Li, X. and Hayashi, K. (1996). "Alternate method for the analysis of residual strain in the arterial wall." Biorheology **33**: 439-449.

Liu, S. Q. (1998). "Influence of tensile strain on smooth muscle cell orientation in rat blood vessels." Journal of Biomechanical Engineering **120**(3): 313-320.

Liu, S. Q. and Fung, Y. C. (1989). "Relationship between hypertension, hypertrophy, and opening angle of zero-stress state of arteries following aortic constriction." Journal of Biomechanical Engineering **111**: 325-335.

Maniotis, A. J., Chen, C. S. and Ingber, D. E. (1997). "Demonstration of mechanical connections between integrins, cytoskeletal filaments, and nucleoplasm that stabilize nuclear structure." Proceedings of the National Academy of Sciences of the United States of America **94**(3): 849-854.

Matrisian, L. M. (1992). "The matrix-degrading metalloproteinases." BioEssays **14**(7): 455-463.

Matsumoto, T., Goto, T. and Sato, M. (2002). Residual stress and strain in the lamellar unit of the aorta: experiment and analysis. Proceedings of the 4th World Congress Biomechanics, Calgary, Canada.

Matsumoto, T. and Hayashi, K. (1994). "Mechanical and dimensional adaptation of rat aorta to hypertension." Journal of Biomechanical Engineering **116**: 278-283.

Matsumoto, T. and Hayashi, K. (1996). "Stress and strain distribution in hypertensive and normotensive rat aorta considering residual strain." Journal of Biomechanical Engineering **118**(1): 62-73.

Mavromatis, K., Fukai, T., Tate, M., Chesler, N., Ku, D. N. and Galis, Z. S. (2000). "Early effects of arterial hemodynamic conditions on human saphenous veins

perfused ex vivo." Arteriosclerosis, Thrombosis, and Vascular Biology **20**: 1889-1895.

McAnulty, R. J. and Laurent, G. J. (1987). "Collagen synthesis and degradation in vivo. Evidence for rapid rates of collagen turnover with extensive degradation of newly synthesized collagen in tissues of the adult rat." Collagen and Related Research **7**(2): 93-104.

Merrilees, M. J., Tiang, K. M. and Scott, L. (1987). "Changes in collagen fibril diameters across artery walls including a correlation with glycosaminoglycan content." Connective Tissue Research **16**: 237-257.

Nissen, R., Cardinale, G. J. and Udenfriend, S. (1978). "Increased turnover of arterial collagen in hypertensive rats." Proceedings of the National Academy of Sciences of the United States of America **75**(1): 451-453.

O'Callaghan, C. J. and Williams, B. (2000). "Mechanical strain-induced extracellular matrix production by human vascular smooth muscle cells: role of TGF-β_1." Hypertension **36**(3): 319-324.

Peters, M. W., Canham, P. B. and Finlay, H. M. (1983). "Circumferential alignment of muscle cells in the tunica media of the human brain artery." Blood Vessels **20**(5): 221-233.

Peterson, S. J. and Okamoto, R. J. (2000). "Effect of residual stress and heterogeneity on circumferential stress in the arterial wall." Journal of Biomechanical Engineering **122**(4): 454-456.

Peyton, S. R. and Putnam, A. J. (2005). "Extracellular matrix rigidity governs smooth muscle cell motility in a biphasic fashion." Journal of Cellular Physiology **204**: 198-209.

Pienta, K. J. and Coffey, D. S. (1992). "Nuclear-cytoskeletal interactions: evidence for physical connections between the nucleus and cell periphery and their alteration by transformation." Journal of Cellular Biochemistry **49**: 357-365.

Rachev, A. (1997). "Theoretical study of the effect of stress-dependent remodeling on arterial geometry under hypertensive conditions." Journal of Biomechanics **30**(8): 819-827.

Rachev, A. and Greenwald, S. E. (2003). "Residual strains in conduit arteries." Journal of Biomechanics **36**: 661-670.

Rachev, A., Stergiopulos, N. and Meister, J.-J. (1996). "Theoretical study of dynamics of arterial wall remodeling in response to changes in blood pressure." Journal of Biomechanics **29**(5): 635-642.

Rowe, A. J., Finlay, H. M. and Canham, P. B. (2003). "Collagen biomechanics in cerebral arteries and bifurcations assessed by polarizing microscopy." Journal of Vascular Research **40**: 406-415.

Saini, A., Berry, C. L. and Greenwald, S. E. (1995). "Effect of age and sex on residual stress in the aorta." Journal of Vascular Research **32**(6): 398-405.

Seliktar, D., Black, R. A., Vito, R. P. and Nerem, R. M. (2000). "Dynamic mechanical conditioning of collagen-gel blood vessel constructs induces remodeling in vitro." Annals of Biomedical Engineering **28**: 351-362.

Small, J. V. and Gimona, M. (1998). "The cytoskeleton of the vertebrate smooth muscle cell." Acta Physiologica Scandinavica **164**: 341-348.

Sodek, J. and Ferrier, J. M. (1988). "Collagen remodelling in rat periodontal tissues: compensation for precursor reutilization confirms rapid turnover of collagen." Collagen and Related Research **8**(1): 11-21.

Stergiopulos, N., Vulliemoz, S., Rachev, A., Meister, J.-J. and Greenwald, S. E. (2001). "Assessing the homogeneity of the elastic properties and composition of the pig aortic media." Journal of Vascular Research **38**: 237-246.

Szendroi, M., Vajta, G., Kovacs, L., Schaff, Z. and Lapis, K. (1984). "Polarization colours of collagen fibres: a sign of collagen production activity in fibrotic processes." Acta Morphologica Hungarica **32**(1): 47-55.

Taber, L. A. and Humphrey, J. D. (2001). "Stress-modulated growth, residual stress, and vascular heterogeneity." Journal of Biomechanical Engineering **123**(6): 528-535.

Takamizawa, K. and Hayashi, K. (1987). "Strain energy density function and uniform strain hypothesis for arterial mechanics." Journal of Biomechanics **20**(1): 7-17.

Todd, M. E., Laye, C. G. and Osborne, D. N. (1983). "The dimensional characteristics of smooth muscle in rat blood vessels: a computer-assisted analysis." Circulation Research **53**: 319-331.

Torrance, H. B. and Shwatz, S. (1961). "The elastic behaviour of the arterial wall." Journal of the Royal College of Surgeons of Edinburgh **7**: 55.

Vaishnav, R. N., Young, J. T., Janicki, J. S. and Patel, D. J. (1972). "Nonlinear anisotropic elastic properties of the canine aorta." Biophysical Journal **12**(8): 1008-1027.

Vito, R. P. and Dixon, S. A. (2003). "Blood vessel constitutive models - 1995-2002." Annual Review of Biomedical Engineering **5**: 413-439.

Vito, R. P. and Hickey, J. (1980). "The mechanical properties of soft tissues-II: the elastic response of arterial segments." Journal of Biomechanics **13**: 951-957.

Vito, R. P., Whang, M. C., Glagov, S. and Aoki, T. (1991). The distribution of strains and stresses in the arterial cross section. Proceedings of the 1991 ASME Winter Annual Meeting, Atlanta, GA.

von Maltzahn, W. W. (1983). "Parameter sensitivity analysis and improvement of a two-layer arterial wall model." Journal of Biomechanical Engineering **105**(4): 389-392.

von Maltzahn, W. W., Besdo, D. and Wiemer, W. (1981). "Elastic properties of arteries: a nonlinear two-layer cylindrical model." Journal of Biomechanics **14**(6): 389-397.

von Maltzahn, W. W., Warriyar, R. G. and Keitzer, W. F. (1984). "Experimental measurements of elastic properties of media and adventitia of bovine carotid arteries." Journal of Biomechanics **17**(11): 839-847.

Vorp, D. A., Rajagopal, K. R., Smolinski, P. J. and Borovetz, H. S. (1995). "Identification of elastic properties of homogeneous, orthotropic vascular segments in distension." Journal of Biomechanics **28**(5): 501-512.

Walmsley, J. G. and Canham, P. B. (1979). "Orientation of nuclei as indicators of smooth muscle cell alignment in the cerebral artery." Blood Vessels **16**(1): 43-51.

Whittaker, P., Kloner, R. A., Boughner, D. R. and Pickering, J. G. (1994). "Quantitative assessment of myocardial collagen with picrosirius red staining and circularly polarized light." Basic Research in Cardiology **89**(5): 397-410.

Williams, B. (1998). "Mechanical influences on vascular smooth muscle cell function." Journal of Hypertension **16**: 1921-1929.

Wilson, E., Sudhir, K. and Ives, H. E. (1995). "Mechanical strain of rat vascular smooth muscle cells is sensed by specific extracellular matrix/integrin interactions." Journal of Clinical Investigation **96**(5): 2364-2372.

Wilson, S. H., Herrmann, J., Lerman, L. O., Holmes, D. R., Napoli, C., Ritman, E. L. and Lerman, A. (2002). "Simvastatin preserves the structure of coronary adventitial vasa vasorum in experimental hypercholesterolemia independent of lipid lowering." Circulation **105**(5): 415-418.

Wolinsky, H. and Glagov, S. (1967). "A lamellar unit of aortic medial structure and function in mammals." Circulation research **20**(1): 99-111.

Wolman, M. and Kasten, F. H. (1986). "Polarized light microscopy in the study of the molecular structure of collagen and reticulin." Histochemistry **85**(1): 41-49.

Work, S. S. and Warshaw, D. M. (1988). "Detection of surface movements on single smooth muscle cells: digital video microscopy." Computers in Biology and Medicine **18**(6): 385-393.

Worth, N. F., Rolfe, B. E., Song, J. and Campbell, G. R. (2001). "Vascular smooth muscle cell phenotypic modulation in culture is associated with reorganization of contractile and cytoskeletal proteins." Cell Motility and the Cytoskeleton **49**(3): 130-145.

Wuyts, F. L., Vanhuyse, V. J., Langewouters, G. J., Decraemer, W. F., Raman, E. R. and Buyle, S. (1995). "Elastic properties of human aortas in relation to age and atherosclerosis: a structural model." Physics in medicine and biology **40**(10): 1577-1597.

Xu, C., Zarins, C. K., Bassiouny, H. S., Briggs, W. H., Reardon, C. and Glagov, S. (2000). "Differential transmural distribution of gene expression for collagen types I and III proximal to aortic coarctation in the rabbit." Journal of vascular research **37**(3): 170-182.

Zulliger, M. A., Fridez, P., Hayashi, K. and Stergiopulos, N. (2004). "A strain energy function for arteries accounting for wall composition and structure." Journal of Biomechanics **37**: 989-1000.

Zulliger, M. A., Rachev, A. and Stergiopulos, N. (2004). "A constitutive formulation of arterial mechanics including vascular smooth muscle tone." American Journal of Physiology - Heart and Circulatory Physiology **287**: H1335-H1343.